Fall 2021

Structure and Stability of AG-IR Bimetallic Catalysts Prepared By Electroless Deposition and Synthesis and Performance of High Selectivity Movnbsbteox Mixed Oxides for Oxidative Dehydrogenation of Ethane

Mozhdeh Parizad

STRUCTURE AND STABILITY OF AG-IR BIMETALLIC CATALYSTS PREPARED BY ELECTROLESS DEPOSITION AND SYNTHESIS AND PERFORMANCE OF HIGH SELECTIVITY $MoVNbSbTeO_x$ MIXED OXIDES FOR OXIDATIVE DEHYDROGENATION OF ETHANE

by

Mozhdeh Parizad

Bachelor of Science
Shiraz University, 2011

Master of Science
Amirkabir University of Technology, 2014

Submitted in Partial Fulfillment of the Requirements

For the Degree of Doctor of Philosophy in

Chemical Engineering

College of Engineering and Computing

University of South Carolina

2021

Accepted by:

John R. Regalbuto, Major Professor

John R. Monnier, Major Professor

Aaron K. Vannucci, Committee Member

Andreas Heyden, Committee Member

Melissa Ann Moss, Committee Member

Tracey L. Weldon, Interim Vice Provost and Dean of the Graduate School

DEDICATION

I dedicate this work to my wonderful amazing husband, Mehdi, for your unconditional love. You have been always by myside and a promise that I have the best friend forever.

ACKNOWLEDGEMENTS

I would like to thank my supervisors, Dr. John R. Regalbuto and Dr. John R. Monnier for being incredible advisors and incredible listeners. You constantly help me put things into perspective and prepare me for great things in the future. I wish to thank my committee members, Dr. Andreas Heyden for his patience and support, Dr. Arron Vannucii for his time and help, and Dr. Melissa Moss for her consideration. I would like to offer my special thanks to Dr. Andrew Wong, Dr. Benjamin Egelske, and Dr. John Tengco for their contribution to my journey and their unforgettable friendship. I am thankful to all of the Dr. Regalbuto's, Dr. Monnier's and Dr.Vannucci's Lab group members for being great coworkers and friends. I am grateful to our kind graduate coordinator, Marcia Rowen, for her assistance with my administrative and technical issues. I would love to thank Scott and Victoria Andes for their companionship and being amazing friends to me. I would like to thank my family for their love and support in all my endeavors.

Most of all, I am extremely grateful to my great husband, Mehdi, for his unconditional love, support and encouragement. I am sure in this journey, I would not be able to take any step further without you, and I am thankful I have you in my life.

ABSTRACT

Improvements in industrial thermal conversions can be realized through comprehensive catalytic studies, where enhanced catalyst stability and activity are desired. Catalyst performance can be greatly affected by structural changes at high temperatures. In the case of supported Ag-Ir particles, the surface free energy (SFE) can determine preferred arrangement of the component metals. The well-established methods of strong electrostatic adsorption (SEA) and electroless deposition (ED) have been used to synthesize highly-dispersed Ag/Ir on different alumina supports (δ,θ-Al_2O_3 and γ-Al_2O_3). Surface thermodynamics dictate that the Ir-Ag system should conform to minimize free energy resulting in a low SFE Ag layer localized on the high SFE Ir surface. XRD data and STEM images indicate that both monometallic catalysts sintered, but deposition of a Ag shell by ED prevented the sintering of both Ag and Ir. H_2 TPD measurements corroborate the high H_2 uptake chemisorption experiments, indicating the additional H_2 capacity was due to more weakly-bound H, which computational and XPS results confirm.

In light olefin production from ethane, selective catalytic oxidative dehydrogenation (ODH) represents an alternative to thermal dehydrogenation, where the latter requires temperatures exceeding 1100^0C. ODH can achieve similar ethylene space-time yields using a catalytic process operating at 300-600 ^{0}C. Complex multicomponent oxides have been shown to be effective ODH catalysts, with significant findings

suggesting exceptional performance of Te-containing MoVNb mixed oxides. MoVNbTe(Sb)Ox M1-phase catalysts were synthesized using a slurry method in accordance with previous techniques disclosed in patent literature. Different parameters, i.e. compositions and thermal treatments, in synthesis and their effects on catalyst performance were studied. Catalysts were characterized by using XRD, SEM, BET, and XRF. It was determined that Te has a structural effect during synthesis and lack thereof results in no catalyst activity. A complete kinetic study for the same M1-phase catalyst was done including reactant (C_2H_6, O_2) and product (C_2H_4, CO_2, and H_2O) reaction orders. Three pressures of 0, 60, and 120psig and three temperatures of 275, 310, and 350°C were used. The activation energies of ethane consumption and products formation were calculated. Higher reaction orders of ethane for ethylene formation compared to combustion products formation suggest ethane rich feed for optimal reaction condition. Low temperature operation is preferred to avoid non-selective product formation and an oxygen lean environment is suggested to prevent deactivation of the catalyst via partial reduction.

TABLE OF CONTENTS

LIST OF TABLES

LIST OF FIGURES

CHAPTER 1

INTRODUCTION

Several techniques to improve catalyst stability and activity have been developed focusing on catalyst modifications for decreasing the costs associate to industrial processes. In this regard, one of the strongest incentives for improved catalyst activity and durability is that downtime of industrial processes can lead to losses of millions of dollars each day. Although modification of chemical processes can be a solution for decreasing the rate of catalyst deactivation, in many important chemical processes such as automotive emissions, dry reforming of methane, catalytic pyrolysis, or steam reforming, harsh conditions at high temperatures are unavoidable.

The main objective of this work is designing a stable and active catalyst in three projects. In second chapter of my dissertation (this work was published in October 2020 in ACS Catalysis), the challenges of catalyst stability and activity at high temperatures were studied by using the well-established methods of strong electrostatic adsorption (SEA) and Electroless deposition (ED) to synthesize highly-dispersed Ag/Ir on different alumina supports (δ,θ-Al_2O_3 and γ-Al_2O_3). It is worth noting that the surface free energy of Ir (3231 ergs/cm^2) is much higher than that of Ag (1302 ergs/cm^2). As a result, surface thermodynamics favor the Ir - Ag system should arrange to give the lowest free energy of a Ag layer localized on the Ir surface to minimize the high Surface Free Energy (SFE) of Ir. The characterization results of XRD and STEM images indicate sintering of both

monometallic catalysts. However, the deposition of a Ag shell by ED prevented both Ag and Ir from sintering. Also, TPD of H_2 measurements corroborate the high H_2 uptake chemisorption experiments and indicated the additional H_2 capacity was attributed to more weakly-bound H. Furthermore, XPS data and computational studies using density function theory (DFT) showed that additional H_2 capacity is associated to changes in the adsorption stoichiometry of H:Ir (from 1:1 to 4:1) at single atom Ir sites that are surrounded by Ag shell atoms.

The selective oxidation of low molecular weight alkanes such as ethane has become much more attractive as a viable, less expensive route to ethylene, the world's highest volume chemical intermediate. Third chapter of my dissertation contains the preparation on an optimal $MoVNbTeSbO_x$ catalyst. The current process of thermal dehydrogenation (cracking) of ethane to ethylene consuming a disproportionate amount of energy is not sustainable from either economic, industrial, or environmental perspectives. Complex metal oxides and multicomponent oxides catalysts provide the most promising catalysts for partial oxidation. One of these, a mixed oxide containing Mo, V, Nb, Sb, and Te, has become one of the leading candidates for this reaction. The preferred empirical formula is $Mo_1V_{0.29}Nb_{0.17}Te_{0.125}$ $Sb_{0.01}Ox$. The preferred composition is approximately 95% selective to C_2H_4 even at high conversion levels of C_2H_6. Non-selective products are limited to small amounts of CO, CO_2, and CH_3COOH.

In the third chapter, we have optimized the structure of the mixed oxide to yield the highest concentration of the presumably selective M1 crystalline phase and, by difference, minimized the amount of the presumably non-selective M2 phase. Parameters that have been optimized are the elemental composition of the mixed oxide and the

thermal conditions for calcination of the mixed oxide precursor and the annealing temperatures at 500 – 700°C (in inert gas flow) to form the crystalline M1 and M2 phases. Catalysts have been characterized by XRD, SEM, BET/pore analysis, and XRF. Specifically, the amount of Te in the lattice has been varied over the range 0-0.2 (atomic ratio normalized to Mo) to determine the effect on formation of the desired M1 phase and resulting catalytic activity. Tellurium plays an important role in catalyst activity and catalysts without Te show no activity; Te also has a structural effect on the mixed oxide catalyst. Catalysts with no Te contain no M1 crystalline phase. Also, we found that the percentage of M1 and M2 phase can be tuned by changing the calcination ramp and post treatment of the catalyst by oxalic acid solution. The higher post treated catalyst activity is attributed to the removal of vanadium. In this context, since it was concluded that catalysts with different M1/M2 ratio synthesized by various calcination ramp rates have the same performance, the effect of post treatment is attributed to the change of vanadium amount (V^{+5}).

In the fourth chapter, a complete kinetic analysis at 0, 60, and 120 psig pressures and temperatures of 275, 310, and 350 °C for the optimized catalyst have been conducted for the reactants (C_2H_6 and O_2) and kinetic inhibition of the products (C_2H_4, CO_2, and H_2O). It should be noted that the catalyst showed an excellent stability since after each set of experiments no deactivation was observed by catalyst evaluation at standard reaction condition (15% C_2H_6, 10%O_2, 5% CH_4, balance He, 0 psig, and 350°C). Reaction orders of ~1.0 and 0.0 for ethane and O_2, respectively, indicate the rate limiting step is likely bond breaking of the first C-H bond to form the adsorbed and reactive C_2H_5 species which undergoes further oxidation to form C_2H_4. The ~0 order for O_2 is also consistent

with a Mars Van Krevelen mechanism where lattice oxygen is the active species during reaction, and the gas phase O_2 re-oxidizes the mixed oxide lattice.

Finally, ethane conversion and ethylene selectivity were found to be independent of CO_2 presence even at high concentration to the feed. In contrast, using ethylene in the feed caused a strong inhibition. Nonetheless, the activation energy analysis indicated that running the reaction at low temperature favors the ethylene formation.

CHAPTER 2

STABILIZATION OF CATALYTIC SURFACES THROUGH CORE-SHELL STRUCUTRES: AG-IR/AL_2O_3 CASE STUDY

Parizad, M., Wong, A. P., Reber, A. C., Tengo, J. M. M., Karakalos, S. G., Khanna, S. N., Regalbuto, J. R., and Monnier, J. R. ACS Catalysis, 2020, 10, 22, 13352–13363.

Reprinted here with permission of the publisher

2.1 Abstract

To solve the challenges of catalyst stability and activity at high temperatures, catalyst composition and method of preparation are critical. In this context, the well-established methods of strong electrostatic adsorption (SEA) and Electroless deposition (ED) have been used to synthesize highly-dispersed Ag/Ir on different alumina supports (δ,θ-Al_2O_3 and γ-Al_2O_3). The surface free energy of Ag (1302 ergs/cm^2) is much lower than that of Ir (3231 ergs/cm^2); surface thermodynamics dictate the Ir - Ag system should arrange to give the lowest free energy of a Ag layer localized on the Ir surface to minimize the high SFE of Ir. The catalysts remained dispersed at high temperature annealing treatments (400, 600, and 800°C). For all Ag-Ir/δ,θ-Al_2O_3 samples, H_2 chemisorption values were higher after annealing at 400 and 600°C than at 200°C and were considerably higher than for the corresponding base catalyst of 1.0 wt% Ir/δ,θ-Al_2O_3 used as the base catalyst. XRD data and STEM images indicate that both monometallic catalysts sintered, but deposition of a Ag shell by ED prevented the sintering of both Ag and Ir. TPD of H_2 measurements corroborate the high H_2 uptake chemisorption experiments and indicated the additional H_2 capacity was due to more weakly-bound H. Computational and XPS results suggest the excess H_2 chemisorption can be accounted for by binding up to four H atoms to single surface Ir atoms surrounded by Ag in the shell of the bimetallic catalysts that have been pretreated at temperatures > 400°C. As a result, H_2 capacity increases from the normal adsorption stoichiometry of H : Ir = 1:1 up to as high as 4:1.

2.2 Introduction

Catalytic stability is a focus for many industrial processes. Catalyst deactivation often limits catalyst time-on-stream through the loss of active sites by particle sintering, metal leaching, and coke formation [1-3]. Downtime of industrial processes can cause losses of millions of dollars each day; therefore, strong incentives exist to improve catalyst durability and activity. Although modifications to chemical processes can alter the rate of catalyst deactivation, in many cases harsh reaction conditions at high-temperatures such as automotive emissions, dry reforming of methane, catalytic pyrolysis, or steam reforming are unavoidable [4-6].

Several techniques to improve catalyst stability have been developed that focus on modifications to catalyst supports to increase the interaction of metal nanoparticles with the support. Support durability can be improved by use of promoters to improve interactions with supported nanoparticles, e.g., alumina doped with silica, La, Ba, or Ca[7-8]. Alternatively, incorporation of the active metal sites into the lattice of the support like those found in homogenous precipitation methods have been used [9-10]. Another method to improve nanoparticle stability is by addition of a secondary metal. Bimetallic catalysts often have increased activity, selectivity, and even stability compared to their monometallic analogs [11-13]. The inclusion of secondary metals can increase nanoparticle stability by altering the physical properties in an alloy, by changing oxidation states of one or both metals, or by selective placement of a second metal shell on the surface of another metal[14].

Electroless deposition (ED) is a method of catalyst preparation that can test the hypothesis of improved stability by depositing a shell of a second metal on the surface of

a pre-existing metal. The guidelines and methodology have been recently discussed in a recent book chapter[15]. Basically, ED requires a liquid phase, organic reducing agent (RA) to be activated on a nanoparticle core and after activation, the reduction of a metal salt occurs to form the beginning of a shell layer. The deposition mechanism can be either catalytic or auto-catalytic depending on whether the RA is adsorbed/activated on the core or the shell metal, respectively. Many different core-shell bimetallic combinations of Au-Pd, Pt-Pd, Ag-Pt, Ag-Pd, Cu-Pd, Ag-Ir, Pt-Co, Pt-Ru, Pt-Ni, Pt-Rh, among others, have been synthesized using ED [16-21].

In this study, we focus on enhancing the stability of catalytic surfaces by depositing a Ag layer on the surface of an Ir core supported on Al_2O_3 to form a more stable Ag layer. The Ir particles were deposited on the Al_2O_3 surface using the well-established method of strong electrostatic adsorption (SEA) developed by Regalbuto[22-23]. The surface free energy (SFE) of Ag (1302 ergs/cm^2) is much lower than that of Ir (3231 ergs/cm^2); the SFE of generic Al_2O_3 is stated as 805 ergs/cm^2 [24-25]. Thus, surface thermodynamics dictate the Al_2O_3 - Ir - Ag system should arrange to give the lowest system free energy of Ir supported on Al_2O_3 with a Ag layer localized on the Ir surface to minimize the high SFE of the Ir surface. By adding a lower SFE metal shell onto a higher SFE metal core, a bimetallic system is created which thermodynamically constrains the lower SFE metal to remain on the surface of the higher SFE metal core. Further, because the support almost always has the lowest SFE, there is yet another impediment for diffusion of the shell component onto the support. Thus, it should be possible to design and synthesize numerous metal core-shell configurations to theoretically prevent sintering of the shell metal and stop the migration of the shell metal component onto the

support surface. To test this hypothesis, a series of Ag coverages prepared by ED using an aqueous bath containing $Ag(CN)_2^-$ and hydrazine (N_2H_4) as reducing agent on Ir have been synthesized and characterized following annealing at temperatures ranging from 200 –800°C. The stability was determined by annealing treatments followed by chemisorption, XRD, XPS, and STEM measurements. Experimental results were compared to DFT calculations on the same system.

2.3 Methods

2.3.1 Computational details

First principles theoretical studies were performed using dispersion-corrected density functional theory (DFT) within the generalized gradient approximation (GGA) proposed by Perdew, Burke and Ernzerhof (PBE) for the exchange and correlation functional[26]. The DFT-D3 method was used to include the Van der Waals corrections[27]. The computations were performed using the VASP code, and the Kohn–Sham orbitals were expanded using a plane wave basis set and the cutoff was set to 400 eV[28-29]. The support was modelled by taking a periodic cell of 72 Al atoms and 108 O atoms in the structure of α-Al_2O_3[30]. The Gibbsite model of α-Al_2O_3 included 63 Al atoms and 108 O atoms, and 27 H atoms. The model of γ-Al_2O_3 included 4 layers with 128 Al atoms and 196 O atoms. A dipole correction was incorporated along the z-axis of the slab. Due to the large size of the surface supercell only the Γ point was used for Brillouin zone integration. A conjugate-gradient optimization method was used and structures were not considered optimized until the forces on the atoms were minimized to 0.01 eV/Å or less. For the $Ag_{11}Ir_{11}$ clusters, 25 total structures were optimized, and multiple optimizations for each structural motif were performed to make certain that the structure has found the

local minimum. For the hydrogen binding studies, the hydrogen atoms were placed at ten sites around the cluster and optimized. The lowest energy structures are reported. The geometry optimization of the cluster supported on the surface was performed with the bottom two layers of the alumina support fixed, while the top three layers were free to relax.

2.3.2 Experimental details

All catalyst supports were calcined at 700°C for 4 hours before metals deposition. SEA was used to deposit the iridium anionic precursor, potassium hexachloroiridiate (K_2IrCl_6, Alfa Aesar 99.9%), on δ,θ-alumina (SASOL APA 0.2, BET surface area = 37 m^2/g) and γ-alumina (UOP VGL-25, BET surface area = 164 m^2/g) at low pH conditions. Solutions of HCl and NaOH were used to adjust the pH to lower and higher values, respectively. Potassium silver cyanide, $KAg(CN)_2$, and potassium gold cyanide, $KAu(CN)_2$, were used as the precursors for ED, and the reducing agents (RA) were hydrazine and formaldehyde.

2.3.3 Catalyst characterization

Metal concentrations were analyzed by a Perkin-Elmer 2000DV ICP-OES and a Perkin-Elmer AA 400. A Micromeritics 2920 Analyzer was used to determine the number of catalytically active sites by H_2 pulse chemisorption. All catalysts were first reduced at 200°C in H_2 followed by hydrogen chemisorption at 40°C. Annealing treatments were then performed *in situ* using flowing UHP argon after being passed through both Deoxo and H_2O removal filters (Restek) at 200, 400, 600, and 800°C for 4 hours each followed by hydrogen chemisorption at 40°C. All chemisorption measurements were performed immediately after pretreatment. TPD measurements were

also performed using a Micromeritics 2920 Analyzer in the continuous flow mode to determine desorption characteristics of H_2. Pretreatments in flowing Ar were also done i*n situ* before desorption experiments were conducted. Following pretreatment, a 10% H_2/balance Ar gas flow was passed over the sample at 25°C for 15 – 30 minutes to saturate the surface with chemisorbed H. After purging the sample for 15 min to remove residual and physically adsorbed H_2, the TPD experiment was started and the sample heated from 20 – 420°C at 10°C/min. Desorbed H_2 was monitored as a positive peak in the Ar carrier stream. X-ray diffraction (XRD) patterns were collected using a Rigaku MiniFlex II equipped with a high sensitivity D/tex Ultra Si slit detector and a Cu-Kα radiation source (λ=1.5406 Å) operated at 30 mA and 15 kV. Scans were typically made over a 2θ range of 20˚- 80˚ at a scan rate of 2.0˚/min. Diffraction patterns were also obtained for the supports alone. Metal diffraction patterns were deconvoluted using Gaussian peak shapes, and average particle sizes were estimated by the Scherer equation with a shape factor of 0.94.

XPS analyses were carried out on a Kratos AXIS Ultra DLD XPS system with a monochromatic Al Ka source at 15 keV and 150W at pressures below 10^{-9} torr. The X-rays were incident at an angle of 45° with respect to the surface normal. High resolution core level spectra were measured with a pass energy of 10 eV and analysis of the data was carried out using XPSPEAK41 software. The XPS system equipped with a hemispherical electron analyzer, catalysis cell for in-situ chemical treatments, and a load lock chamber for rapid introduction of samples without breaking vacuum. The XPS experiments were conducted using an electron gun directed on the sample for charge neutralization.

2.4 Results and discussion

2.4.1 Theoretical Investigations

The hypothesis was that core-shell nanoparticles will have enhanced stability when the core metal has a larger surface free energy than the shell metal. To test this hypothesis we performed a series of theoretical investigations on cluster models to identify if such core-shell particles exhibit enhanced stability. The first model system was a ten atom cluster, Ag_9X on α-alumina (0001), in which 9 Ag atoms formed the shell of the core-shell cluster, and the core was a single metal atom, X; we tested X=Au, Ag, Cu, Pd, Pt, Ni, Rh, Co, Ir, Fe, and Ru, where the metals were sorted by smallest to largest calculated surface free energy[31]. The Ag binding energies were calculated using Eq. 1, and the core metal binding energies for the core element X using equation 2.

$$(\text{Ag B.E.}) = E(Ag_8X\_Al_2O_3)+E(Ag_{atom})- E(Ag_9X\_Al_2O_3) \quad (2.1)$$

$$(\text{X B.E.}) = E(Ag_9\_Al_2O_3)+E(X_{atom})- E(Ag_9X\_Al_2O_3) \quad (2.2)$$

The silver binding energies, core metal binding energies and structures of several representative structures are shown in Figure 1A and 1B. The Ag binding energy is a measure of the stability of the cluster, and if Ostwald ripening is the dominant mechanism for sintering,[32-34] then the Ag binding energy is a good proxy for the amount of sintering. The Ag binding energy of Ag_{10} is 2.37 eV, so we can consider the cluster to have enhanced stability if the Ag binding energy is greater than this value and can consider the cluster to have a reduced stability if the Ag binding energy is less than this value. The Ag_9 clusters with the greatest Ag binding energies occur when the core metal is Ru, Fe, and Ir; Ag binding energies are 2.74, 2.64, and 2.60 eV, respectively. Ru has the largest surface free energy, Fe has the second largest, and Ir has the third largest.

Computationally, Rh, Ni, and Co also increase the Ag binding energy, while Pd, Pt, Cu, and Au decrease the Ag binding energy, although the decrease is only around 0.02 eV for the case of Au. This implies that for these clusters, sintering will be reduced in the case of Ru, Fe, and Ir, although the Ag binding energy compares the stability of the Ag_9X cluster to the Ag_8X cluster (after removal of one of the Ag atoms), so electronic shell effects can affect the results[35]. Ru, Fe, and Ir are all large surface free energy metals, which is consistent with our hypothesis that large surface free energy core metals will enhance stability and inhibit sintering.

The binding of the core metal X is also shown in Figure 1A and is proportional to the total binding energy of the bimetallic clusters. The core metal binding energy of the bimetallic clusters is consistently larger than for Ag. This is not necessarily a measure of the stability of the bimetallic particle versus monometallic particles, since the mixing energy between the monometallic clusters and the bimetallic clusters must be compared to determine if mixing is thermodynamically favored. The greater binding energy of the X atom reveals that core metals such as Ir, Rh, and Ru bond most strongly to the Ag than Ag, so clusters with these cores should have larger total stability. Essentially, the bonding between Ag and X is greater than the bonding between Ag and Ag, although some changes in the interaction with the support may also affect the core metal binding energy; Ir has the largest core binding energy of the elements studied here. These metals with enhanced stability are all high surface free energy metals which is consistent with our hypothesis, and the highest core metal binding energy for Ir suggests that it would be a reasonable choice for a core metal for synthesis of core-metal particles with enhanced stability.

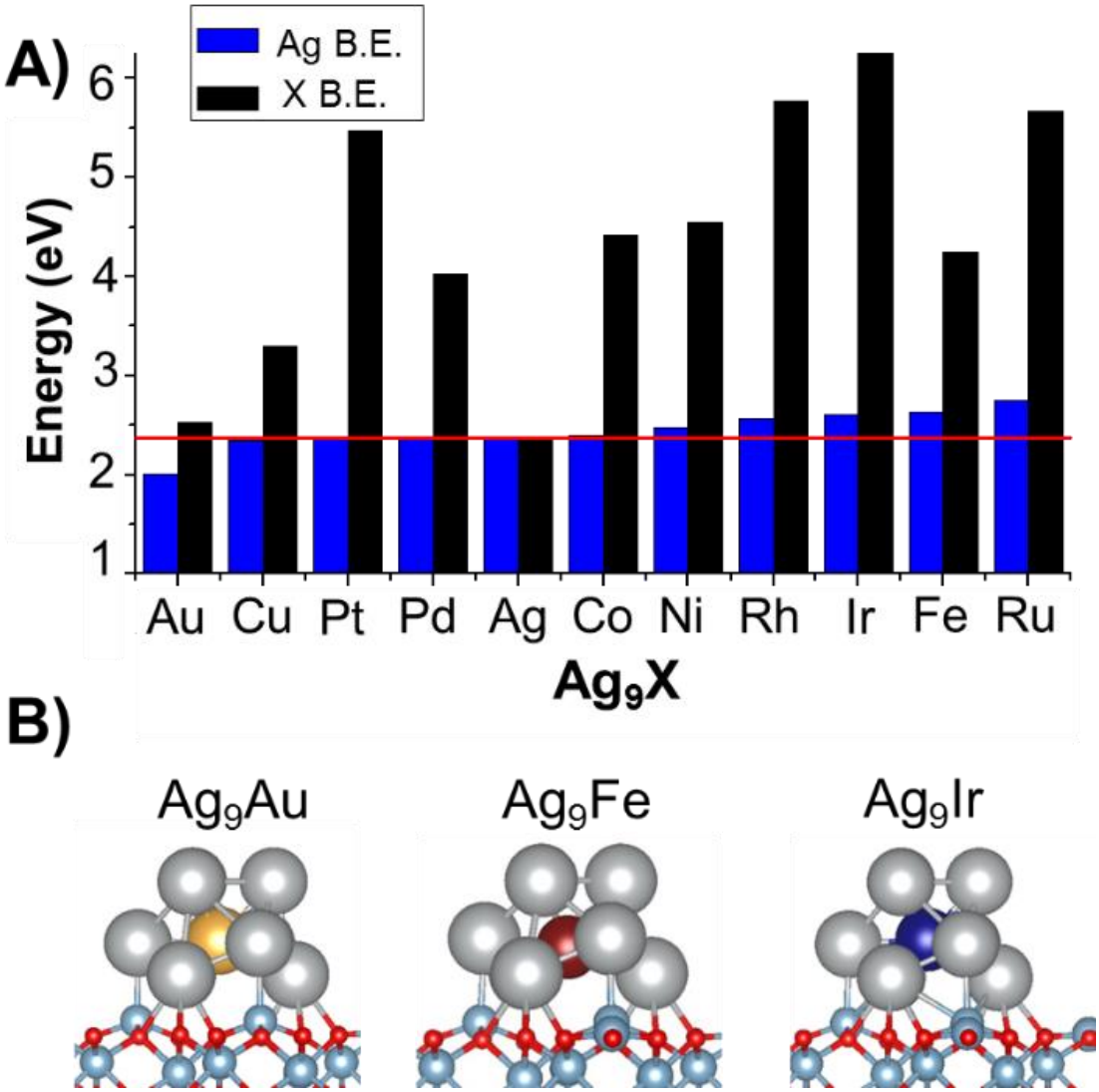

Figure 2.1: (A) The Ag and core binding energy for element X of Ag_9X on α-Al_2O_3(0001). (B) The structure of Ag_9Au, Ag_9Fe, and Ag_9Ir on α-Al_2O_3(0001). Silver atoms are silver, aluminum atoms are light blue, oxygen atoms are red, and Au, Fe, and Ir are gold, red, and blue, respectively.

Larger Ag-Ir bimetallic nanoparticles were examined to further test the hypothesis that bimetallic core-shell particles will have enhanced stability when the core metal corresponds to a large surface free energy metal with a shell metal having a lower surface free energy. The energetics of different structures of $Ag_{11}Ir_{11}$ clusters on α-Al_2O_3 (0001)

were examined, and by far the lowest energy structure was a core-shell structure where Ag existed as a shell on an Ir core, as shown in Figure 2. The mixing energy was calculated to be -0.87 eV using equation 3, and the negative value is evidence that the bimetallic core-shell cluster is more stable than the phase separated pure Ag and pure Ir clusters[36].

$$E(\text{Mixing}) = E(Ag_{11}Ir_{11}\_Al_2O_3) - \tfrac{1}{2} E(Ag_{22}\_Al_2O_3) - \tfrac{1}{2} E(Ir_{22}\_Al_2O_3) \quad (2.3)$$

A hybrid system was also investigated where a single atom of Ir is part of the shell that is otherwise made up of Ag and with an Ir core. We find this structure to be relatively low in energy and is 1.09 eV less stable than the Ir-core, Ag-shell structure but significantly more stable than the other isomers, and the mixing energy is +0.22 eV. The energy difference of 1.09 eV corresponds to an energy of 0.05 eV/atom or about 300° C, so it is not unreasonable for such structures to be found after heating at higher temperatures. For comparison, a series of alloy structures were calculated using the structure of the Ag_{22} cluster with positions of Ag or Ir randomly assigned. The lowest energy of these structures had a mixing energy of +2.04 eV which is 2.89 eV less stable than the Ag shell-Ir core structure. For an Ir shell-Ag core structure, the cluster is 4.09 eV less stable than the Ag shell-Ir core structure. The stability of the Ir core, Ag shell structure is due to stronger bonding between the Ir atoms. This offers further evidence that bimetallic particles become significantly more energetically stable when they have a core-shell structure where the core metal is a large surface free energy metal such as Ir, and the shell is a low surface free energy metal such as Ag.

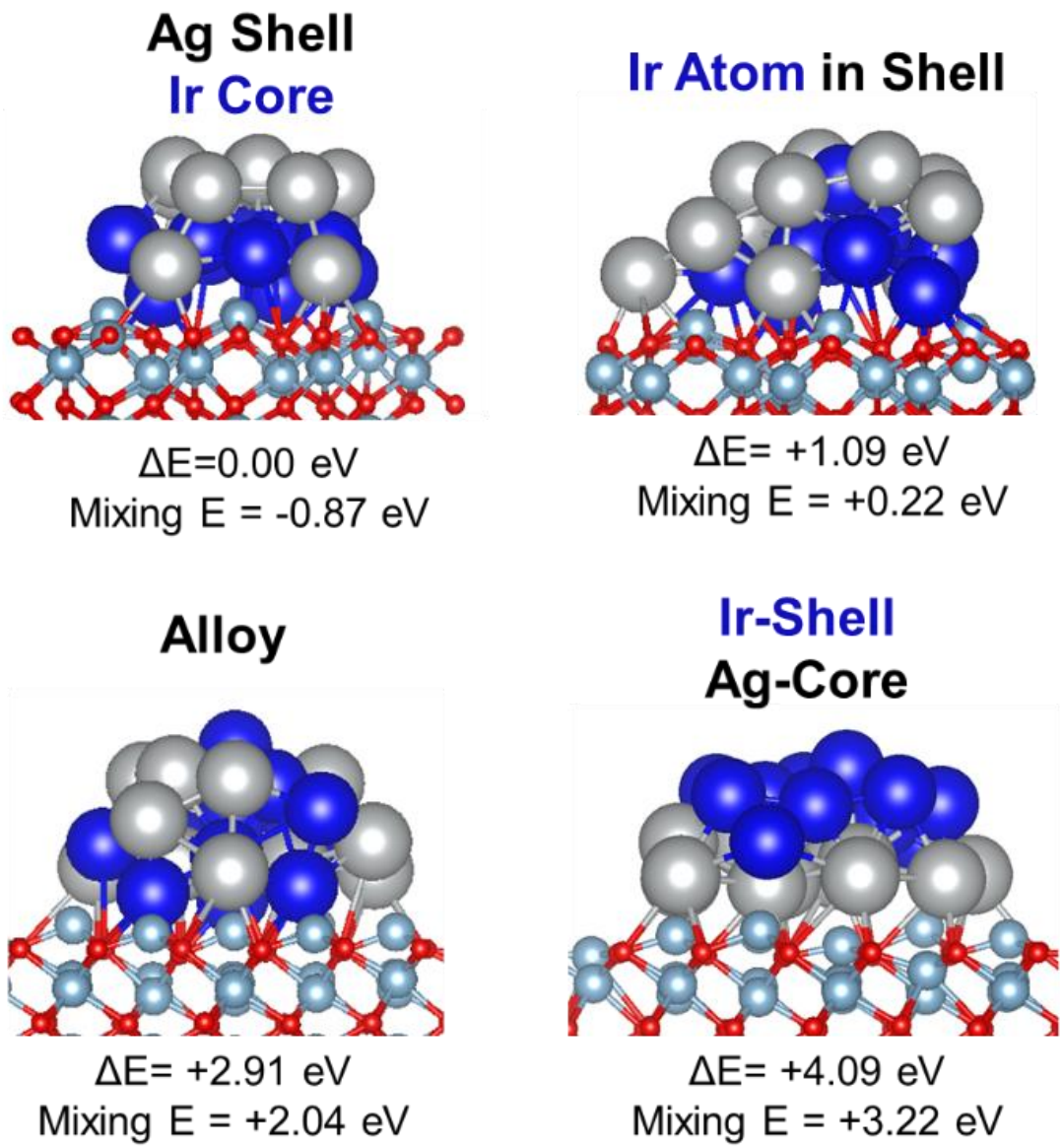

Figure 2.2: Structures, relative energies, and mixing energies of different $Ag_{11}Ir_{11}$ clusters on α-Al_2O_3(0001) with the Ag shell-Ir core structure (upper left), a structure with a single Ir atom in the Ag Shell (upper right), a representative alloy structure (lower left), and a Ir shell-Ag core structure (lower right). Silver atoms are silver, Ir atoms are blue, aluminum atoms are light blue, and oxygen atoms are red.

2.4.2 Catalyst preparation

Strong Electrostatic Adsorption (SEA) was used to prepare the Ir catalysts. Adsorption density of the iridium precursors over δ,θ-Al_2O_3 and γ-Al_2O_3 is plotted against pH (Figure 3). In the acidic pH region, anionic $IrCl_6^{2-}$ was adsorbed on the

alumina supports (PZC~8.4). At pH values near the PZC, only slight adsorption occurs. As the solution was acidified, the hydroxyl groups of alumina were protonated permitting the negatively-charged anionic Ir complex to adsorb at greater densities. The concurrent decrease in uptake in strong acidic mediums can be attributed to excessively strong ionic strength, where the electrostatic charge between the protonated surface and the Ir complex was weakened from other ions in solution. The maximum adsorption densities for these alumina supports were 0.75 and 1.1 μmol/m^2 of surface for δ,θ-Al_2O_3 and γ-Al_2O_3, respectively. This maximum adsorption occurred at a final pH ~4 for both aluminas.

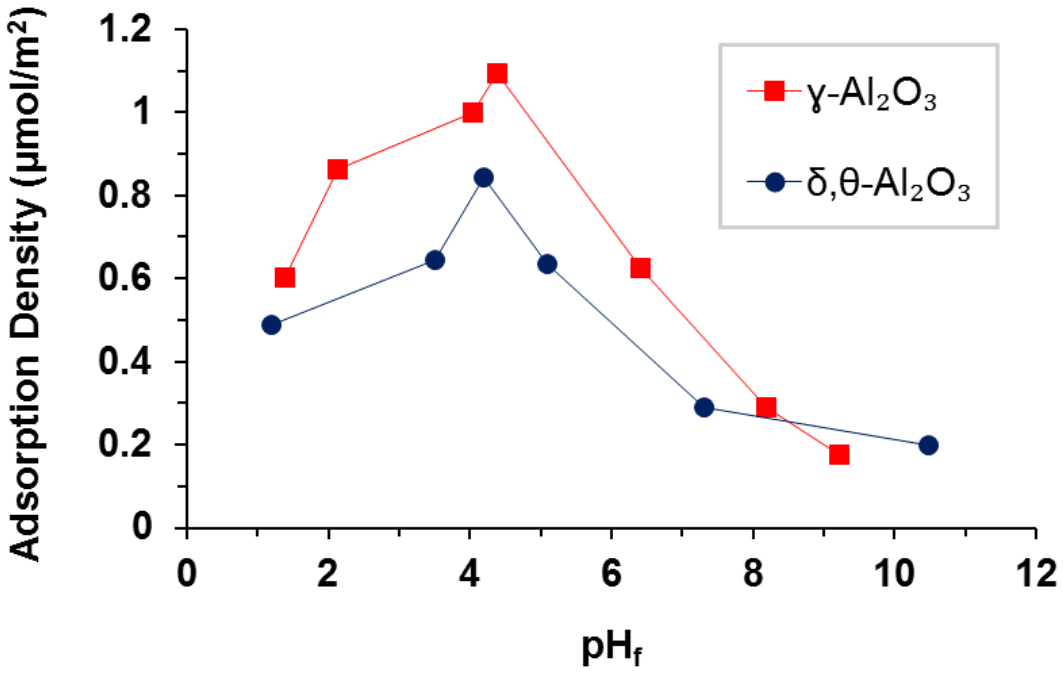

Figure 2.3: Adsorption of Ir complexes.

One limitation of SEA is that the weight loading of the catalyst is limited by the maximum adsorption density of the precursor and the surface area of the support. Therefore, only a limited amount of metal was adsorbed in a single SEA cycle for the

lower surface area θ/δ-Al_2O_3 support; a second cycle of SEA was required for this support. Only one SEA cycle was required for γ-Al_2O_3 since the surface area was substantially higher. The final weight loadings of Ir on δ,θ-Al_2O_3 and γ-Al_2O_3 were 1.0 and 3.2 wt% Ir, respectively. Since the surface area of γ-Al_2O_3 (164 m^2/g) was considerably higher than δ,θ-Al_2O_3 (37m^2/g), a higher loading was used to better attain similar surface concentrations of Ir on the two supports. Initial particles sizes were below the limit of detection (<1.5 nm) using XRD line broadening. Particle size determinations were thus determined by H_2 chemisorption and the data shown at a later point.

Electroless Deposition (ED) was used to prepare controlled, partial-shell layers on the Ir surfaces, using the methodology from previous work for bimetallic Ag-Ir core-shell structures [20]. Briefly, potassium silver cyanide, $KAg(CN)_2$, and potassium gold cyanide, KAu(CN), were used as Ag and Au precursors, and hydrazine was used as the RA. The ED bath was maintained at pH 10, above the support PZC, to prevent any electrostatic interactions between the support and either $Ag(CN)_2^-$ or $Au(CN)_2^-$. The batch kinetics of Ag deposition on δ,θ-Al_2O_3 and γ-Al_2O_3 are shown in Figure 4A and B, respectively. For ED of Ag^+ the first 30 min were used to determine whether the ED bath was thermally stable with respect to reduction of $Ag(CN)_2^-$ by the high concentration of N_2H_4. After 30 min, the 1.0% Ir/δ,θ-Al_2O_3 catalyst was added to the bath and deposition began. This was not done for deposition of $Ag(CN)_2^-$ on 3.2 wt% Ir/γ-Al_2O_3. The rates of deposition were fastest in the first 15 minutes when the N_2H_4 and $Ag(CN)_2^-$ concentrations were highest. A fresh aliquot of N_2H_4 was added every 30 mins to offset the instability of N_2H_4, which decomposes very quickly to evolve H_2, i.e., the rate of N_2H_4 decomposition to form N_2 and H_2 is similar to the rate of activation on the Ir surface. The deposition slowed as the

process continued for a number of reasons: (1) kinetics were dependent on concentrations of the Ag^{+} and Au^{+} salts in solution, (2) the weak affinity for auto-catalytic deposition of Ag^{+} on Ag^{o} using hydrazine as the RA, and (3) the byproduct CN^{-} from the reduction of the cyano salts is isoelectronic with CO, which is known to strongly adsorb on platinum group metals which prevents further deposition.

To offset the sluggish deposition of Ag at higher coverages, the temperature of deposition was increased from 25 to 75°C. Figure 4A shows that raising the temperature of deposition from 25 to 50 to 75°C substantially increased the extent of deposition for the 2.0ML target loading.

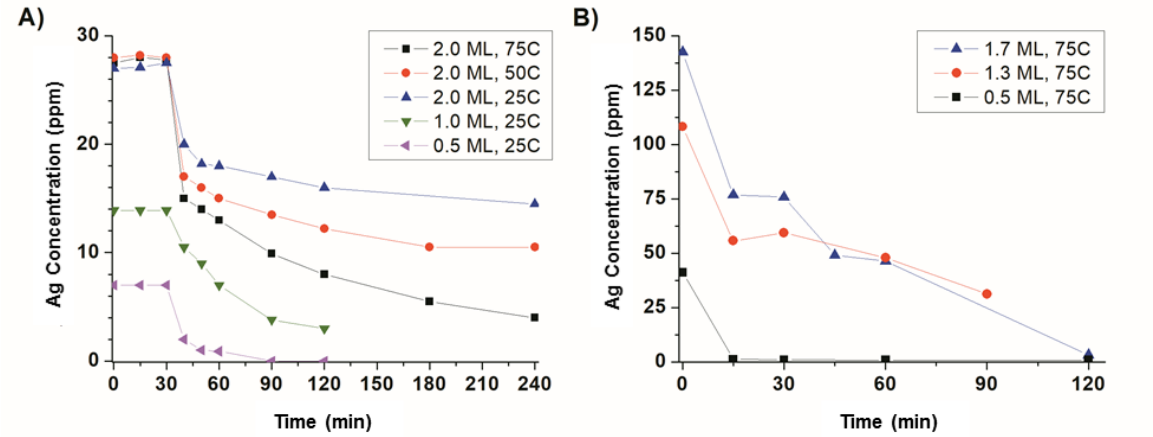

Figure 2.4: Electroless Deposition kinetics of (A), Ag on 1.0 wt% Ir/δ,θ-Al_2O_3 and (B), Ag on 3.2 wt% Ir/γ-Al_2O_3. In (A), for first 30 min, bath stability was tested; only the reducing agent and Ag salt were present in bath. After 30 min, 1.0 wt% Ir/δ,θ-Al_2O_3 added to ED bath.

A summary of the bimetallic catalysts synthesized by ED are shown in Table 1. Weight percentages of the shell component and experimental coverages were determined by atomic absorption spectroscopy and H_2 chemisorption following reduction at 200°C, respectively. For increasing weight loadings of Ag deposited on 1 wt% Ir/δ,θ-Al_2O_3,

chemisorption results indicate Ag coverages increase from 0.22 to 0.93 ML coverage, based on monodisperse coverages of Ag on Ir (Ag/Ir = 1). Since at 25°C and following pretreatment at 200°C, Ag does not dissociatively adsorb H_2, the coverage of Ag on Ir can be determined from the reduction in H_2 uptake compared to the monometallic, 1 wt% Ir/δ,θ-Al_2O_3. From Table 1 we see that ED of 0.14 wt% Ag lowers the H_2 uptake by 22% relative to the monometallic 1 wt% Ir sample; thus, the coverage of Ag on Ir is θ_{Ag} = 0.22, and so on. However, the results for 3.2 wt% Ir/γ-Al_2O_3 showed only a marginal increase in Ag coverage (0.8 to 0.9) as the weight loading of Ag deposited by ED varies from 0.73 to 2.8 wt% Ag. It should be noted in passing that the dispersion of the Ir particles on the 3.2 wt% Ir/γ-Al_2O_3 was much higher at 1.0, so the unusually small Ir particles from the SEA preparation may have caused the unexpected behavior and changed Ag coverage from monodisperse (Ag/Ir = 1) to some other value.

Table 2.1: Summary of Bimetallic Core-Shell Catalysts.

Core	**Support**	**Shell Metal**	**Shell wt%**	**θ_{target} (ML)**	**θ_{theo} (ML)**	**θ_{exp} (ML)**
1.0 wt% Ir	δ,θ-Al_2O_3	Au	0.24	0.5	0.43	0.18
		Ag	0.14	0.5	0.52	0.22
			0.21	1.0	0.81	0.40
			0.24	2.0	0.92	0.62
			0.35	2.0	1.31	0.87
			0.47	2.0	1.77	0.93
3.2 wt% Ir	γ-Al_2O_3	Ag	0.73	0.5	0.41	0.80
			1.5	1.3	0.85	0.88
			2.8	1.7	1.60	0.90

Chemisorption values for the unmodified 1.0 wt% Ir and 3.2 wt% Ir samples gave H_2 uptakes corresponding to dispersions of 0.49 and 1.0, respectively, with calculated particle sizes of 2.3 nm and 1.1 nm, also respectively[37]. The fractional coverages of Ag on Ir are shown graphically in Figure 5. After deposition this series of catalysts with different coverages was then annealed at increasing temperatures (400, 600, and 800°C) to determine catalyst stability.

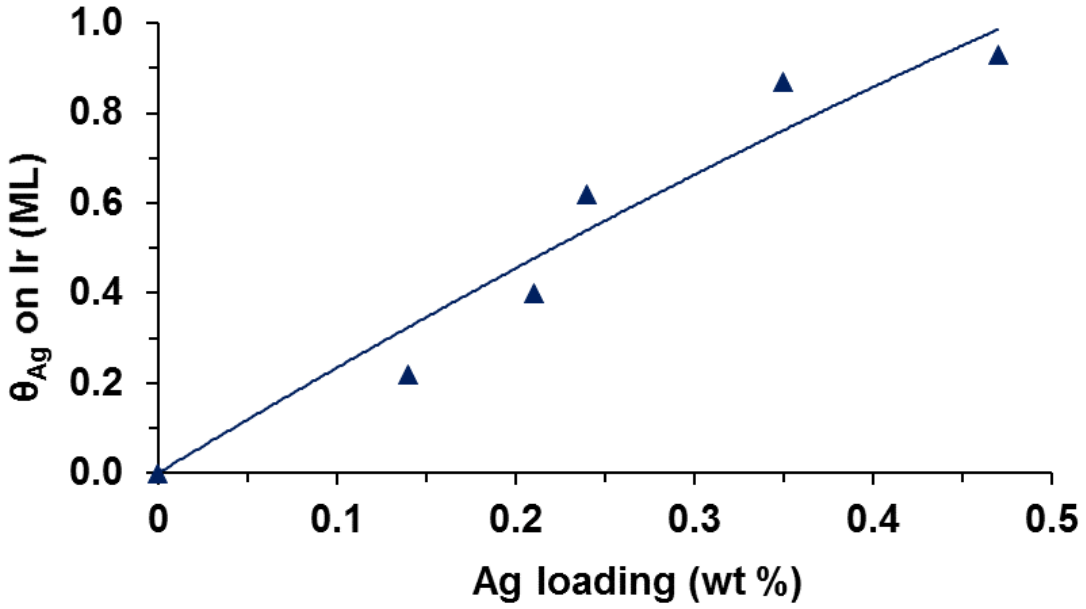

Figure 2.5: Estimated coverage of Ag on Ir using chemisorption versus loading of Ag for the δ,θ-Al_2O_3 support.

2.4.3 Particle size analysis

The particle sizes of these catalysts were examined using STEM images and XRD patterns. Comparisons will be made with H_2 chemisorption results discussed in much greater detail in a later Section. We note that the particle sizes of the catalysts are summarized in Table 2. The initial particle sizes of the monometallic Ir catalyst on δ,θ-Al_2O_3 were d_{chem} = 2.3 nm, d_n= 1.4 nm (number average from STEM), and d_{XRD} = <2 nm.

After the annealing treatments of 200, 400, 600, and 800°C, the final particle sizes of the monometallic 1 wt% Ir/δ,θ-Al_2O_3 were d_{chem} = 21 nm, d_n= 43 nm, and d_{XRD} = 26 nm. The two particle size measurements obtained from chemisorption and XRD are in good agreement with each other. The larger particle size determined from STEM measurements is likely due to an insufficient number of particles being measured, which favors larger particle size determination. Regardless, the significant increase in particle size was due to severe metal sintering after pretreatment at high temperatures. A clear suppression of nanoparticle sintering is observed for the Ag-Ir bimetallic particles. After the high temperature pretreatments, the XRD bimetallic particle sizes were between 19 - 22nm (shown in insert of Figure 6). Moreover, the Ir (111) metallic peaks in the bimetallic catalysts shown at 2θ = 40.7° in Figure 6 are reduced in intensity compared to the monometallic Ir catalyst. This reduction of the Ir (111) peak suggests a bimodal distribution of the Ir, where many smaller Ir particles also exist. No metallic Ag (111) peaks at 2θ = 38.1° were observed by XRD for the δ,θ-Al_2O_3 bimetallic catalysts. A monometallic Ag catalyst was annealed under the same conditions at 800 °C to compare with the bimetallic catalysts. XRD results of the annealed monometallic Ag catalyst indicated particle sintering to 29 nm. Thus, the bimetallic nanoparticles had increased resistance to sintering with regard to both the monometallic Ag and Ir counterparts. We had anticipated lower particle sizes for Ag, but the resistance of Ir to sintering was unanticipated.

Table 2.2: Summary of particle sizes of catalysts. For bimetallic catalysts the particle sizes are for Ir.

Catalyst	T (ºC)	Chemisorption (nm)	XRD (nm)	STEM (nm)
1%Ir/δ,θ-Al_2O_3	200	2.3	<2	1.4
	400	2.3	<1.5	-
	600	24	-	-
	800	21	26	43
0.14%Ag-1%Ir/δ,θ-Al_2O_3	200	2.9	-	-
	400	2.4	-	-
	600	6.4	-	-
	800	11	20	-
0.21%Ag-1%Ir/δ,θ-Al_2O_3	200	3.8	-	-
	400	1.4	-	-
	600	1.6	-	-
	800	3.8	22	-
0.35%Ag-1%Ir/δ,θ-Al_2O_3	200	8.7	-	1.5
	400	1.2	-	1.6
	600	3.6	-	-
	800	5.3	22	6.7
0.47% Ag-1%Ir/δ,θ-Al_2O_3	200	16	-	-
	400	5.0	-	-
	600	5.7	-	-
	800	12	22	-
3.2% Ir/γ-Al_2O_3	200	1.1	<2	-
	400	1.2	-	-
	600	8.0	-	-
	800	17	23	56
0.73% Ag-3.2%Ir/γ-Al_2O_3	200	5.6	-	-
	400	2.7	-	-
	600	2.2	-	-
	800	3.2	-	-
1.5% Ag-3.2%Ir/γ-Al_2O_3	200	9.2	-	-
	400	4.4	-	-
	600	2.1	-	-
	800	3.2	-	-
2.8% Ag-3.2%Ir/γ-Al_2O_3	200	11	-	-
	400	7.0	-	-
	600	2.9	-	-
	800	3.3	-	1.6

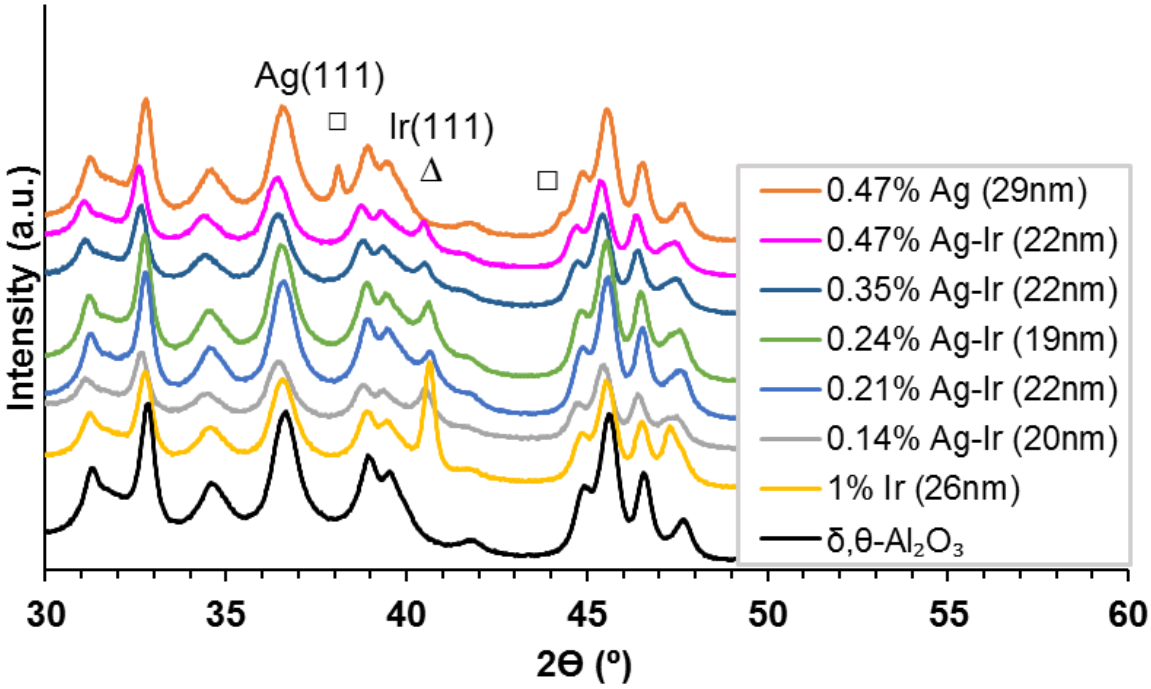

Figure 2.6: XRD diffraction patterns of monometallic and bimetallic catalysts supported on δ,θ-Al_2O_3 after annealing at 800°C. XRD particle sizes are shown in the parenthesis (for bimetallic catalysts the particle sizes are for Ir). Bimetallic catalysts contain 1 wt% Ir.

A similar XRD analysis was performed for the γ-Al_2O_3 annealed catalysts. The initial particle size of the Ir on γ-Al_2O_3 was ~2nm by chemisorption and <2nm from XRD. After annealing treatments at 800°C, the Ir severely sintered as observed by a large Ir (111) peak in the XRD pattern in Figure 7. The final particle size for the 3.2 wt% Ir/γ-Al_2O_3 was d_{chem} = 17 nm, d_n= 56 nm, and d_{XRD} = 23 nm. Again, chemisorption and XRD bulk particle sizes are in quite good agreement with each other. When 0.73 wt% Ag was added as a shell component, both Ir and Ag were again stabilized as indicated by the absence of the Ag (111) peak and a less intense Ir (111) peak. Both Ag (111) and Ir (111) peaks existed in the higher weight loadings of Ag (1.5 and 2.8 wt%) annealed catalysts, but both peaks were less intense than either the Ag or Ir monometallic analogues. These low XRD intensities signify that a bimodal distribution of Ir and Ag nanoparticles must

coexist; when XRD detected some large clusters, many small Ag-Ir clusters must have remained below the limit of XRD detection.

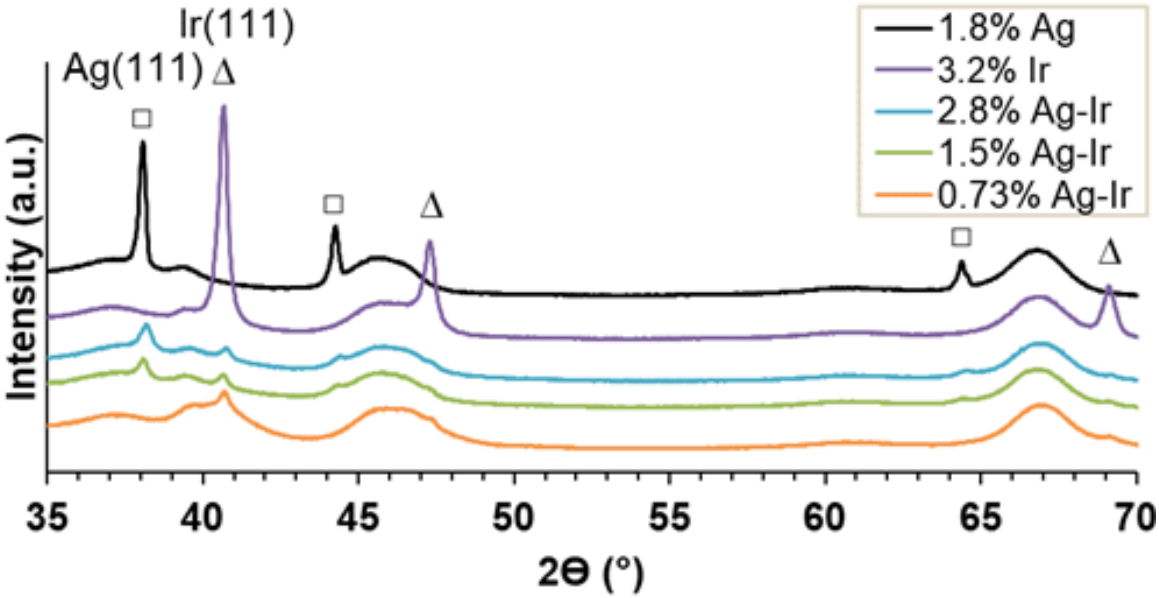

Figure 2.7: XRD diffraction patterns of monometallic and bimetallic γ-Al_2O_3 catalysts after annealing at 800°C.

To summarize the XRD data, monometallic Ir and monometallic Ag catalysts sintered on both alumina supports. Anchoring Ag as a shell by ED prevented the sintering of Ag compared with the monometallic Ag catalysts on the Al_2O_3 supports. This increased stability of Ag agrees with SFE principles. Surprisingly, the addition of the Ag shell also decreased the sintering of Ir.

STEM was used to confirm the bimodal distribution and stabilization of the Ag-Ir nanoparticles. In Figure 8, STEM images and particle size distributions are shown after the different pretreatment temperatures. The monometallic 1.0 wt% Ir/δ,θ-Al_2O_3 sintered from an initial d_n= 1.4 nm to a d_n = 43 nm (Figure 8A and B); all of the Ir existed as large particles. This severe sintering was prevented by addition of Ag. The bimetallic Ag-Ir

catalyst (0.35Ag-1.0Ir wt.%) started with an initial d_n = 1.5 nm and sintered to d_n= 1.6 nm and d_n = 6.7 nm after pretreatments of 400 and 800°C, respectively (Figure 8C, D and E). Many of these Ag-Ir nanoparticles remained small (<5nm) after 800°C. The images taken after 400°C annealing (Figure 8D) showed virtually no particle size difference from the initially prepared size. This validates Ir's resistance to sintering up to 400°C which was observed from chemisorption in Figures 9 and 10. However, the unchanged particle size of the δ,θ-Al_2O_3 bimetallic catalysts between the initial state at 200°C and after a pretreatment of 400°C cannot explain the abnormally high H_2 uptake of these Ag-Ir bimetallic catalysts after pretreatments at intermediate temperatures. If an Ag shell were to sinter and expose the Ir surface, the H_2 uptake would not surpass the maximum H_2 uptake of the monometallic Ir.

A STEM comparison was also made between an annealed monometallic Ir (3.2 Ir wt.%) and an annealed bimetallic Ag-Ir catalyst (2.8Ag-3.2Ir wt.%) supported on γ-Al_2O_3. Both γ-Al_2O_3 catalysts were initially small, but after annealing at 800°C, there were large difference in particle size (Figures 8F and G). The bimetallic Ag-Ir catalyst (Figure 8F) particle size was mostly unchanged at d_n= 1.6 nm, and the monometallic catalyst severely sintered to d_n= 56 nm (Figure 8G). The results of very little sintering for the bimetallic system over γ-Al_2O_3 agrees with the minute Ir (111) XRD peaks and high H_2 capacity after 800°C shown in Figures 7 and 10, respectively. The STEM images of both Al_2O_3 supports at various wt. loadings and Ag coverages suggest a clear indication that the bimetallic Ag-Ir catalysts are more sinter resistant. The particle size distribution for all catalyst was displayed on Figure S1.

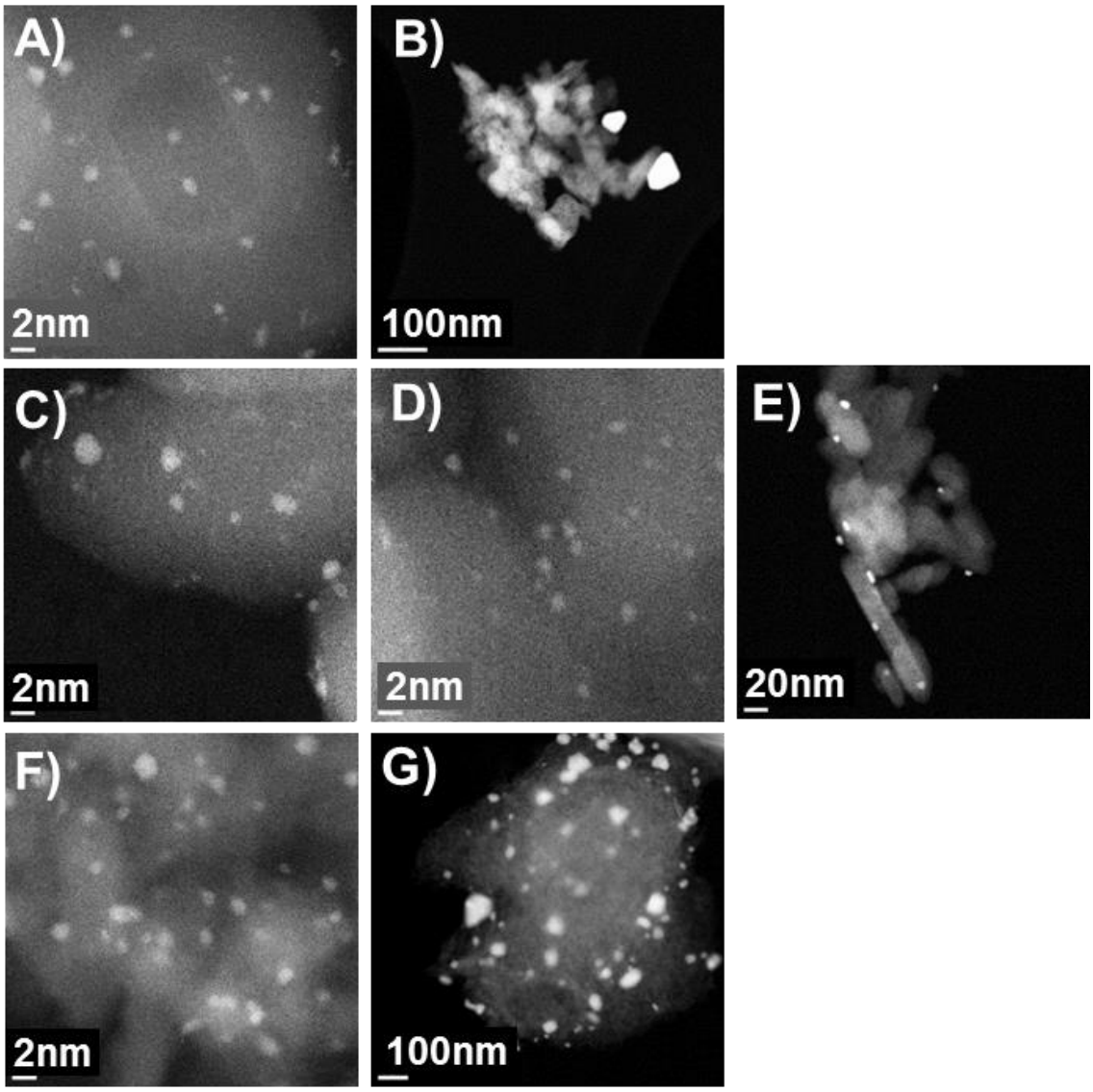

Figure 2.8: STEM images of (A) 1% Ir/δ,θ-Al_2O_3 fresh; (B) 1% Ir/δ,θ-Al_2O_3 at 800°C; (C-E) 0.35% Ag-Ir/δ,θ-Al_2O_3 at 200°C, 400°C and 800°C, respectively; (F) 2.8% Ag-Ir/γ-Al_2O_3 at 800°C; (G) 3.2% Ir/γ-Al_2O_3 at 800° C.

2.4.4 Chemisorption results

The chemisorption results of the δ,θ-Al_2O_3-supported Ag-Ir bimetallic catalysts are shown in Figure 9 and summarized in Table 3. The chemisorption data at 200°C show the expected decrease in H_2 uptake as higher levels of Ag are deposited on the Ir surface.

Results also show the 1.0 wt% Ir catalyst was thermally stable up to 400°C in flowing Ar; no change in H_2 uptake from chemisorption between 200 and 400°C was observed.

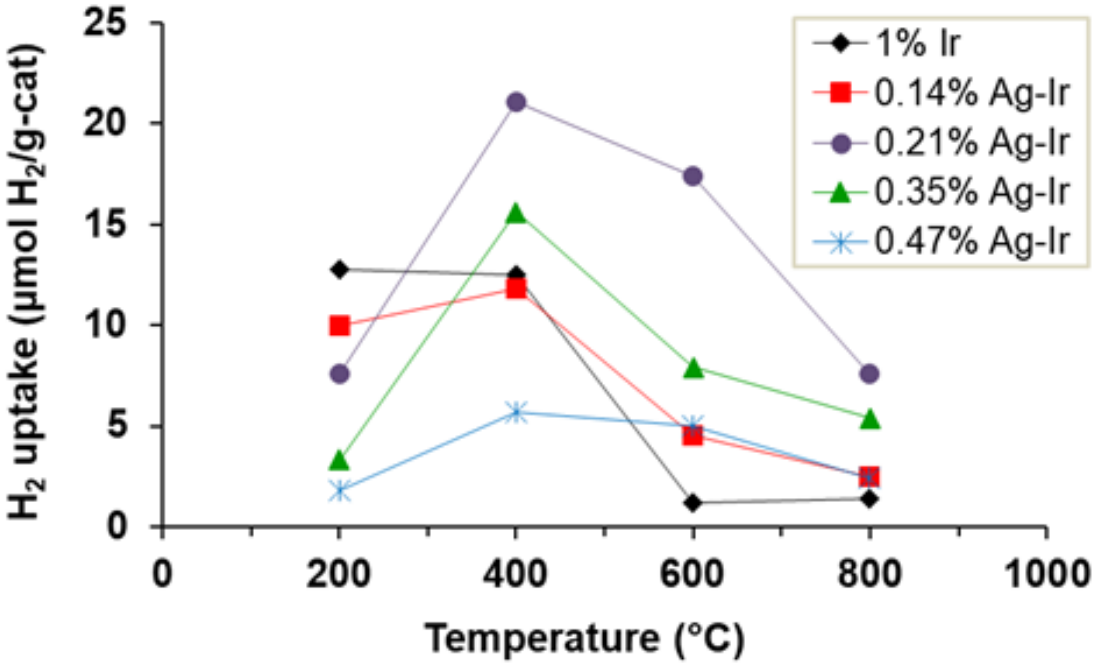

Figure 2.9: Chemisorption of H_2 on annealed Ag-Ir catalysts supported on δ,θ-Al_2O_3.

However, at temperatures ≥ 600°C, the H_2 uptake decreased dramatically from 12.5 to 1.2 µmol/g catalyst, indicative of severe nanoparticle sintering. However, for all Ag-Ir samples, H_2 uptakes were actualy higher after annealing at 400 and 600°C than at 200°C. The effect is greatest for the sample with 0.21 wt% Ag where the H_2 uptake was 3x higher than at 200°C. Even at 800°C, the Ag-Ir samples exhibited higher H_2 uptakes than the unmodified Ir sample; the ordering was completely inverted from what it was at 200°C. It is intuitive that H_2 uptake of the bimetallic catalysts should not surpass the monometallic catalyst unless the effective stoichiometry of adsorption for the H/Ir site is altered or the surface of Ag can also chemisorb H or provide adsorption sites as in the

case of H-spillover or that the addition of Ag gives re-dispersion of Ir at high temperatures.

Table 2.3: The chemisorption results of the Ag-Ir bimetallic system supported on δ,θ-Al_2O_3.

	1%Ir	**0.14%Ag-Ir**	**0.21%Ag-Ir**	**0.24%Ag-Ir**	**0.35%Ag-Ir**	**0.47% Ag-Ir**
θ_{Ag} at 200°C	0	0.22	0.40	0.62	0.87	0.93
Conditions	H_2 uptake at 40°C following pretreatments, (μmol H_2/g-cat)					
Reduce in H_2 at 200°C, 2 hrs	12.8	10.0	7.6	4.5	3.3	1.8
Heat in Ar at 400°C, 4 hrs	12.5	11.8	21.1	17.8	15.6	5.7
Heat in Ar at 600°C, 4 hrs	1.2	4.5	17.4	11.2	7.9	5.0
Heat in Ar at 800°C, 4 hrs	1.4	2.5	7.6	4.6	5.4	2.4

The same annealing/chemisorption treatments were performed on a series of Ag-Ir bimetallic catalysts supported on γ-Al_2O_3 and shown in Figure 10. The 3.2 wt% Ir/γ-Al_2O_3 also exhibited similar chemisorption trends to the monometallic 1.0 wt% Ir/δ,θ-Al_2O_3 after the various annealing pretreatments. The Ir/γ-Al_2O_3 sample was also stable up to 400°C, with only a slight deactivation compared to annealing at 200°C. At 600°C, there is a significant loss of active sites from 73 μmol H_2/g catalyst to 11 μmol H_2/g catalyst. The difference in the initial amounts of H_2/g adsorbed for 1.0 wt% and 3.2 wt% loadings of Ir on Al_2O_3 catalysts was expected based simply on Ir weight loading; however, the dispersion of the Ir particles for the 1.0 wt% Ir/θ,δ-Al_2O_3 sample was 0.49 versus 1.0 for the 3.2 wt% Ir/γ-Al_2O_3 sample .

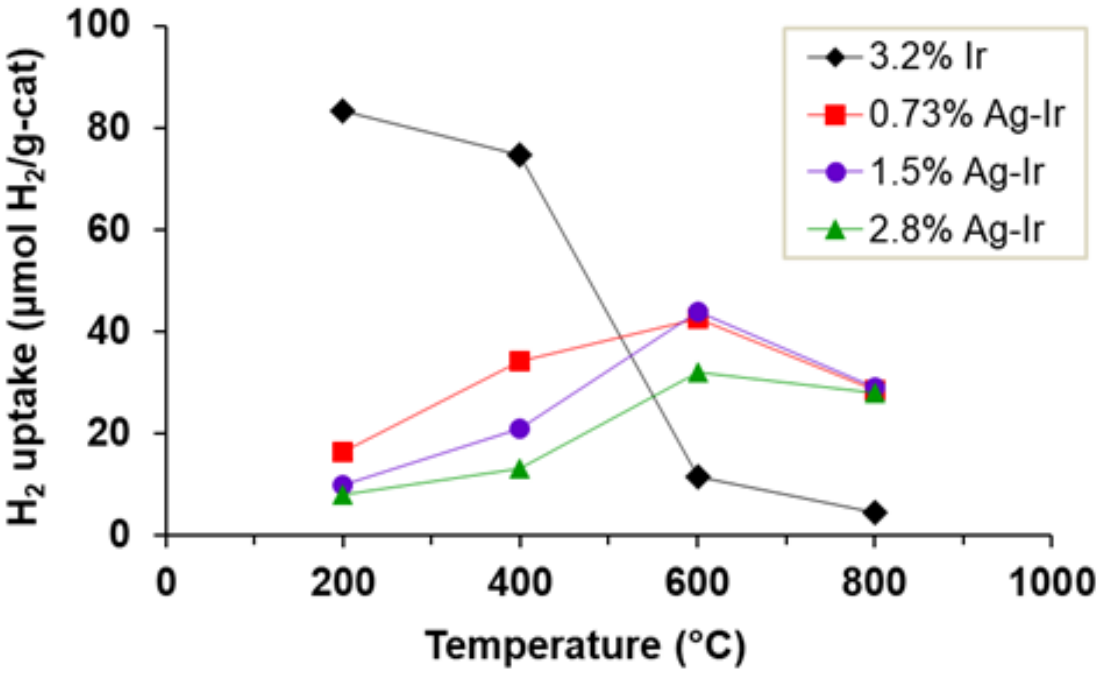

Figure 2.10: Chemisorption of H_2 on annealed Ag-Ir catalysts supported on γ-Al_2O_3.

When Ag was deposited on 3.2 wt% Ir/γ -Al_2O_3, the initial H_2 uptakes at 200C for the bimetallic system was reduced by 80%, agreeing with higher Ag coverages giving lower initial H_2 uptakes. After annealing at 400, 600, and 800°C, the Ag-Ir bimetallic catalysts again exhibited increased capacity for H_2 compared to the values at 200°C indicating the same anomalous behavior. However, at no point was the H_2 capacity for the γ-Al_2O_3 bimetallic system higher than the maximum H_2 capacity of the monometallic Ir catalyst at 200°C. This suggests the mechanism of enhancement of Ag to improve H_2 uptake may be different for ultra-small Ir particles with dispersions ~ 1. The migration of Ag into the bulk of Ir is unlikely, since at a Dispersion of 1.0 there is no bulk and Ag and Ir have not been reported to form alloys[38]. In this case, Ag may primarily stabilize Ir particles to prevent extreme sintering. The H_2 uptake values for the γ-Al_2O_3 bimetallic

catalysts after treating at 800°C were higher than for the monometallic Ir catalyst, which supports the ability of Ag to stabilize Ir particle sizes.

Finally, to illustrate these anomolous H_2 uptakes were not limited to Ag-Ir particles, a similar series of Au-Ir/δ,θ-Al_2O_3 catalysts were prepared that exhibited the same behavior of elevated H_2 uptake at 400 and 600°C. A representative chemisorption plot is shown in Figure 11 that compares the optimum coverages of both Ag and Au on Ir for enhanced H_2 chemisorption.

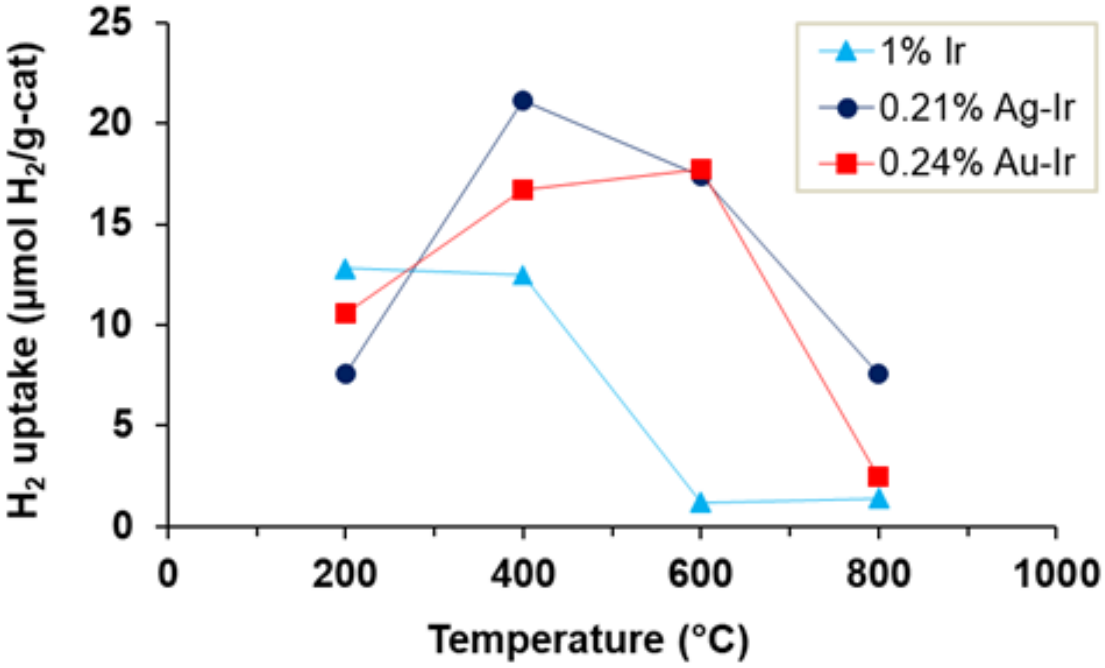

Figure 2.11: Comparison of Ag-Ir and Au-Ir catalysts for H_2 adsorption.

2.4.5 TPD of H_2

Temperature programmed desorption of H_2 (adsorbed at 40°C) following *in situ* annealing at 400°C in flowing Ar was conducted to better understand the sites and energetics giving rise to the higher H_2 adsorption values. The TPD results in Figure 12 show desorption spectra for unmodified 1% Ir/θ,δ-Al_2O_3 and three different coverages of Ag on Ir. All Ag-Ir catalysts show (at least) two other lower temperature H_2 desorption peaks in addition to the H_2 desorption peak centered at ~275°C attributed to Ir; the larger peak was centered at 90-100°C and the other at 170-180°C. The peaks were observed for all bimetallic Ag-Ir samples. It was not possible to quantitatively compare desorption amounts (no response factor determined) for the different catalysts although all peak intensities were normalized to 0.10 g of sample however. Regardless, the TPD results corroborate the chemisorption experiments and indicate the additional H_2 capacity is due to more weakly-bound H than normally exists on surface Ir sites. Later discussion of the XPS and DFT results indicate that H spillover on to adjacent Ag sites and/or multiple H atoms on special Ir sites are likely responsible. Most likely, H atoms adsorbed on Ag or multiple H atoms per Ir site would be more weakly adsorbed than one H per surface Ir atom.

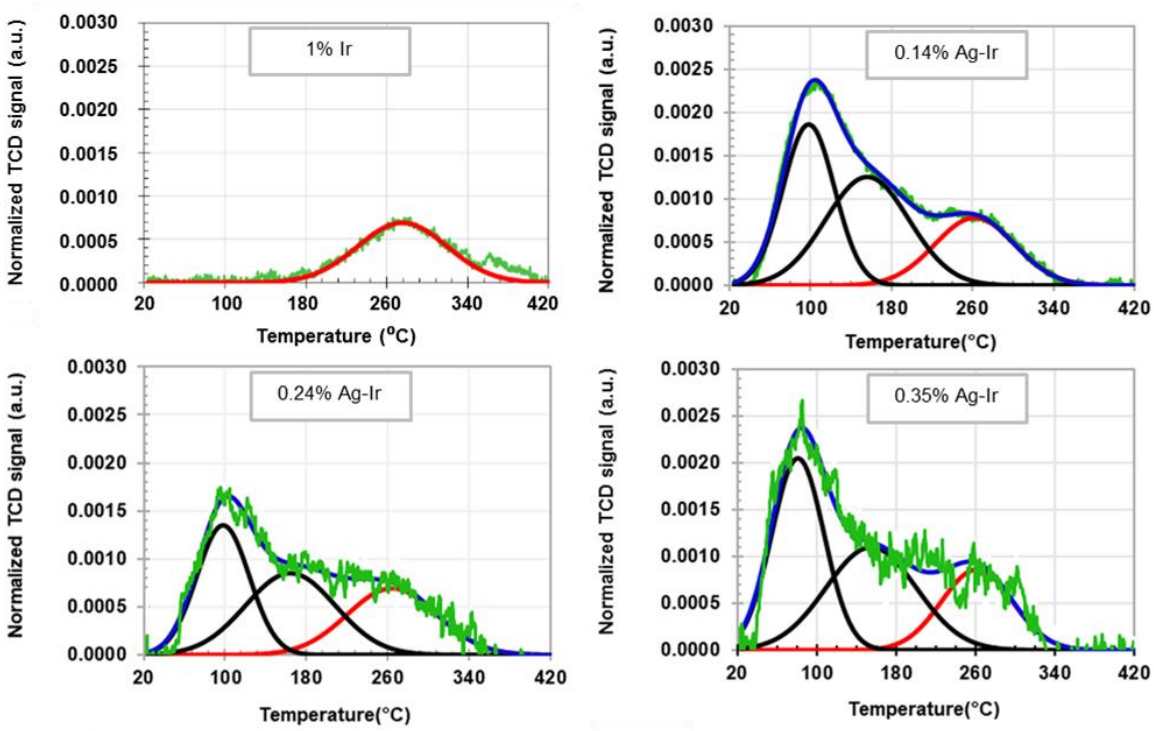

Figure 2.12: TPD of H_2 from 1% Ir and selected Ag-Ir bimetallic catalysts that have been annealed at 400°C immediately before TPD experiments were conducted. Ramp rates during TPD were 10°C/min for all samples and H_2 was initially adsorbed at 40°C.

Figure 9 had shown that the Ag-Ir catalysts annealed at 800°C exhibited higher H_2 uptakes than unmodified Ir and the results in Figure 13 confirm those results. The 1% Ir sample gave no observable H_2 desorption, while the 0.24% Ag-1.0% Ir/θ,δ-Al_2O_3 sample gave measurable H_2 desorption with at least four desorption peaks, including the low temperature peaks found after annealing at 400°C. Thus, the unusual behavior of the Ag-Ir system persists even at 800°C. The magnitude of the desorption peak at ~260°C also suggests that Ag has apparently stabilized the Ir particle from undergoing sintering.

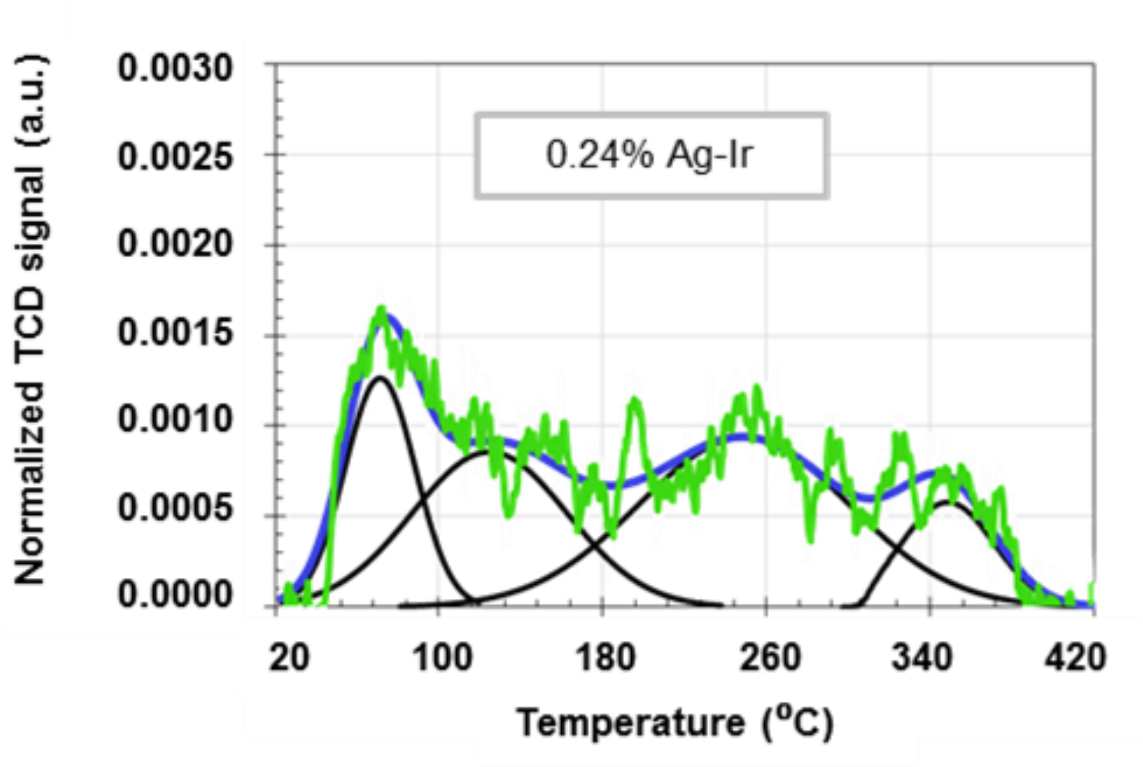

Figure 2.13: TPD of H_2 from 0.24% Ag-1.0% Ir/θ,δ-Al_2O_3 with θ_{Ag} = 0.62 annealed at 800°C. There was no observable TPD of H_2 from the base 1.0% Ir/θ,δ-Al_2O_3 catalyst.

2.4.6 Computational Study of H_2 Adsorption

In order to understand the observed trends in H_2 uptake on Ag/Ir nanoparticles, H_2 binding energies to a model $Ag_{11}Ir_{11}$ core-shell particle were investigated. Four hypotheses were tested to determine the weakly bound H that desorbs as H_2, seen in TPD experiments. We were also interested in understanding the unusually large H_2 adsorption for the Ag-Ir particles after annealing at T ≥ 400°C. Firstly, charge transfer from Ag to Ir in core-shell particles might activate the Ag surface to permit dissociative H_2 adsorption and binding directly on Ag. Secondly, multiple H atoms might bind to a single surface Ir atom surrounded by Ag atoms in the shell. Thirdly, H spillover to Ag could occur from dissociatively adsorbed H on Ir. Fourthly, reconstruction could result in a core Ir atom diffusing to the surface due to energetics of H binding and the reconstruction energy

might lower the binding energy of H on that reconstructed Ir site. To test these concepts, the binding energy of H atoms was determined to evaluate whether these hypotheses were energetically feasible.

The H_2 binding energies on pure Ag and Ir clusters placed on α-Al_2O_3 (0001) were first determined. The binding energy of H_2 to Ag is 0.17 eV and the binding energy of H_2 to Ir is 2.99 eV, as shown in Figure 14A and 14B. The H_2 binding energy was calculated using Eq. 4.

$$H_2 \text{ B.E.} = E(Ag_xIr_y\_Al_2O_3) + E(H_2) - E(H_2Ag_xIr_y/Al_2O_3) \quad (2.4)$$

The high B.E. of H_2 for the Ir cluster is consistent with the high desorption temperature of H_2 (~280°C) seen in the TPD experiments, and the weak binding of Ag clusters is consistent with pure Ag particles having no H_2 uptake. The case for the Ag shell on top of Ir was next considered in Figure 14C. The binding energy of H_2 on Ag in the shell is 0.13 eV and is virtually the same as for pure Ag, suggesting that the Ag is not activated by Ir, so this activation was not the source of the excess and more weakly bound H_2. Figure 14D shows an Ir atom surrounded by Ag in the shell; the H_2 binding energy is 2.21 eV, somewhat less than what is seen for pure Ir, although still quite large. This suggests that isolated Ir atoms can strongly and dissociatively bind H_2 and that two H atoms per single Ir site is energetically favorable.

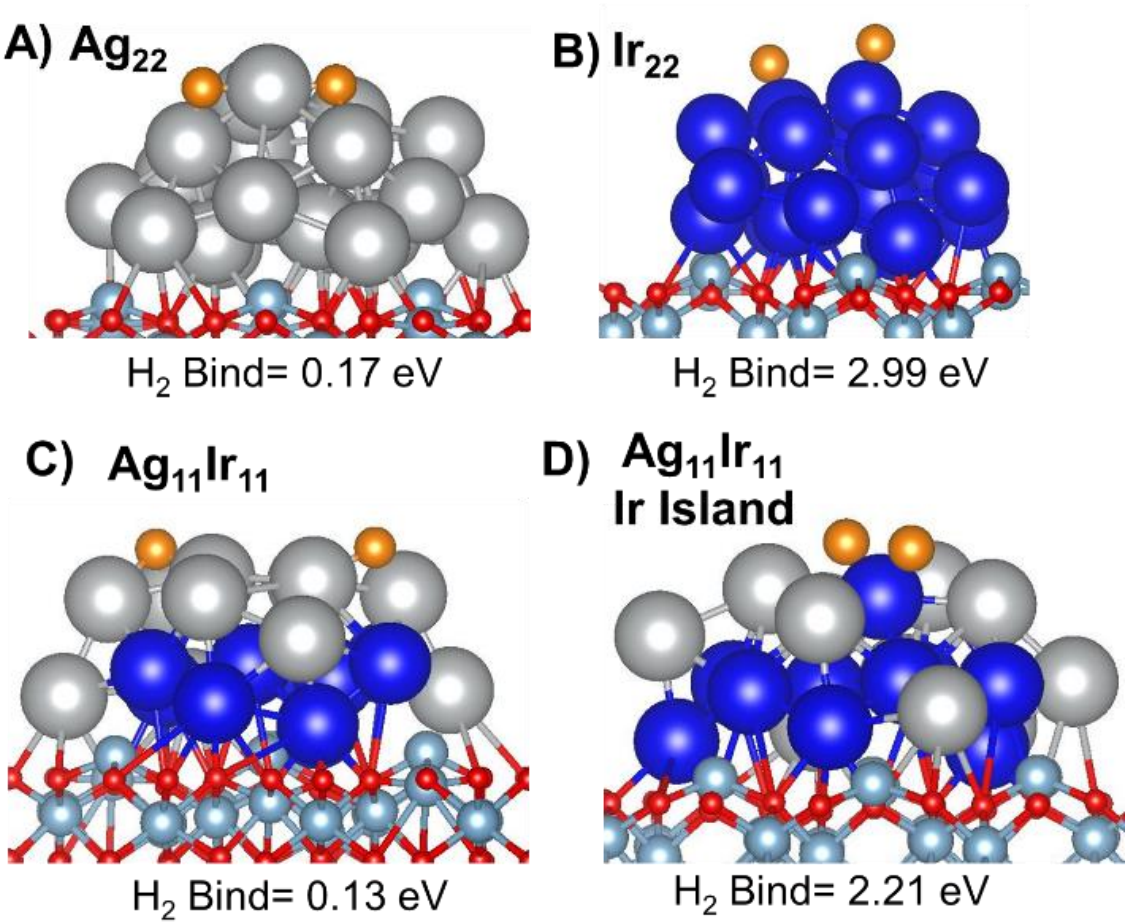

Figure 2.14: The H_2 binding energy for (A) Ag_{22}, (B) Ir_{22}, (C) $Ag_{11}Ir_{11}$ core shell particle, and (D) $Ag_{11}Ir_{11}$ where one Ir atom is moved to the shell. Ag is silver, Ir is blue, and adsorbed H is orange.

A more plausible consideration is for two H_2 molecules bound to a single Ir atom surrounded by Ag as in Figure 15. The first H_2 molecule dissociates and binds strongly with 2.21 eV as shown in Figure 15A, but a second H_2 molecule can also bind weakly at 0.84 eV, as indicated in Figure 15B. The H atoms are dissociatively adsorbed and are bridged between Ir and a neighboring Ag atom. The H/Ir >1 stoichiometry agrees with results of others for nanoparticles of Ir [39-40]. The calculated H_2 binding energy is large enough that the H/Ir stoichiometry could be as high as 4 in cases where single Ir atoms is surrounded by Ag. Because H is bridged between Ir and Ag, the binding energy is

significantly lower than when bound to Ir alone. A third H_2 molecule appears to have a negligible binding energy. This very low binding energy suggests that H spillover is unlikely to be a source of weakly bound H. The 0.84 eV binding energy found for the second H_2 molecule bound to the Ir atom is a plausible energy for a source of the weakly bound H, and the large H_2 uptake. Also, this corresponds to 4 H atoms binding to a single surface Ir atom, although this does require a structure where a single Ir atom is completely surrounded by Ag.

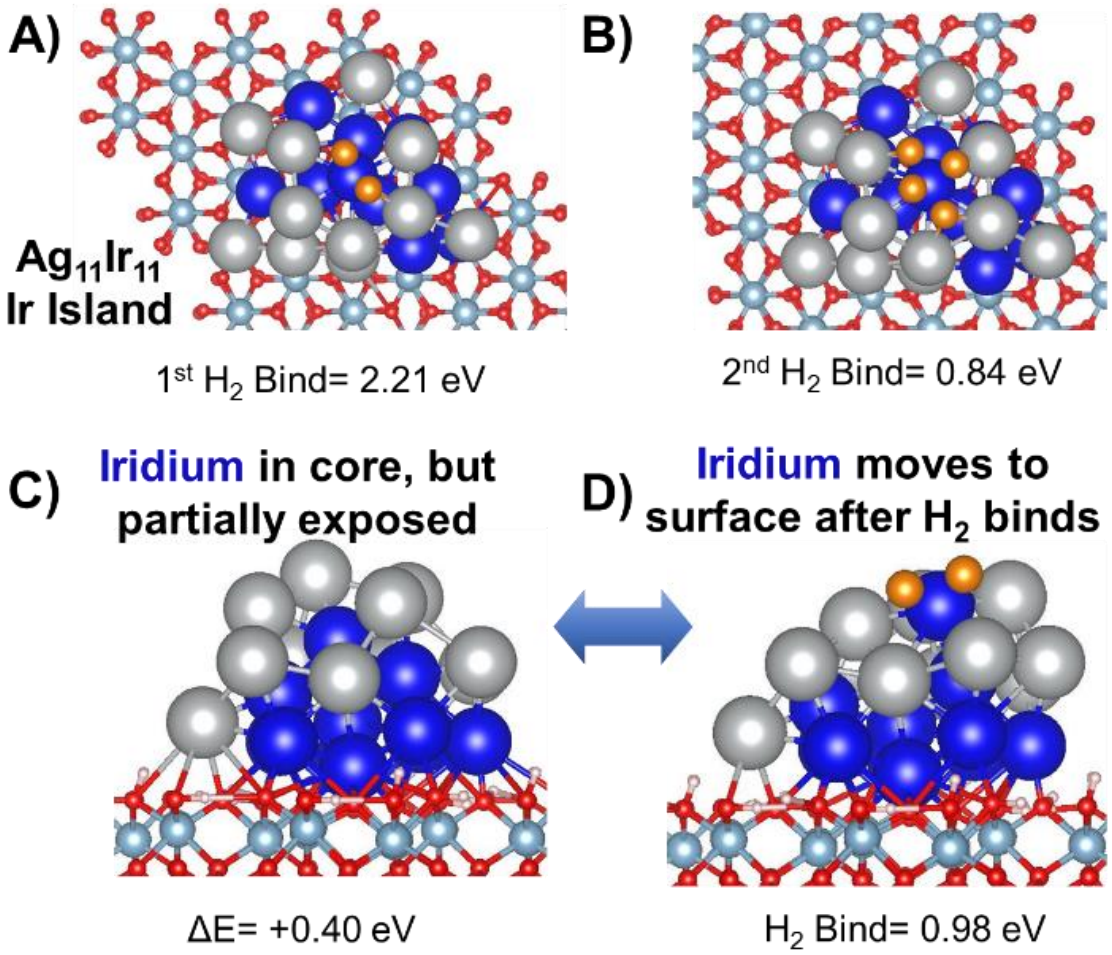

Figure 2.15: The H_2 binding energy of the (A) first and (B) second H_2 molecule on $Ag_{11}Ir_{11}$ where one Ir atom is moved to the shell. (C) The structure of an isomer of $Ag_{11}Ir_{11}$ on a gibbsite alumina support. (D) The structure of the $Ag_{11}Ir_{11}$ after a hydrogen molecule has bound to the partially exposed Ir atom.

A final possible source of the weakly bound H is that reconstruction of the core-shell particle may weaken the binding energy to Ir atoms that are partially exposed. In Figure 15C an Ir atom is "crowned" by 5 silver atoms in a $Ag_{11}Ir_{11}$ cluster supported on a Gibbsite alumina surface. When a H_2 molecule is brought near the Ir atom, the cluster reconstructs pulling the Ir atom out of the core. The net binding energy of the H_2 molecule is 0.98 eV, and this energy is lower due to the reconstruction energy of the cluster. When H_2 is removed from the exposed Ir, the Ir atom relaxes back into the core, returning to the original structure. The binding energy is also in the region expected for the weakly bound H_2 that desorbs in the TPD experiments.

After evaluating these different hypotheses for the weakly bound H_2 from the TPD experiments, two hypotheses have reasonable energetics. The first is that multiple H atoms bind to an Ir atom surrounded by Ag atoms. The first pair of H atoms binds quite strongly, and the second binds weakly as all 4 H atoms exist as bridged species between Ag and Ir. The second possibility is hydrogen-induced reconstruction of the core-shell particle, where Ir atoms that are close to the surface may bind to H_2 pulling an Ir atom out of the core, but due to the reconstruction energy these H atoms are weakly bound. We also observed that the Ir core does not activate the Ag shell and that H spillover from Ir to Ag is energetically unfavorable. Considering that the formation of isolated Ir atoms in the Ag shell is energetically realistic, the most likely explanation is that multiple H atoms are bound to a single Ir atom in a bridged Ir-Ag configuration resulting in both weakly bound H and an unusually high uptake with a 4:1 ratio of surface H to surface Ir. The fact that electroless deposition permits these structures to be formed with a high level of certainty has permitted this correlation of experiment with theory.

2.4.7 XPS results

XPS measurements were performed on the 0.24% Ag-1.0% Ir/θ,δ-Al_2O_3 and 0.24% Au-1.0% Ir/θ,δ-Al_2O_3 catalysts after in-situ annealing at 400°C in flowing Ar for 15 hours in the catalysis cell attached to the UHV sample chamber. The in-situ treatment was conducted to permit the study of electronic interactions of the bimetallic system, which was the temperature that gave maximum H_2 chemisorption values.

Figures 16 A and B show that after annealing in Ar both Ag 3d and Ir 4f peaks shift to lower Binding Energies (BE) by 0.5 eV and 0.8 eV, respectively, compared to their metallic states. This chemical shift is characteristic of intermetallic interactions indicating an electron transfer from Ag to Ir. Silver is an exception in photolectron spectroscopy where there is a shift to lower BE when it transfers e^- density to electronegative elements[41]. The DFT calculations in Figures 16 C and D show that the experimental chemical shifts are consistent with a Ag shell on an Ir core with the calculated Ag shift being -0.2 eV, and the Ir shift being -0.7 eV. The average charge on the Ag atoms is +0.04. However, when the Ag is in the core, the shift becomes -0.5 eV with the net charge on the Ag being +0.20. We have calculated these shifts on γ-Al_2O_3 because dry α-Al_2O_3 donates charge to supported metals, so α-Al_2O_3 is not an ideal model for analyzing XPS data. For the Ir shifts, there is only a small change in the calculations for surface Ir and core Ir; core Ir atoms have a shift of -0.7 eV and shell Ir atoms have a shift of -0.8 eV. While the energetic differences are small, this does not exclude the possibility that there are isolated Ir atoms surrounded by Ag in the surface layer (only one Ir atom out of a total of 11 Ir atoms) of the core-shell particle.

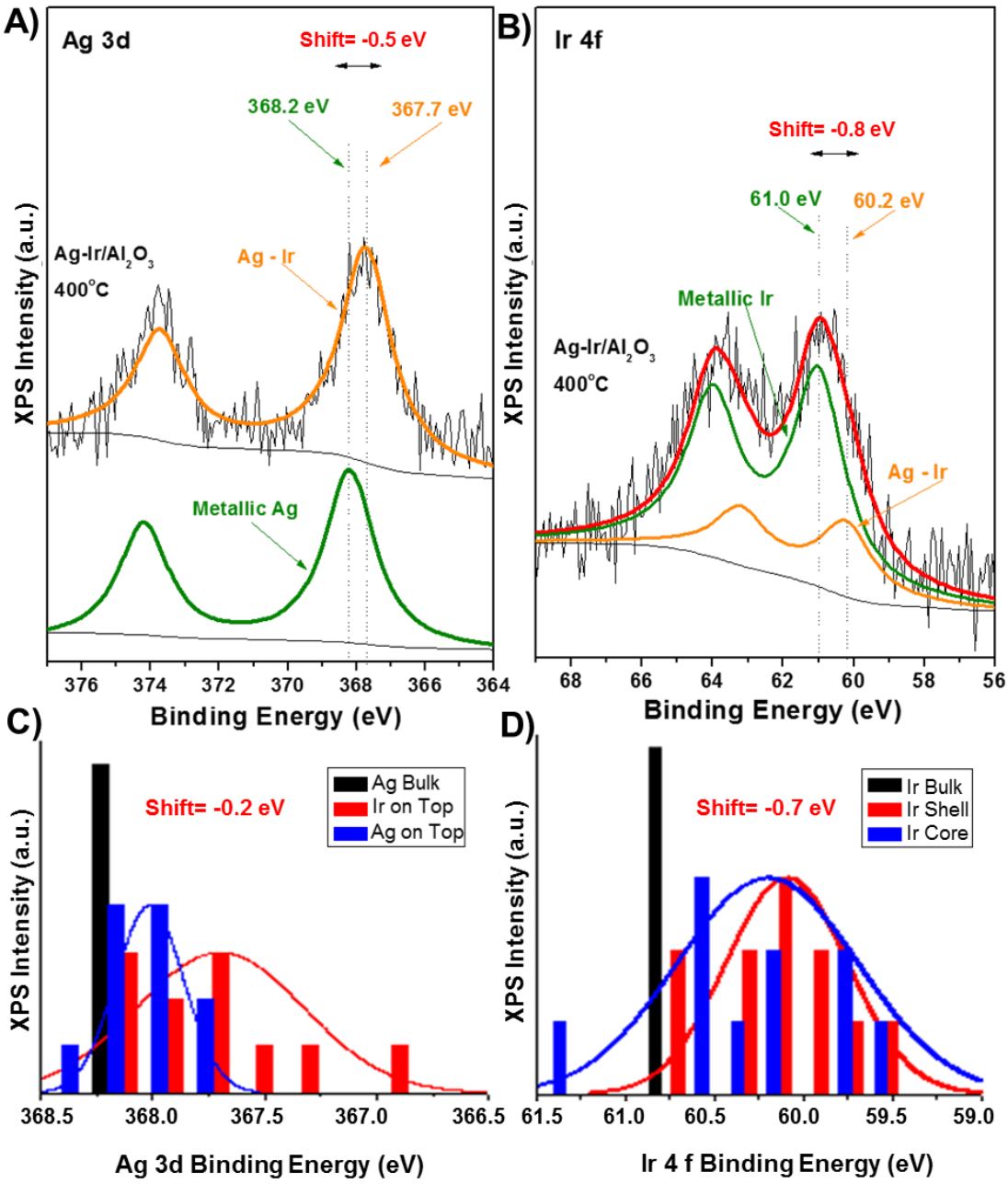

Figure 2.16: Electronic interaction of the 0.24% Ag-1.0% Ir/θ,δ-Al_2O_3 catalysts indicating core-shell nanoparticles after annealing at 400 °C from XPS measurements of the Ag 3d and Ir 4f core level peaks in (A) and (B). Panels (C) and (D) show DFT calculations of the chemical shifts of the corresponding XPS peaks on $Ag_{11}Ir_{11}$ on γ-Al_2O_3.

Both Ag and Au overlayers are expected to behave similarly [42] as we have shown in Figure 11. Han has used a combination of computational and STEM measurements to

study TiO_2-supported Ir surfaces covered with a layer of Au and found that Ir atoms can diffuse through the Au layer to form "isolated" Ir atoms in a Au surface matrix, very similar to what we postulate for the Ag-Ir system.[43] In fact, similar electronic effects were observed for the XPS data in Figure 17 for the Au-Ir catalysts after annealing in Ar at 400°C. The Au 4f peak shifts 0.4 eV to higher BE and Ir 4f shifts 0.8 eV to lower Binding Energy (BE), compared to the normal metallic states of Au and Ir . These chemical shifts again indicate intermetallic interaction between the metals and an electron transfer from Au to Ir.

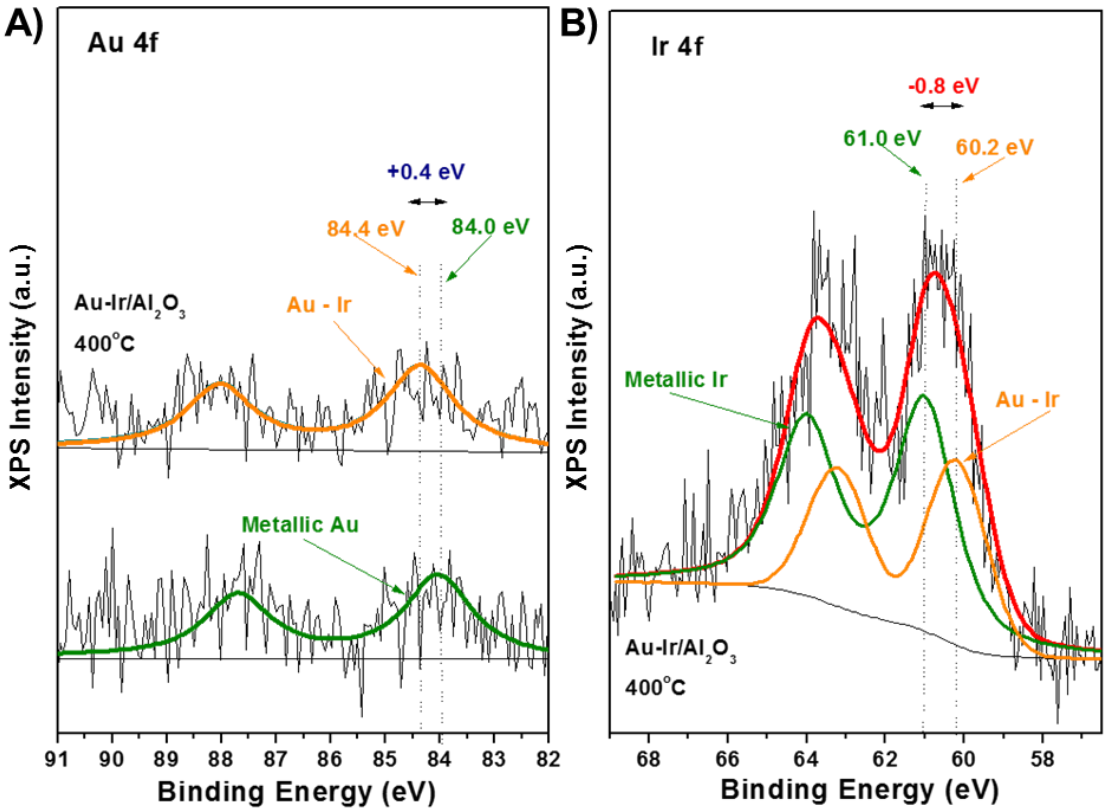

Figure 2.17: Electronic interaction of the the 0.24% Au-1.0% Ir/θ,δ-Al_2O_3 catalysts after annealing at 400 °C as demonstrated by XPS measurements of the Au 4f and Ir 4f core level peaks.

It has been reported that although Au alone cannot dissociate H_2, Au layers on top of Ir are reactive enough for H_2 dissociation[44-45]. The XPS results in this study provide evidence to support the chemisorption and TPD studies that H_2 chemisorption on both Ag-Ir and Au-Ir catalysts can be accounted for by strong electronic and structural differences between "as deposited" and "after annealing" bimetallic systems. The electronic interactions between Au and Ir and Ag and Ir are indicative of near-surface alloys that are able to either dissociate H_2 directly and or to provide an adsorption site for dissociatively adsorbed H [46]. The electronic transfer from Ag and Au towards Ir, together with surface segregation, can lead to enhanced catalytic activity of deposited noble metals and, possibly, Ir. Again, the key is the ability of electroless deposition to synthesize well-controlled and characterized bimetallic strucures.

2.5 Conclusions

The combination of SEA and ED permits formation of well-dispersed and well-controlled core-shell Ir@Ag nanoparticles on alumina supports. The Ag loading can be adjusted by changing reaction temperature, reducing agent, and reaction time for the ED bath. Higher Ag coverages occur at higher Ag weight loadings and coverages were determined using H_2 chemisorption following reduction at 200°C. After high-temperature annealing in flowing Ar (400, 600, and 800°C), H_2 chemisorption was unexpectedly high for the Ag-Ir/δ,θ-Al_2O_3 catalysts. TPD of H_2 confirmed the addition of large amounts of more weakly-bound H, compared to monometallic Ir. Computational studies credit the additional H_2 capacity to changes in the adsorption stoichiometry of H:Ir (from 1:1 to 4:1 at single atom Ir sites that are surrounded by Ag shell atoms. Consistent with the hypothesis of differential surface free energies (SFE) where the lower SFE component (Ag) is stabilized by deposition on the much higher SFE core metal (Ir), Ag was much more resistant to sintering. Somewhat surprising, the stability of the Ir core was also greatly enhanced. XRD, STEM, and XPS confirmed the higher stability and

formation of special Ir sites. We believe this is the first instance where rational catalyst formation has been used to prepare catalysts such as these that exhibit these properties and permit an extensive suite of characterization analyses that corroborate detailed computational analyses.

2.6 Acknowledgements

The authors gratefully acknowledge the National Science Foundation for funding through the Center for Rational Catalyst Synthesis, an Industry/University Cooperative Research Center [NSF Industry/University Collaborative Research Center grant IIP1464595]. ACR and SNK gratefully acknowledge funding from the U.S. Air Force Office of Scientific Research, grant FA9550-18-1-0511.

CHAPTER 3

IMPROVED SYNTHESIS OF MOVNBTE(SB)O_X M1-PHASE CATALYSTS FOR ODH OF ETHANE

3.1 Introduction

Increasing oil prices and environmental concerns are leading to urgent searching for alternative processes for production of light olefins that are more environmentally friendly from raw materials. More abundant and cheaper light alkanes from natural gas can be upgraded to light olefins that have more demands for, particularly for ethylene. Ethylene as a building block in chemical industry is produced by steam cracking and fluid catalytic cracking. The process of making ethylene from ethane thermal dehydrogenation and steam cracking consumes a large amount of energy annually which is not efficient from economic, industrial, and environmental point of view. The problems of traditional method such as high energy consumption, rapid coking and thermodynamics limitations are motivations to find a better approach for ethylene production, such as oxidative dehydrogenation (ODH) of ethane.[47-50]

ODH has drawn more attentions and interests due to several advantages such as changing the pathway from an extremally endothermic process, i.e. steam cracking or direct catalytic dehydrogenation, to an exothermic process, i.e. ODH, lowering the temperature that can save energy and operational costs, better performance by increasing the conversion and selectivity towards ethylene as a result of new chemical pathway, less coking problem due to introducing oxygen in the feed stream, and using one of the most abundant portion of natural gas, ethane, as a reactant.[51]

The selective oxidation of alkanes with low molecular weight like ethane need comprehensive study in catalysis. Production of C_2 oxygenated products from ethane using oxidant of H_2O_2 catalyzed by Zeolites containing Cu and Fe were investigated.[52] By utilizing simple evaporation method, Mo-V-Nb mixed oxides were prepared with

different composition and were studied for ODH reaction.[53] The improvement of catalysts has been evaluated and classified in two major groups: one is non-effective or slightly effective like doping, the other is effective like addition of another catalyst or coexistence of another phase (like M2 phase).[54-55] The most common catalyst used for oxidation reactions are metals, metal oxides or metal complexes immobilized in zeolites, silica, alumina or polymeric resins, and metal organic frameworks (MOFs) for selective and chiral oxidation catalysis.[56-57] It should be mentioned that because of low chemical reactivity of alkane, ODH of alkanes are challenging.[58]

In this work, we focus on improving catalyst properties such as activity and ethylene selectivity. Catalysts with different compositions, and calcination ramp rate were synthesized and evaluated. The catalyst behavior in different reaction conditions such as different temperature, with presence of dilution and without dilution was studied. Standard battery of tests used to characterize the catalysts, including XRD, XRF, Kr and N2 physisorption (BET), and SEM imaging. For evaluation, a setup of four parallel reactors were used with feed and product streams from each reactor evaluated by gas chromatography (GC).

3.2 Methods

3.2.1 Catalyst preparation

A catalyst with a nominal composition $Mo_1V_{0.29}Nb_{0.17}Te_{0.125}$ $Sb_{0.01}Ox$, is prepared in the following: In a 200ml beaker, 8.164 g of ammonium niobate (V) oxalate hydrate ($C_4H_4NNbO_9 \cdot xH_2O$) (Sigma Aldrich 99.99% trace metals basis), 0.147g of antimony (III) oxide (Sb_2O_3) (Alfa Aesar 99%) and 2.163 g of oxalic acid dihydrate ($HO_2CCO_2H.2H_2O$) (Alfa Aesar 99.5-102.5%) are mixed with 80 mL of DI water at room

temperature and stirred until fully solvated and a homogeneous solution (solution 1) is obtained. For mixing magnet stir bar with speed of 500 RPM has been used.

In another 200ml beaker, 17.815 g of Ammonium heptamolybdate tetrahydrate ($(NH_4)_6Mo_7O_{24}4H_2O$) (VWR Chemicals BDH 81.0-83.0% (MoO_3 basis)), 3.423 g of ammonium vanadium oxide (NH_4VO_3) (Alfa Aesar 99% min) and 2.896 g of telluric acid dihydrate ($H_2Te_4.2H_2O$) (Alfa Aesar 99+%) are dissolved in 100mL water at 70°C and a homogeneous solution (solution 2) is obtained. 2.5 mL of concentrated nitric acid is added to Solution 2. For mixing magnet stir bar with speed of 500 RPM has been used.

The resulting acidified solution is then combined with solution 1 and an orange-colored gel is formed. The catalyst is named USC2. Same procedure was used to prepare USC3($Mo_1V_{0.29}Nb_{0.17}Te_{0.150}Sb_{0.01}Ox$) except the amount of telluric acid dihydrate is 3.476 gr. For USC1($Mo_1V_{0.29}Nb_{0.17}Te_{0.200}Ox$) the amount of telluric acid dihydrate is 4.634 gr and there is no antimony (III) oxide.

For both USC 2, USC3, and USC1 after getting the solution, the water is removed from the gel on a rotavapor at 50°C and the absolute pressure remained at 50 mmHg until solid is obtained. This solid is further dried in an oven at 80°C overnight. Very dark green dried sample is collected and calcined for two hours in 250SCCM air from room temperature to 275°C with the ramp of 5°C/min. Then the gas is switched to 250SCCM nitrogen to reach 600°C with the ramp of 2°C/min. (Figure 1). The calcined material is ground with a mortar/pestle to powder which is then pressed (Model C, Carver, Inc., Wabash, IN, USA) in a 13mm ID stainless steel die (evacuable pellet press, PIKE

technologies, WI, USA) at 10,000 pounds, for a final pressure of ~50,000psi and crushed and sized to 20-25 or 40-60 mesh granules for reactor evaluation.

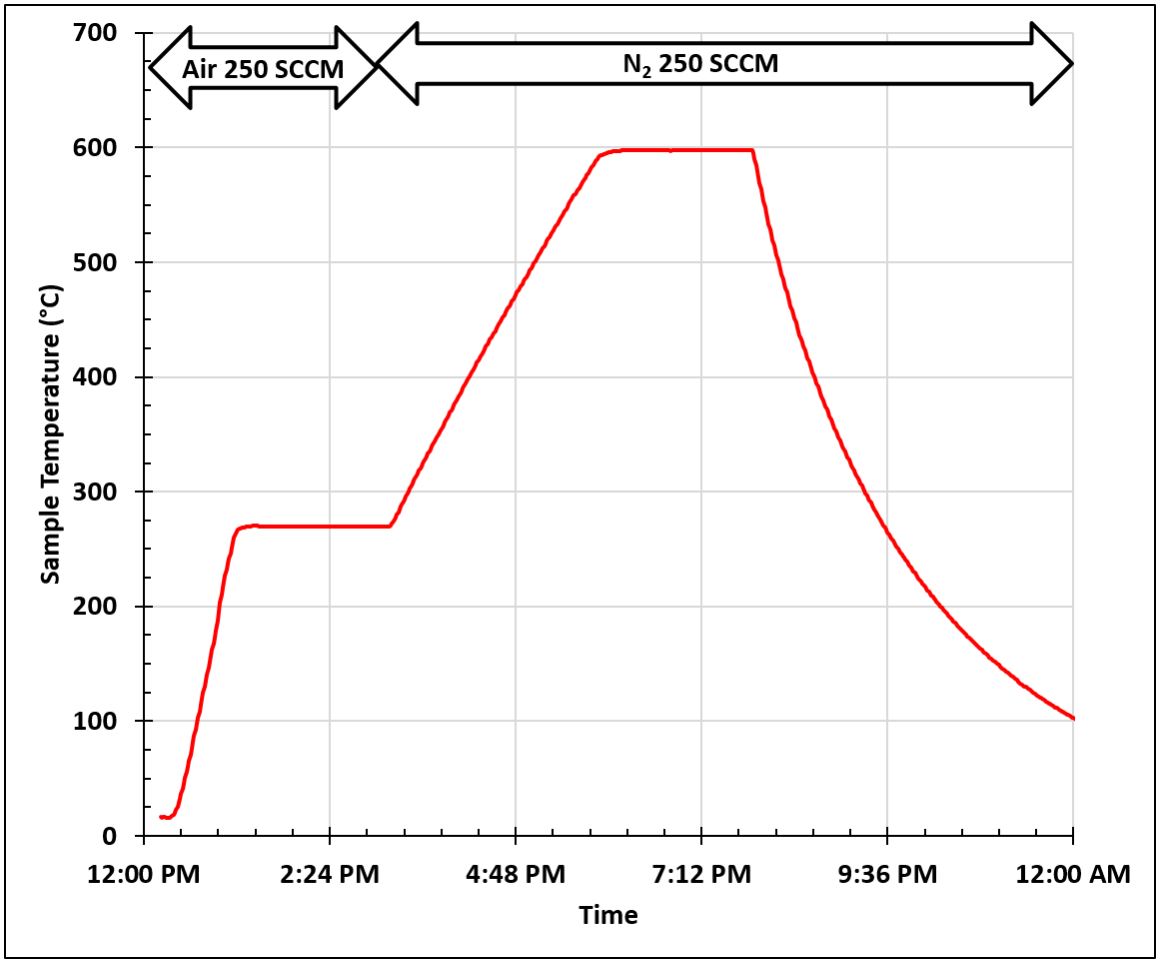

Figure 3.1: diagram of calcination furnace.

For the post treatment process, 8 gr of prepared catalyst was added to the solution of 3.2 gr oxalic acid dihydrate in 33.6 ml DI water. The mixture was heated at 75°C for 6hr while is it stirring with a stirring bar. The solution was brought to room temperature then filtered and washed to collect solid sample. The catalyst was dried in air at 80°C for 20hrs. The calcination occurred in a vertical furnace with the ramp rate of 5°C/min from room temperature to 600°C in the presence of 250SCCM N_2. The temperature was hold at 600°C for 2 hrs and then cooled to room temperature. The calcined material is ground

with a mortar/pestle to powder which is then pressed and crushed and sieved for further evaluation.

3.2.2 Reactor setup details

Reactor setup holds four parallel reactors. In order to control the flow of each inlet gas and therefore the feed composition, the gas feeds are connected to primary mass flow controllers (Brooks 5850e, Brooks Instrument, Hatfield, PA, USA), , and then they merge to an dead volume to allow for buffering of any flow fluctuations caused by MFC control chatter. After exiting the mixing chamber, the feed mixture goes to a secondary manifold, where four streams, controlled by MFCs feed each individual reactor. Excess flow is bled off by means of a back pressure regulator, at the end of this secondary reactor feed manifold. The temperature of each reactor is controlled by a heating mantle attached a temperature controller. Reaction pressure is controlled by a back pressure regulator (BPR) at the back of each reactor along with a pressure gauge. For operation at atmospheric pressure, a BPR bypass loop was used to prevent unknown pressures arising from varying BPR cracking pressure levels. The gas product streams, at atmospheric pressure, sampled downstream from each BPR is connected to a four-position VICI® (Valco Instruments Co. Inc., Houston, TX, USA) switching valve selects the reactor that is analyzed. A two-position VICI switching valve used to switch between injection and load mode for GC injection. Sampling occurs every 30 mins and the complete cycle time is 2hrs for 4 reactors. The diagram is shown in Figure 2.

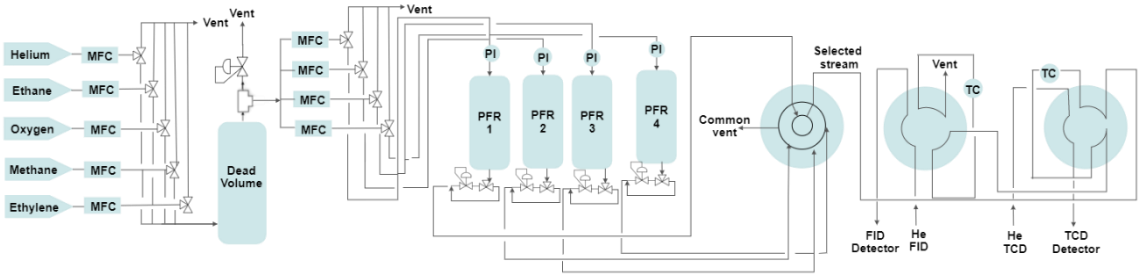

Figure 3.2: Four parallel reactors setup diagram.

The gas phase product is analyzed by gas chromatography (GC) (HP 5890 Series II) compact with HP PLOT-Q capillary column (30m, 0.320mm) for FID detector to quantify hydrocarbons and oxygenates and Carboxen 1010 PLOT (30m, 0.53mm) for TCD detector to quantify fixed gases. The temperature in GC is programmed to analyze and separately identify O_2, CO, CO_2, C_2H_4, C_2H_6 and acetic acid. The GC oven temperature stays at 50°C for 5 mins and undergo the rate of 25°C/min to reach the final temperature of 200°C and held at this level for 13 mins. The inlet and detector temperature are kept at 150°C for both detectors. The column head pressure is 9 and 2.5 psi for FID and TCD, respectively. Methane, an unreactive gas under reaction conditions studied, was used as a gas phase internal standard (5% by vol.) to correct for volumetric changes during reaction.

3.2.3 Catalyst characterization instruments

X-ray diffraction (XRD) patterns were collected using a Rigaku MiniFlex II equipped with a high sensitivity D/tex Ultra 250 1-D Si slit detector and a Cu-Kα radiation source (λ=1.5406 Å) operated at 30 mA and 15 kV. Scans were typically made over a 2θ range of 20˚- 80˚ at a scan rate of 2.0˚/min. In quantitative analysis with XRD, whole powder pattern fitting (WPPF) was used. This method is efficient because for this catalysts XRD pattern is complicated to be fitted by simple and single peaks. WPPF was

used to quantify M1 and M2 phases, using crystallographic data previously reported in literature for these phases, and assuming no contribution from simple metal oxides.

Sample surface areas were measured by N_2 and or Kr physisorption (ASAP 2020 Plus Micromeritics, Norcross, GA, USA) with Brunauer-Emmett-Teller (BET) used for data reduction. Upper P/P_0 determined by method of Rouquerol.[59] Good agreement of Kr and N_2 BET allowed for BHJ and another pore analysis to be accomplished through N_2 physisorption.

3.3 Results and discussion

3.3.1 Catalyst characterization

It was seen that the post treatment process increased SA and improved M1 to M2 ratio. The activity of the catalyst performance is summarized in Table 1. The Kr BET has been done to get the surface area and WPPF analysis was performed to get the M1 and M2 percentages.

Table 3.1: The reaction condition is 0.9 gr of fine powder pelletized and sieved with mesh 20-25. The gas flow is 12 SCCM. The pressure is 0 psig and the temperature is 325°C. feed composition is 15% C_2H_6, 10% O_2, 5% CH_4 and balance He. PT= post treated catalyst.

Catalyst	**Pellet SA (m^2/gr)**	**M1(%)**	**M2(%)**	**C_2H_6 Conv. (%)**	**C_2H_4 Sel. (%)**	**CO Sel. (%)**	**CO_2 Sel. (%)**	**HOAc Sel. (%)**	**rate C_2H_4 formation, (mmol/hr-gcat)**
USC 2 PT	12.1	97.6	2.4	23.45	93.97	2.22	2.63	1.18	1.11
USC 2	12.7	95.7	4.3	16.70	95.80	1.51	1.73	0.96	0.88
USC 3 PT	11.7	95.1	4.9	21.71	93.98	2.12	2.82	1.08	1.03
USC 3	12.0	93.6	6.4	13.09	96.01	1.55	1.61	0.83	0.69

Table 1 indicates that USC 2 PT shows higher activity while keeping almost the same C_2H_4 selectivity. It can be hypothesized that higher M1 to M2 ratio can result in higher rate of formation of C_2H_4. For better understanding of the effect of M1 to M2 ratio in the catalyst performance, a set of catalysts has been made, characterized, and evaluated. By changing the ramp rate of calcination step, catalyst with different M1 to M2 ratio had been synthesized. (Table 2)

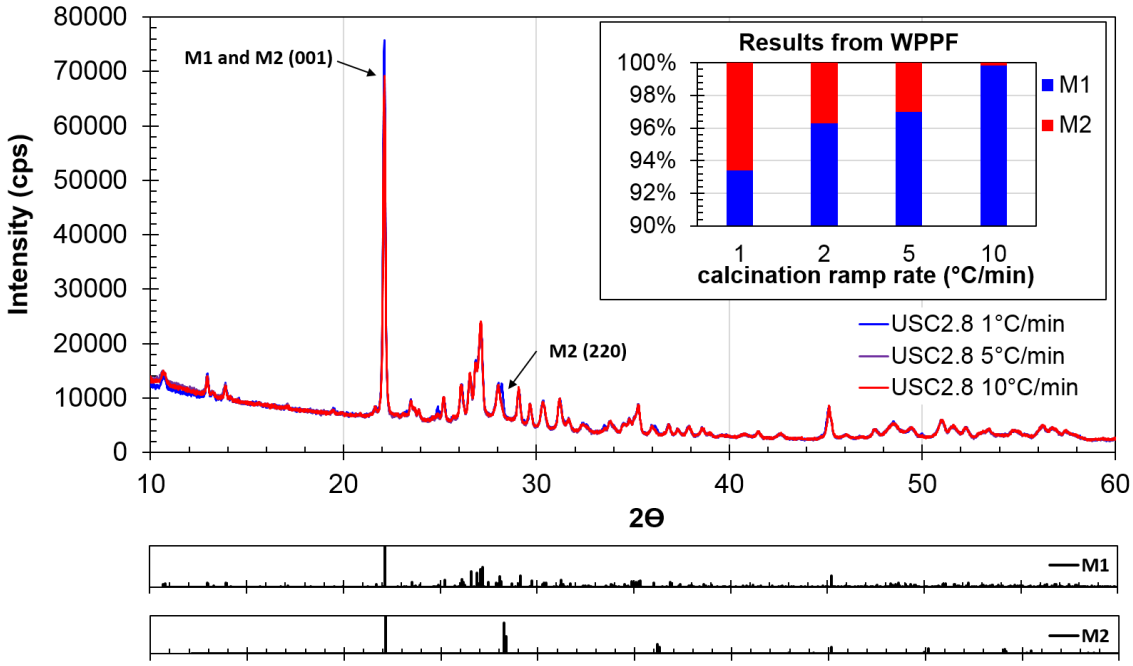

Figure 3.3: XRD pattern and WPPF analysis result.

It should be noted that the surface area is measured for the crushed pellet that sieved with 20-25 mesh. The XRD pattern for the samples is provided in Figure 3. The M1 and M2 phase have their most intense peak i.e. (001) along with other peaks in the same 2theta position.

As Kr BET shows the catalyst with 2°C/min has the optimum surface area among the catalysts with the same composition and different calcination ramp rates. Figure 4 shows the surface area and the amount of Kr absorbed.

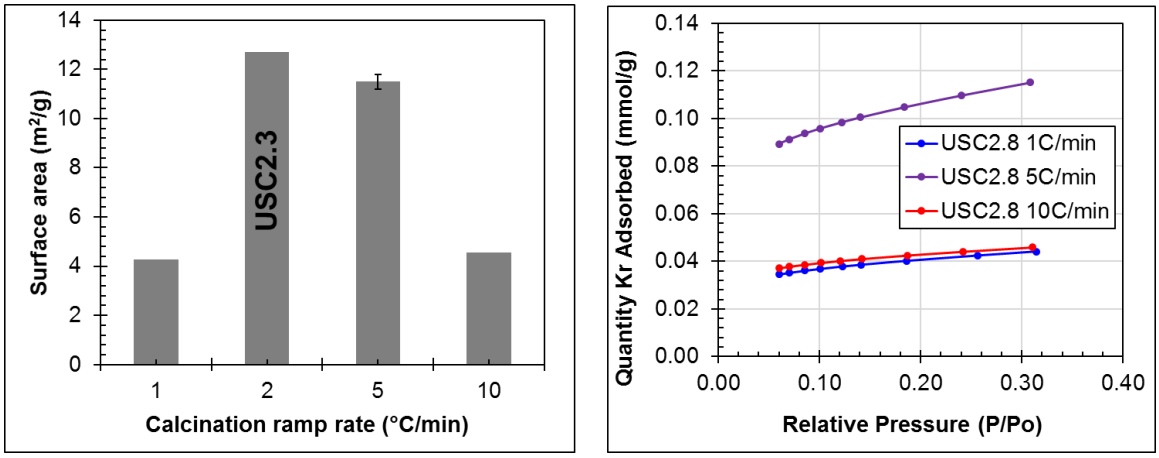

Figure 3.4: Surface area and Kr BET results.

The catalysts have been evaluated in two temperatures of 325 and 350°C to clarify the effect of M1 and M2 percentages and the surface area effect. The reaction data are summarized in Table 2.

Table 3.2: The reaction condition is 0.9 gr of fine powder pelletized and sieved with mesh 20-25. The gas flow is 12 SCCM. The pressure is 0 psig. feed composition is 15% C_2H_6, 10% O_2, 5% CH_4 and balance He. Surface area is by Kr BET, and M1/M2 analyzed by WPPF.

T (°C)	Catalyst	Ramp rate (°C/min)	Pellet SA (m^2/gr)	%M1	%M2	C_2H_6 Conv. (%)	C_2H_4 Sel. (%)	CO Sel. (%)	CO_2 Sel. (%)	HOAc Sel. (%)	rate C_2H_4 formation, (mmol/hr-gcat)	rate C_2H_4 formation, (mmol/hr-m^2cat)
325	USC2.8.1	1	4.3	93.4	6.6	16.63	95.97	1.45	1.73	0.85	0.88	0.204
	USC 2.7	2	12.7	95.7	4.3	16.70	95.80	1.51	1.73	0.96	0.88	0.068
	USC2.8.5	5	11.5	97.4	2.6	16.64	95.83	1.53	1.78	0.86	0.88	0.076
	USC2.8.10	10	4.6	99.8	0.2	15.54	96.07	1.53	1.53	0.87	0.81	0.176
350	USC2.8.1	1	4.3	93.4	6.6	34.20	95.07	2.33	1.95	0.65	1.80	0.418
	USC 2.7	2	12.7	95.7	4.3	34.21	95.01	2.33	1.94	0.72	1.81	0.142
	USC2.8.5	5	11.5	97.4	2.6	34.12	94.94	2.35	2.01	0.70	1.78	0.155
	USC2.8.10	10	4.6	99.8	0.2	32.41	94.92	2.49	1.97	0.62	1.69	0.367

For both Temperatures, the catalysts with different ramp rates show almost the same rate of C_2H_4 formation per amount of catalyst. On the other hand because of the difference between the surface area, the rate of formation per surface area of the catalyst is higher for calcination ramp rate of 1 and 10 °C/min, and it has the same rate of formation for 2 and 5 °C/min. To investigate the catalyst property that causes this difference between surface area yet showing the same rate of C_2H_4 formation per gr catalyst, the SEM images were provided. (Figure 5)

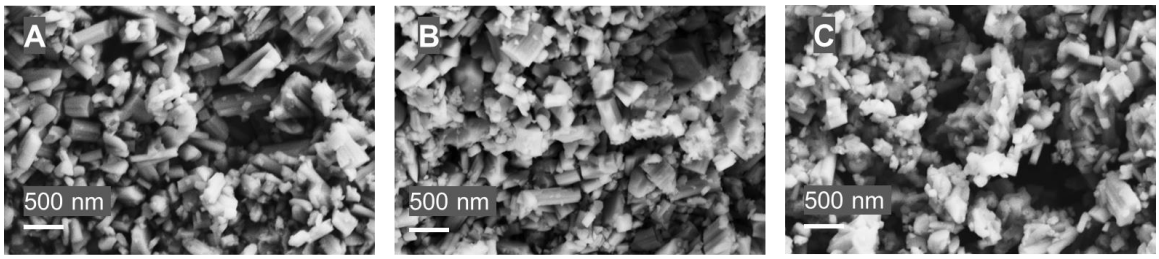

Figure 3.5: SEM images of (A) post-treated USC 2 ; (B) USC 2 with 2°C/min ramp rate; (C) USC 2 with 10°C/min ramp rate.

Figure 5 B shows the SEM image of catalyst with the ramp rate of 2°C/min. The needles are short with average needle length of 219nm. Figure 5 C indicates the image for the same catalyst with the ramp rate of 10°C/min. The needles have the average length of 92 nm and in comparison with 2°C/min sample shows shorter needle length and more folded needles. Sintering more needles together explains the lower BET surface area , and keeping almost the same area for the needle ends (the supposedly active surface) explains the same rate of C_2H_4 formation for 2°C/min and 10°C/min samples. As a conclusion calcination ramp rate (1 to 10°C/min) has no significant effect on catalyst performance despite change in surface area. The calcination ramp rate affects BET SA with maximum value at 2 and 5°C/min.

Figure 5A shows post treated USC2 which has similar average length as USC2 (230 nm). It is worth mentioning that both samples have 2°C/min calcination ramp rate. It can be concluded that the ramp rate effect the needle shape not the post treatment process. The area for (001) plane which reported to be active surface for ODH[60] are the same for all 3 samples shown in the Figure 5.

Figure 6 shows the mmol of product vs conversion for samples with different calcination ramp rates of 2, 5, 10°C/min. The higher conversion is at 350°C and low conversion is at 325°C. All the products have similar values, therefore, the difference in M1/M2 ratio has no effect on catalyst performance.

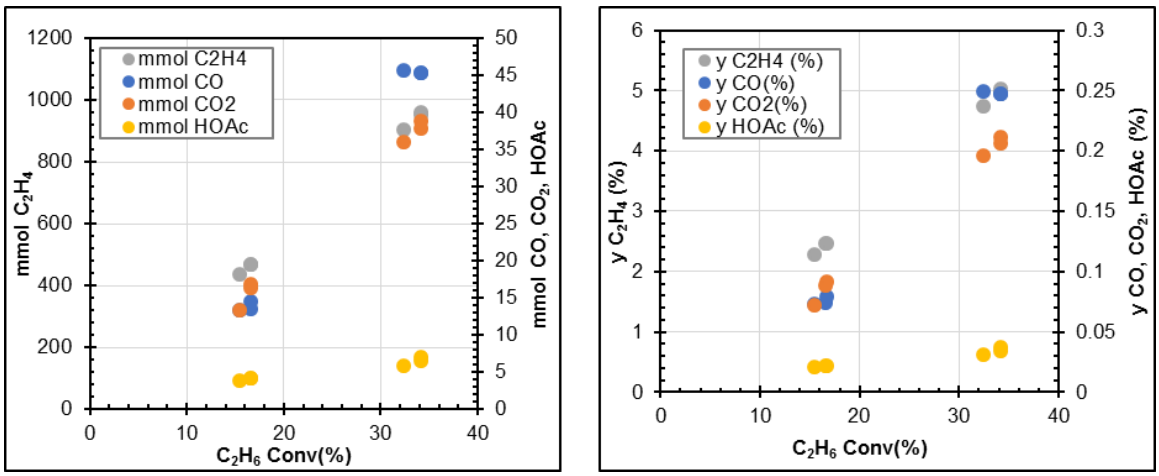

Figure 3.6: Amount of products vs C_2H_6 conversion.

3.3.2 Effect of different Te amount and of removing Te

The difference between USC1, USC2, and USC3 are the amount of telluric acid dihydrate in the solution, therefore, the nominal composition and different M1/M2 ratio. In addition, Figure 6 led to no effect of M1/M2 ratio in the catalyst performance. To investigate the mysterious effect of post treatment process and the difference in activity

between USC1, USC2, and USC3, XRF performed and summarized in the Table 5. The XRF data show surprising result.

The XRF results indicate USC2 dried (the sample before calcination) has higher amount of Mo, V, Sb and lower amount of Nb. USC2.7PT has lower amount of V and Te. As the post treated catalysts show higher activity, it can be concluded that although the overall amount of V decreased, the V with specific oxidation state (V^{+5}, that plays an important role in the RDS (rate determining step)[61] has to be increased. It is the same for USC 3.2 and USC3.2 PT. USC2 synthesized with different ramp rates show the same composition which explains the same activity, despite different M1/M2 ratio. The conversion and yield are plotted in Figure 7 For all the catalysts listed in Table 3, except the USC2 dried (the sample before calcination). It shows the catalyst with lower amount of V is more active. Figure 7 suggests only specific V (probably V^{+5}) is important but not the amount of V. Despite having the same initial V ratio for all the catalysts, increasing the active V increases the conversion and yield more than twice.

In another set of catalyst tellurium, one of the 5 metals in the mixed oxide catalyst, was removed. ($Mo_1V_{0.29}Nb_{0.17}Sb_{0.01}$). The catalyst was calcined at the ramp rate of 2°C/min. As a result of this removal the structure was not preserved the same (Figure 8). Existing work at Union Carbide showed MoVNb ability to run ODH, however, residence time is about 10 times of current residence time, and the SA is unknown.[62]

Table 3.3: XRF results in atomic ratio and normalized to Mo.

Name	Mo	V	Nb	Te	Sb	+/-Mo	+/-V	+/-Nb	+/-Te	+/-Sb
USC1.1	1.000	0.346	0.197	0.143	0.001	0.019	0.016	0.005	0.006	0.001
USC2.11dried	1.000	0.317	0.173	0.088	0.010	0.008	0.014	0.005	0.008	0.002
USC2.5	1.000	0.298	0.194	0.074	0.006	0.007	0.015	0.004	0.005	0.001
USC2.8.1	1.000	0.295	0.196	0.072	0.008	0.010	0.008	0.006	0.006	0.002
USC2.8.5	1.000	0.295	0.193	0.073	0.007	0.016	0.010	0.007	0.004	0.001
USC2.8.10	1.000	0.296	0.194	0.074	0.008	0.014	0.013	0.006	0.007	0.003
USC2.5PT	1.000	0.254	0.203	0.064	0.008	0.002	0.008	0.002	0.004	0.001
USC3.2	1.000	0.314	0.193	0.078	0.007	0.005	0.005	0.008	0.007	0.003
USC3.2PT	1.000	0.276	0.205	0.072	0.007	0.014	0.008	0.005	0.005	0.000

.

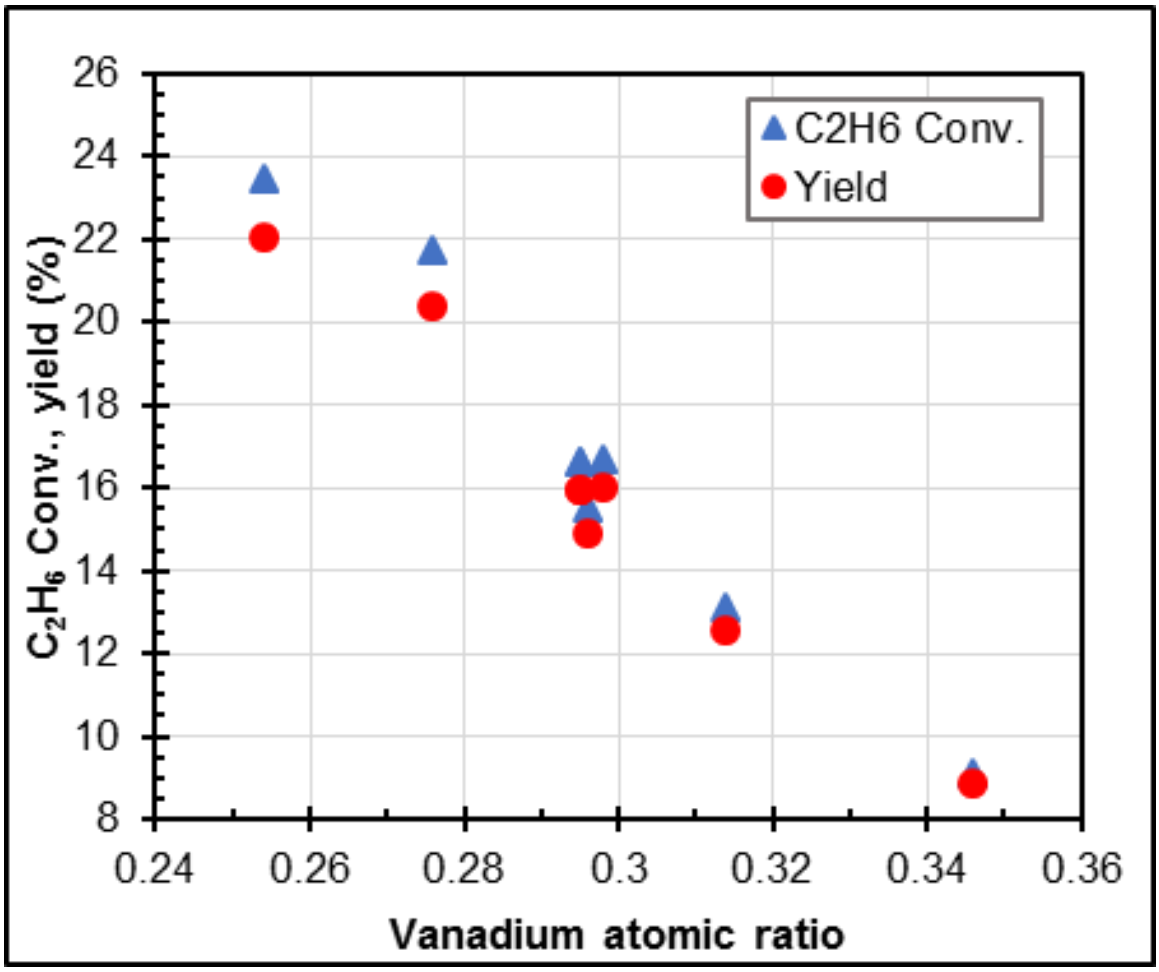

Figure 3.7: C_2H_6 conversion and yield vs. vanadium atomic ratio. The reaction condition is 0.9 gr of fine powder pelletized and sieved with mesh 20-25. The gas flow is 12 SCCM. The pressure is 0 psig and Temperature is 325°C. feed composition is 15% C_2H_6, 10% O_2, 5% CH_4 and balance He.

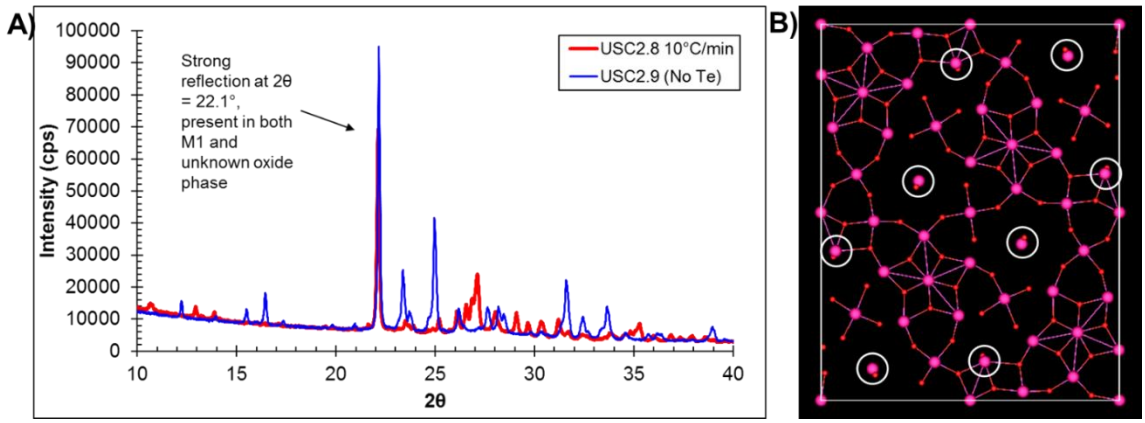

Figure 3.8: A) XRD pattern of catalyst with and without Te. B) Looking down [001] plane of M1 phase. The circles show the Te atom locations in the structure.

The evaluation was done for the catalyst without Te. Removal of Te gives new mixed oxide phase which is not active for ODH. Table 4 shows the very low performance of the catalyst without Te.

Table 3.4: The reaction condition is 0.9 gr of fine powder pelletized and sieved with mesh 20-25. The gas flow is 12 SCCM. The pressure is 0 psig. feed composition is 15% C_2H_6, 10% O_2, 5% CH_4 and balance He.

T (°C)	C_2H_6 Conv. (%)	C_2H_4 Sel. (%)	CO Sel. (%)	CO_2 Sel. (%)	HOAc Sel. (%)	rate C_2H_4 formation, (mmol/hr-gcat)
325	0.15	62.75	19.03	18.22	0.00	0.005
350	0.33	63.97	19.88	16.15	0.00	0.012

3.3.3 Mass transfer limitation

In another test the mass transfer limitation was studied with different mesh size and different amount of SiC as a dilution. The total bed height was held at the same level of 6.4 inch for all conditions. The surface areas are summarized in Table 6.

Table 3.5: Kr and N_2 BET.

Sample	Kr BET (m^2/g)	N_2 BET (m^2/g)
USC2.4 PT 20-25mesh	12.1	12.7
USC 2.4 PT 40-60mesh	14.2	15.0

Table 3.6: The catalyst activity summary for different mesh size and dilution. The pressure is 0 psig and the temperature is 350°C. feed composition is 15% C_2H_6, 10% O_2, 5% CH_4 and balance He.

Catalyst	Reactor	Flow rate (SCCM)	C_2H_6 Conv. (%)	C_2H_4 Sel. (%)	CO Sel. (%)	CO_2 Sel. (%)	HOAc Sel. (%)	rate C_2H_4 formation, (mmol/hr-gcat)	rate C_2H_4 formation, (mmol/hr-m^2 cat
USC 2.4-PT 0.9g 20-25 mesh	PFR1	12	42.05	95.19	2.46	1.52	0.84	2.12	0.16
		24	25.84	96.36	1.75	1.18	0.71	2.75	0.20
		36	19.13	96.70	1.58	1.09	0.63	2.94	0.22
USC 2.4-PT 0.9g 40-60 mesh	PFR3	12	46.37	94.96	2.57	1.57	0.90	2.33	0.15
		24	29.64	96.13	1.89	1.19	0.79	3.15	0.20
		36	21.88	96.64	1.62	1.06	0.68	3.36	0.21
USC 2.4-PT 2.7g 20-25 mesh	PFR4	36	45.75	94.79	2.56	1.77	0.88	2.29	0.17
		72	28.84	96.04	1.86	1.34	0.76	3.06	0.23
		108	21.54	96.54	1.59	1.18	0.70	3.30	0.25

The selectivity vs conversion for the catalysts listed in Table 6 shows in Figure 9. The mechanism is not changing while adding different amount of dilution or using different mesh sizes for both 350°C and 325°C. For both Temperatures, the slope is less than 0.1 which shows the independency of selectivity to extent of conversion. It can be concluded from combining both temperatures that the C_2H_4 selectivity decreased only 2% (from 97% to 95%) while the conversion increased significantly from 8% to 47%. These plots show ODH can be operated at high conversion without losing C_2H_4 selectivity. There is very small amount of CO_x products as a result of consecutive combustion. The intercept is about 98% indicates only 2% belongs to parallel combustion.

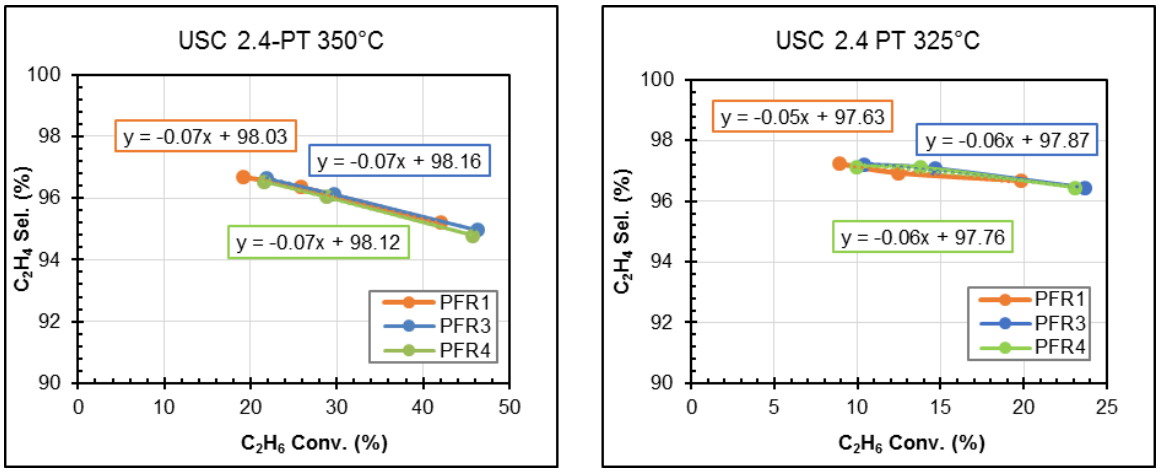

Figure 3.9: Conversion vs selectivity for USC 2.4 PT at 325 and 350°C

Comparing PFR1 and 3 in Table 6 gives higher conversion for smaller particles 40-60. It can be concluded that with the same amount of catalyst, 40-60 will give more active site, but it is noted that SA of 14.2 m^2/g for 40-60mesh is higher than 12.1 m^2/g for 20-25. The rate of C_2H_4 formation needs to be normalized for surface area. The results in the last column on the table shows that the rate of formation is not limited by catalyst conditions (mesh size or dilution). There is no intra particle mass transfer limitation. The

sample BET adsorption/desorption isotherm and BJH vs pore size can be shown in Figure 10.

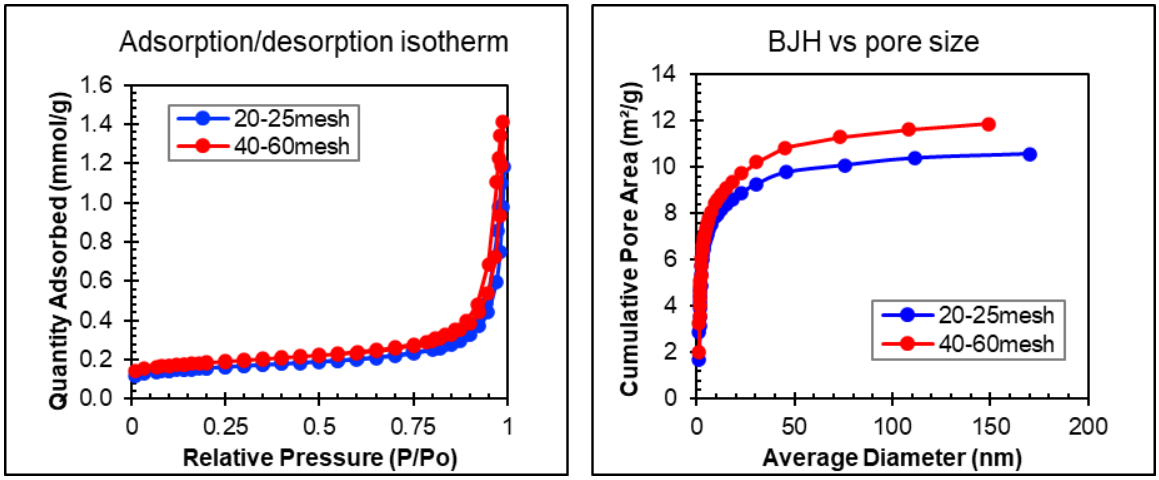

Figure 3.10: Adsorption/desorption isotherm and BJH vs pore size.

In Table 6 comparing PFR4 and 1 shows higher activity for PFR4 that can be due to slightly higher T because of lower amount of dilution. To prove this hypothesis, the catalyst performance without dilution was studied (Table 7). The flow rate for PFR4 is three times of PFR1 and PFR3 to keep the residence time the same.

Table 6 and 7 show the comparison between the catalyst with and without dilution. The catalysts without dilution show slightly higher rate of C_2H_4 formation. It can be concluded that this difference between rates of formation is due to higher temperature in the catalyst bed. Although the four parallel reactors operate similar, it is worth mentioning that the catalysts were evaluated in the same PFR to avoid having any other variables but dilution.

Table 3.7: Catalyst activity for reaction without dilution. The pressure is 0 psig and the temperature is 350°C. Feed composition is 15% C_2H_6, 10% O_2, 5% CH_4 and balance He.

Catalyst	Reactor	Flow rate (SCCM)	C_2H_6 Conv. (%)	C_2H_4 Selec. (%)	CO Selec. (%)	CO_2 Selec. (%)	HOAc Selec. (%)	rate C_2H_4 formation, (mmol/hr-gcat)	rate C_2H_4 formation, (mmol/hr-m^2 cat)
USC 2.4-PT 0.9g 20-25 mesh	PFR1	12	47.77	94.57	2.72	1.64	1.07	2.42	0.18
	PFR1	24	29.76	95.99	1.88	1.22	0.91	3.14	0.23
	PFR1	36	22.13	96.55	1.60	1.04	0.82	3.62	0.27
USC 2.4-PT 0.9g 40-60 mesh	PFR3	12	47.79	93.84	2.69	1.60	1.87	2.41	0.15
	PFR3	24	30.52	95.13	1.87	1.21	1.79	3.20	0.20
	PFR3	36	22.36	96.64	1.56	1.07	0.73	3.66	0.23
USC 2.4-PT 2.7g 20-25 mesh	PFR4	36	51.66	94.46	2.86	1.68	1.00	2.61	0.19
	PFR4	72	32.88	95.95	1.97	1.23	0.85	3.46	0.26
	PFR4	108	24.86	96.53	1.65	1.05	0.77	4.05	0.30

3.4 Conclusions

The slurry method shows a promising and effective way to synthesize a selective and active MoVNbTe(Sb)Ox M1-phase catalysts for ODH of ethane. Different catalysts were prepared to study the M1/M2 ratio effect on catalyst performance. The change in calcination ramp rate resulted in different M1 and M2 phase percentages. XRF results and SEM images prove the similarity in activity and the selectivity and the difference in surface area.

Post treatment process changes both M1/M2 ratio and the composition. The post treated catalyst shows significantly higher activity due to removing the vanadium. As it was concluded that catalysts with different M1/M2 ratio synthesized from different calcination ramp rate have the same performance. Thus, the effect of post treatment is on the change of vanadium amount (V^{+5}).

The main difference between USC 1, 2 and 3 is their composition not M1/ M2 ratio. Although the M1/M2 ratio are different between USC1, USC2, and USC3, but the main reason for different catalyst performance is the amount of vanadium in the catalyst after calcination. It should be noted that all the catalysts started with the same amount of V and different amount of Te, but after calcination they have different amount of V. The difference comes from having different amount of tellurium in the main preparation solution. As the calcined catalyst with less vanadium and is more active, it is proposed that the active vanadium (V^{+5}) is more for the total lower V ratio. It was studied that removing Te from the mixed oxide catalyst almost deactivate the catalyst for ODH of ethane. It is hypothesized tellurium plays an important role in the active plane of (001) and its structure.

CHAPTER 4

KINETIC EVALUATION OF ETHANE ODH OVER MOVNBTE(SB)O_X M1-PHASE CATALYSTS

4.1 Introduction

To increase active sites of MoVTeNb oxides, the surface structure of the M1 phase plays an important role. In this context, the (001) surface facet is believed to be the most active site, and it can be increased by hydrothermal synthesis to grow rod-shaped crystals.[63-64]

The preparation method of Te-containing MoVNb mixed oxide is important in ethane ODH activity.[65] The catalyst synthesized using hydrothermal method showed ethane conversion and ethylene selectivity of higher than 80% at 340-400°C. The high selectivity was related to a $Te_2M_{20}O_{57}$ (M = Mo, V, Nb) crystalline phase, and elimination of MoO_2 as unselective phase.[66] Olefins are produced selectively by formation of orthorhombic $(SbO)_2M_{20}O_{56}$ or $Te_2M_{20}O_{57}$ (M = V or Mo, with/without Nb) phases at 600°C.[67] To answer the challenging question whether Te, Sb or Nb has an importance in catalysis or are simply structural promotors stabilizing the M1 phase, pure orthorhombic MoO_3VO_x catalysts[68] show excellent performance and high productivity at low temperature, while the performance slightly improved for MoVTeNbO.[69] In addition, catalysts with trigonal phase and amorphous structure show less activity, and the lowest activity is attributed to tetragonal MoO_3VO_x catalysts. Furthermore, orthorhombic phases provide higher activity due to the pentagonal structural units, heptagonal channels which facilitates ethane adsorption, and distorted octahedra which is required for lattice oxygen species activation.[68] Therefore, Te, Sb, or Nb work as structural promoters rather than as active sites in ODH of ethane. However, density functional theory (DFT) predicts that C-H activation is associate to V-modified Te=O sites.[70-71]

The V^{5+} species have linear correlation with the activity of phase-pure M1 catalysts.[10,11] The oxygen plasma treatment of the M1 phase of MoVNb- TeOx was used to prove increasing ethane ODH activity with transformation of V^{4+} to V^{5+}.[74]

The Langmuir–Hinshelwood–Hougen–Watson (LHHW) mechanism was proposed rather than Mars-van Krevelen mechanisms for ethane ODH over MoVNbTeO catalysts.[75] Ethylene formation significantly depends on ethane partial pressure while independent of oxidant pressure.[75] The oxygen content estimate of metal oxides in the presence of molecular oxygen obtained from modeling indicates only surface lattice oxygen participates in ODH of ethane.[76-77] Reduced metal oxides can be effectively regenerated in a fluidized bed reactor.[78-80]

Kinetics of ODH of ethane over MoVTeNbO catalysts explained by LHHW model suggest inhibiting effect of H_2O adsorption on reactivity.[75] Modeling results of a wall cooled packed-bed reactor to investigate the effect of coolant temperature on ethylene yield suggest a weak effect of oxygen partial pressure, a negative impact of strong water adsorption on active sites, and a significant importance of inlet ethane partial pressure.[76] Power law kinetic models applied to simulate ethane ODH over MoVTeNbO catalysts also predicted a reaction order of 1.46 for ethane and 0.17-0.43 for oxygen. In addition, this study also showed that CO_2 was mainly formed from ethane, while CO was formed from both ethane and ethylene. Finally, they found a lower activation energy barrier for ODH of ethane (119 kJ/mol) than for ethane oxidation to CO (242 kJ/mol).[81] In another study, Che-Galicia et al. used Eley-Rideal (ER) model to describe reaction mechanism of ODH of ethane over MoVTeNbO catalysts.[82] Although both LHHW and ER mechanisms were reasonably in agreement with experimental data, only the ER

mechanism correctly predicted the effect of ethane partial pressure on reactor hot spots at 452˚C and increased rates of CO_x formation. In addition, the Eley-Ridel-redox mechanism was also proposed for the reaction network of ODH of ethane over MoV catalyst by Rahman et al..[83]

Donaubauer et al. proposed an intrinsic kinetic model for different temperature and pressure and feed ratios. In addition, the presence of C_2H_4 in the reaction mixture was studied. They found oxidation to CO dominates and the net rate of ethylene production was influenced by the consumption of ethylene due to inhibition. C_2H_4 presence showed no significant effect on either secondary H_2 abstraction to AcO* formation or lattice hydroxyl group oxidation. As expected, the C_2H_4 adsorption inhibits its formation.[84]

In this work the active and selective MoVNbTe(Sb)Ox M1-phase catalyst was synthesized using Slurry method. Catalyst pretreatment with co feed of ethylene were performed and the catalyst stability was proved. The complete set of kinetic study was done including reactant reaction orders (C_2H_6, O_2), products reaction orders (C_2H_4, CO_2, and H_2O). Three pressures of 0, 60, and 120psig and three temperatures of 275, 310, and 350°C were used. The activation energies of ethane consumption and products formation was calculated. Catalyst characterization before and after reaction was performed. It should be noted that for the entire kinetic study the same catalyst was used. The stability test after each set of evaluation confirms the same activity at the standard reaction condition. No deactivation was seen during this kinetics study.

4.2 Methods

4.2.1 Catalyst preparation, catalyst characterization instruments, and reactor setup

The catalyst preparation and characterization were discussed in more details in chapter 2 of this dissertation. For this, a catalyst with a nominal composition $Mo_1V_{0.29}Nb_{0.17}Te_{0.125}$ $Sb_{0.01}Ox$, is prepared and named USC2. The post treatment process was performed (USC2 PT) and the calcined material is ground with a mortar/pestle to powder which is then pressed (Model C, Carver, Inc., Wabash, IN, USA) in a 13mm ID stainless steel die (evacuable pellet press, PIKE technologies, WI, USA) at 10,000 pounds, for a final pressure of ~50,000psi and crushed and sized to 40-60 mesh granules for reactor evaluation.

For catalyst characterization instruments the same XRD, XRF, and BET instruments described in chapter 2 were used. The reactor setup is the same as chapter 2 of this dissertation.

4.2.2 Catalyst pretreatment before the kinetics study

The catalyst stability is essential in the kinetics study. The intention is using the same catalyst for the complete set of kinetics study. Regarding the effect of products in catalyst stability, the effect of C_2H_4 on the catalyst is a challenging question. To answer this question, different amount of C_2H_4 was added to the stream and the catalyst activity was investigated.

Table 4.1: Reaction condition: Catalyst = USC2.4 PT (PT is post treated catalyst), catalyst size = fine powder pelletized and sieved with 40-60 mesh size, P = Atmospheric pressure (Bypass BPRs), Flow rate = 12 SCCM, T = 350 ˚C, Feed composition = 15% C_2H_6, 10% O_2, 5% CH_4, different amount of C_2H_4, and balance helium.

Feed C_2H_4 (%)	**C_2H_6 Conv. (%)**	**Conv. lost compared to no feed C_2H_4 (%)**
0	47.79	0.0
5	40.23	15.8
10	35.17	26.4
15	33.02	30.9
25	25.49	46.7

Table 1 shows more deactivation when higher amount of ethylene is added to the feed. The same trend of losing activity was shown for both post treated catalyst and catalyst without post treatment (Table 2).

Table 4.2: Reaction condition: Catalyst size = fine powder pelletized and sieved with 40-60 mesh size, P = Atmospheric pressure (Bypass BPRs), Flow rate = 12 SCCM, T = 350 ˚C, Feed composition = 15% C_2H_6, 10% O_2, 5% CH_4, different amount of C_2H_4, and balance helium, (PT) – post treatment.

Catalyst	**Feed C_2H_4 (%)**	**C_2H_6 Conv. (%)**	**Conv. lost compare to no feed C_2H_4 (%)**
USC 2.4	0	38.96	0.0
USC 2.4	25	18.07	53.6
USC 2.4 PT	0	47.22	0.0
USC 2.4 PT	25	24.71	47.7

The reactors were loaded with fresh catalyst and the activity calculated for the feed of 15% C_2H_6. Then the catalysts were exposed to feed stream with co-feed of 15% C_2H_4 at 350°C. After removing C_2H_4, the activity was measured for different temperatures. It is concluded that the decrease in the activity was also observed in all three temperatures. Surprisingly no significant change in the selectivity's of products. The Table 3 and Figure 1 show the summary.

Table 4.3: Reaction condition: Catalyst size = fine powder pelletized and sieved with 40-60 mesh size, P = Atmospheric pressure (Bypass BPRs), Flow rate = 12 SCCM, T = 350 ˚C, Feed composition = 15% C_2H_6, 10% O_2, 5% CH_4, and balance helium, (PT) – post treatment.

Catalyst	**T(°C)**	**C_2H_6 Conv. (%)**	**C_2H_4 Sel. (%)**	**CO Sel. (%)**	**CO_2 Sel. (%)**	**HOAc Sel. (%)**	**Conv. lost compared to no feed C_2H_4 (%)**
USC 2.5 PT before C_2H_4 co-feed	300	8.61	97.21	1.02	0.87	0.89	N/A
	325	20.69	96.73	1.37	1.03	0.87	N/A
	350	47.66	93.83	2.79	1.57	1.81	N/A
USC 2.5 PT after 15% C2H4 co-feed at 350°C	300	7.57	96.67	1.30	1.01	1.03	12.08
	325	17.80	96.42	1.48	1.15	0.95	13.97
	350	40.56	94.27	2.82	1.52	1.40	14.90

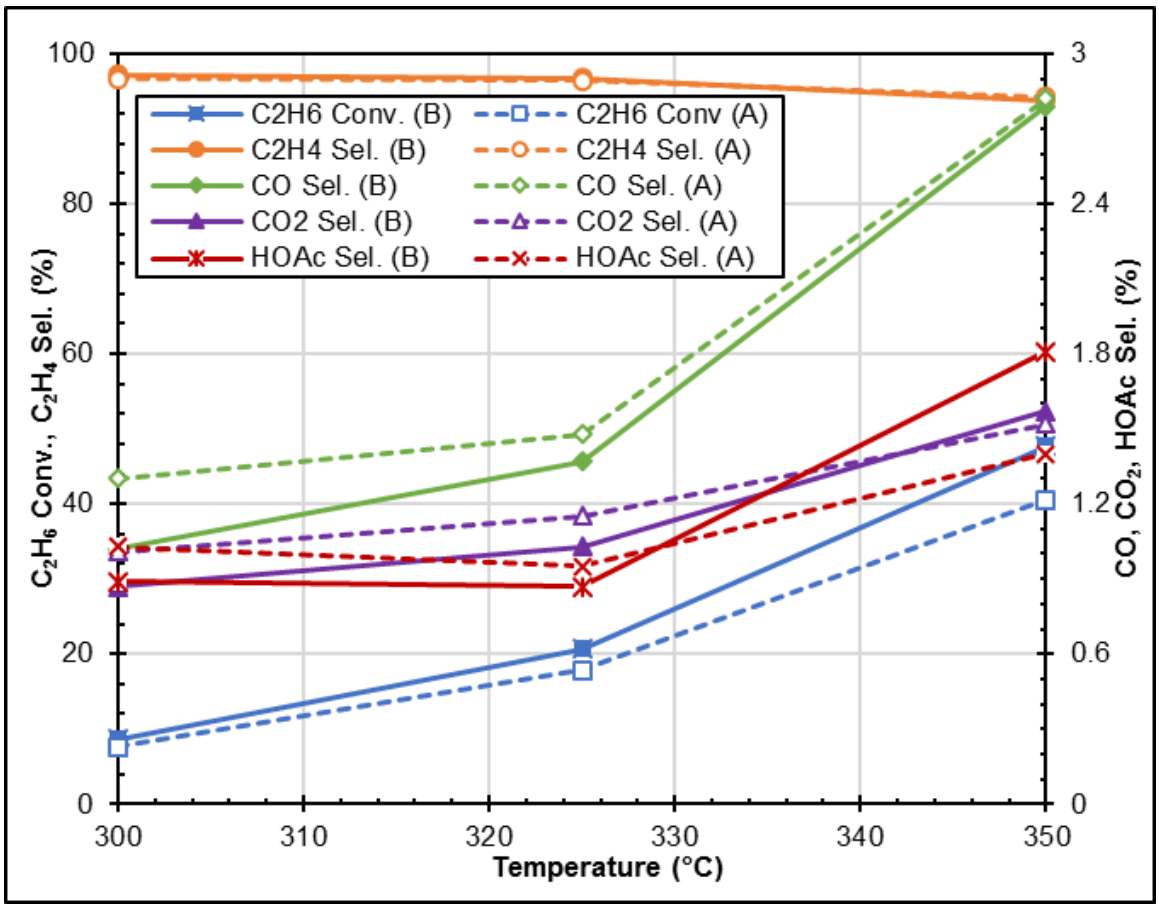

Figure 4:1 C_2H_6 conversion and product selectivity's. The solid line (or the letter "B") and the dashed line (---) (or the letter "A") are indicative of before and after 15% C_2H_4 co-feeding, respectively.

The C_2H_4 amount in the feed was changed and randomized to see the effect of ethylene on catalyst performance. The experiments started with fresh loaded catalyst. Table 4 shows the catalyst has lower activity while the concentration of ethylene is higher. However, interestingly the decreased activity (from 47.22% to ~40.2% ethane conversion) when ethylene is added to the feed does not depend on the percentage of C_2H_4 in the feed. Although after C_2H_4 addition to the feed the catalyst was deactivated, the activity remained the same (~40.2% C_2H_6 conversion) after the prior damage.

Table 4.4: Reaction condition: Catalyst = USC2.4 PT (PT is post treated catalyst), Catalyst size = fine powder pelletized and sieved with 40-60 mesh size, P = Atmospheric pressure (Bypass BPRs), Flow rate = 12 SCCM, T = 350 ˚C, Feed composition = 15% C_2H_6, 10% O_2, 5% CH_4, different amount of C_2H_4, and balance helium.

Feed C_2H_4 (%)	C_2H_6 Conv. (%)	O_2 Conv. (%)	Conv. lost compared to no feed C_2H_4 (%)
0	47.22	44.97	0.0
25	24.71	35.93	47.7
10	34.99	35.46	25.9
15	32.77	36.26	30.6
0	40.23	36.29	14.8
15	33.04	36.83	30.0
0	40.18	36.13	14.9
25	24.5	35.69	48.1
0	40.65	35.56	13.9
15	33.17	37.09	29.8
10	35.27	34.91	25.3
0	40.51	36.28	14.2

Due to the effect of ethylene on the catalyst activity and the importance of stability, the catalyst was exposed to the feed stream containing 15% C_2H_4, 15% C_2H_6, 10% O_2, 5% CH_4, and balance helium for 12 hrs at 350°C and 0psig before stating the kinetics experiments. Following the ethylene pretreatment, the catalyst showed the stability after 240hrs time on stream. In order to confirm the catalyst did not lose the activity, after each set of experiments the catalyst activity were tested and compared to the standard condition (P = 0 psig, Flow rate = 12 SCCM, T = 350˚C, Feed composition = 15% C_2H_6, 10% O_2, 5% CH_4, and balance helium). Surprisingly, no deactivation was

observed during kinetics study and the same catalyst was used for the entire set of evaluation.

4.3 Results and discussion

4.3.1 Catalyst characterization

XRD was performed and WPPF analysis indicates 97.6% M1 phase and 2.4% M2 phase for the USC 2PT. The XRF results confirmed the composition did not change during the reaction. Figure 2 shows the adsorption/desorption isotherm and BJH adsorption for fresh catalyst before reaction and spent catalyst post reaction. BJH indicates minimal change of mesoporous surface area. Isotherms have identical shapes yet downshifted post-rxn indicating loss of some microporous surface area. The N_2 BET was performed and the surface area of fresh and spent catalyst are 15 and 10.4 m^2/gr, respectively.

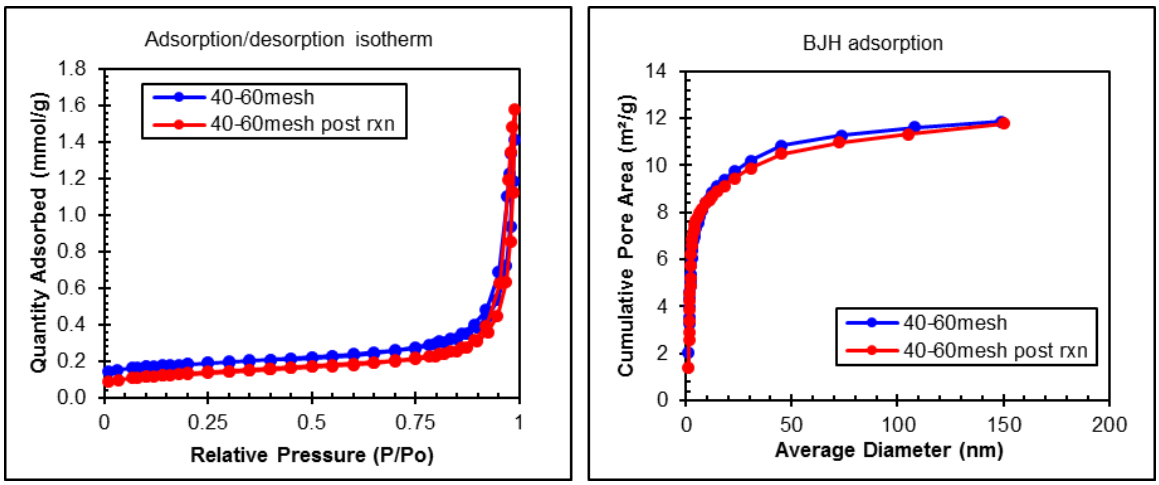

Figure 4.2: Adsorption/desorption isotherm and BJH adsorption for catalyst before and after reaction.

4.3.2 Reaction order for reactants (O_2 and C_2H_6)

Before starting any kinetics study, the stability test has performed on the catalyst. The catalyst activity for 100 hours shows no change in ethane conversion or selectivity of any product (Figure 3A). The temperature among the catalyst bed was measured to assure the smooth temperature profile among the catalyst bed. Figure 3B shows the temperature for 12 different profiles. The similarity of the profiles and the difference of only 1.8°C for 2-inch bed catalyst assure there is no hotspot and the bed has the same temperature while studying the kinetics. It should be noted that the temperature measurement was done by an omega k-type thermocouple (OD = 0.062”) with in a cannula (OD = 1/16”) with a silver solder end. The cannula was sealed with a graphite ferrule (Restek, VG2, 40%Vespel/60%graphite) that make the temperature measurement possible when the reaction is occurring at higher pressure.

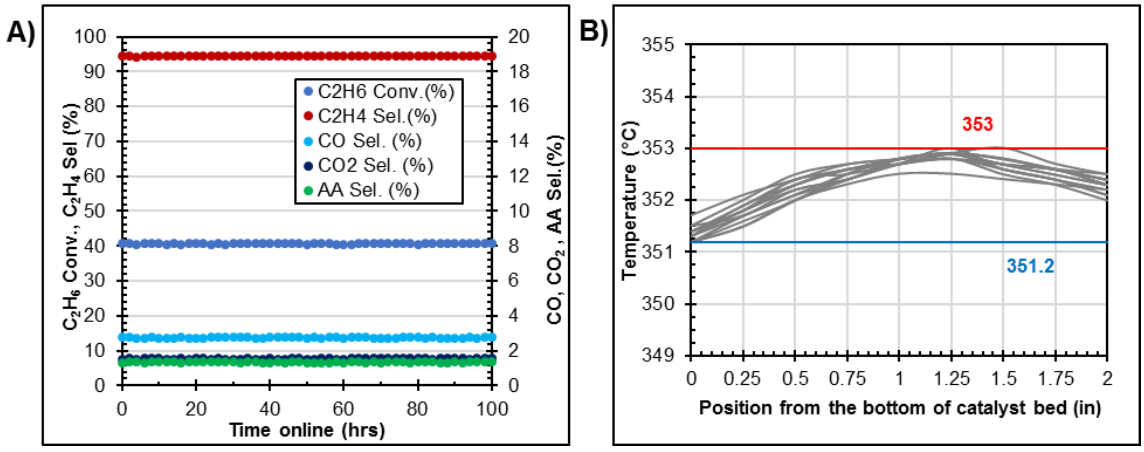

Figure 4.3: A) Long term catalyst stability, B) Temperature profile in the catalyst bed for 12 different profiles.

After confirmation of catalyst stability and uniform temperature inside the catalyst bed, in the first part of the kinetic study, reaction orders of reactant were evaluated. To

achieve reaction order for oxygen, three temperatures of 275, 310, and 350°C were chosen. At each temperature, feed compositions except for oxygen held at the same level of 15% C_2H_6, 5% CH_4 (as an internal standard), balance He. Oxygen concentration varied from 2.5-20%. The reaction order evaluated for three pressures of 0, 60, and 120 psig. The flow rates adjusted to keep the contact time the same. Figure 4 shows the oxygen reaction order for ethane conversion and the products formation (CO, CO_2, and C_2H_4). The plot is just for a chosen condition of 350°C and 120 psig. From the slope of this plot reaction order of oxygen is measured. Oxygen shows pseudo-zero order for ethane conversion and ethylene formation. This oxygen independency suggests a fast oxygen cycle for this reaction which is not common for an oxidative reaction unless the mechanism is Mars-Van Krevelen (MVK). The oxygen reaction order for CO and CO_2 is larger than that of C_2H_4 which suggests achieving the favorable product of C_2H_4 can happen when the feed is oxygen lean. It should be noted that the catalyst is mixed oxide catalyst and presence of enough oxygen is critical. For the operational standpoint the reaction needs to occur in the low enough oxygen in feed to have higher amount of ethylene produced while the catalyst is not suffering from low oxygen concentration environment.

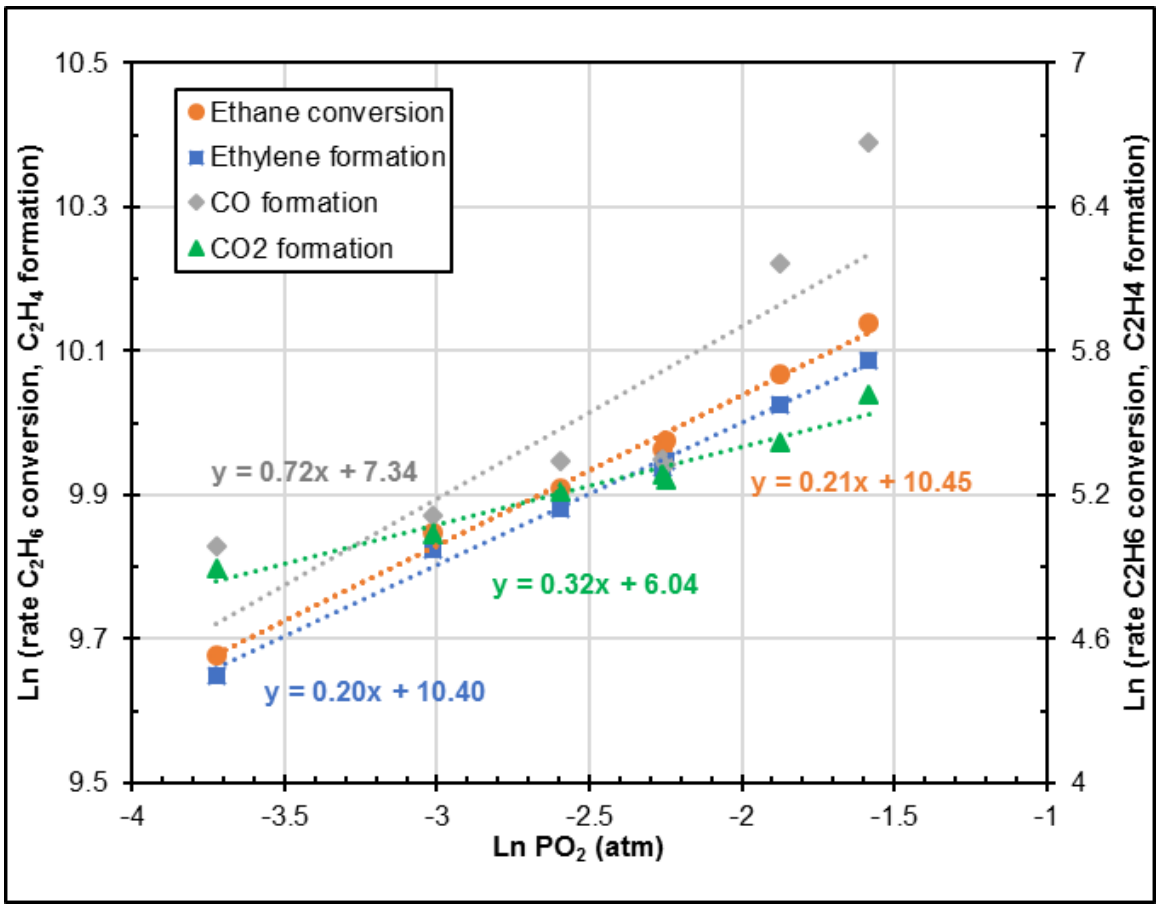

Figure 4.4: O_2 reaction order for C_2H_6 conversion and for C_2H_4, CO, and CO_2 rate of formation. Reaction occurs at T = 350°C, P = 120psig.

For C_2H_6 reaction order, the feed gas composition held the same except for C_2H_6 which varies from 5% to 25%. The O_2 mole percentage is 10.5%, CH_4 as an internal standard is 5% and the balance is helium. Figure 5 indicates the ethane reaction order at 350°C and 120 psig. The ethane reaction order of 0.81 for ethane conversion suggests ethane activation, probably a C-H bond cleavage, is the rate determining step. The reaction order, the slope of the line, is higher for ethylene formation compares to CO and CO_2 formation. This higher reaction order for the favorable product suggests ethane rich feed.

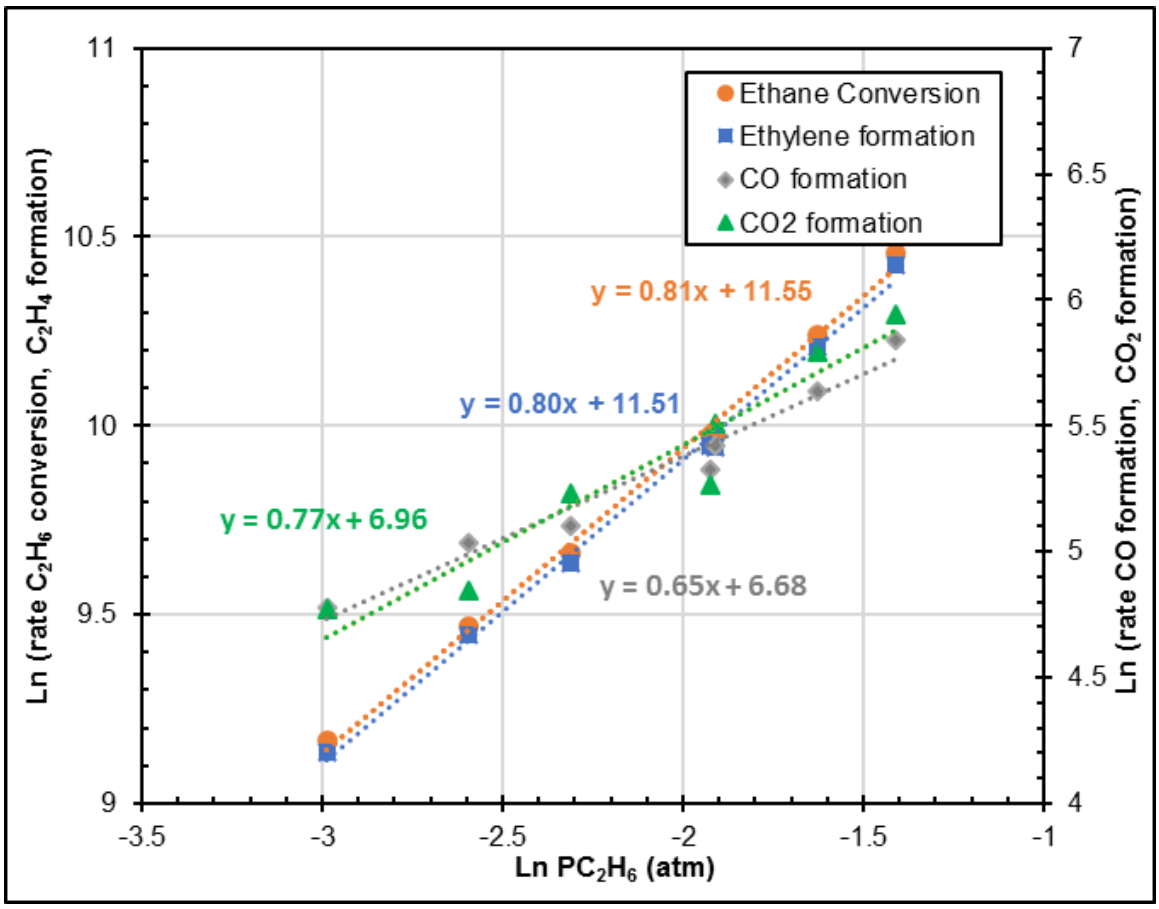

Figure 4.5: C_2H_6 reaction order at 350°C and 120 psig.

The summary of activation energies and reactants reaction orders for three temperature of 275, 310, and 350°C and pressures of 0, 60, and 120 psig is shown in Table 5. For C_2H_4 formation, ethane shows reaction order of about 0.78 in all the pressures and temperatures and oxygen has pseudo zero order. Regarding CO and CO_2 formation, for all the temperatures and pressures the ethane reaction order is lower compares to C_2H_4 formation. On the other hand, in all reaction conditions oxygen reaction order is higher for CO and CO_2 formation compared to C_2H_4 formation. The results suggest Mars-Van Krevelen lattice oxide ion reaction mechanism. The oxygen for ODH reaction is provided by the lattice oxide and afterward the reduced metals were reoxidezed by ions in the gas phase oxygen to make oxide.

Table 4.5: Energetics and kinetics summary.

		0 psig					60 psig					120 psig				
C_2H_6 reaction orders	O_2 =10.5% C_2H_6=5-25%	T, C	C_2H_6	C_2H_4	CO	CO_2	T, C	C_2H_6	C_2H_4	CO	CO_2	T, C	C_2H_6	C_2H_4	CO	CO_2
		275	1.10	1.10	0.65	0.41	275	0.79	0.79	0.81	0.50	275	0.67	0.66	0.95	0.57
		310	0.81	0.81	0.61	0.40	310	0.77	0.77	0.55	0.51	310	0.63	0.63	0.59	0.56
		350	0.82	0.82	0.52	0.63	350	0.81	0.81	0.65	0.61	350	0.81	0.80	0.65	0.77
O_2 reaction orders	C_2H_6=15 %, O_2=2.5-20%	T, C	C_2H_6	C_2H_4	CO	CO_2	T, C	C_2H_6	C_2H_4	CO	CO_2	T, C	C_2H_6	C_2H_4	CO	CO_2
		275	0.21	0.20	0.53	0.33	275	0.15	0.13	1.08	0.27	275	0.17	0.15	0.89	0.38
		310	0.13	0.13	0.15	0.21	310	0.17	0.16	0.82	0.30	310	0.17	0.15	0.86	0.46
		350	0.12	0.12	0.15	0.21	350	0.17	0.16	0.63	0.33	350	0.21	0.20	0.72	0.32
E_{act}	C_2H_6=15 %, O_2=10.5%	E_{act}	C_2H_6	C_2H_4	CO	CO_2	E_{act}	C_2H_6	C_2H_4	CO	CO_2	E_{act}	C_2H_6	C_2H_4	CO	CO_2
		kcal/mol	24.6	24.6	28.0	25.1	kcal/mol	27.2	27.2	31.7	38.5	kcal/mol	30.5	30.5	32.3	29.1

In the context of activation energy for all three pressures, the activation energy for formation of combustion products (CO_x) is larger than activation energy for C_2H_4 formation. The recommendation for the reaction condition is lower temperature. It is worth mentioning the temperature must be high enough to activate the reactants and produce economically reasonable amount of ethylene. Higher pressure shows higher activation energies

4.3.3 Reaction order for products (C_2H_4, CO_2, and H_2O)

In order to investigate the reaction order for products the pressure of 120psig was chosen among the three pressures. For the CO_2 reaction order study, the feed composition was 15%C_2H_6, 10% O_2, 5% CH_4, 0.05-7.5% CO_2. Figure 6 shows variation of CO_2 composition in this range does not change the ethane conversion and ethylene formation. It is worth noting the maximum mole percent of CO_2 produced in the reaction is about 0.05%. The CO_2 reaction order is zero.

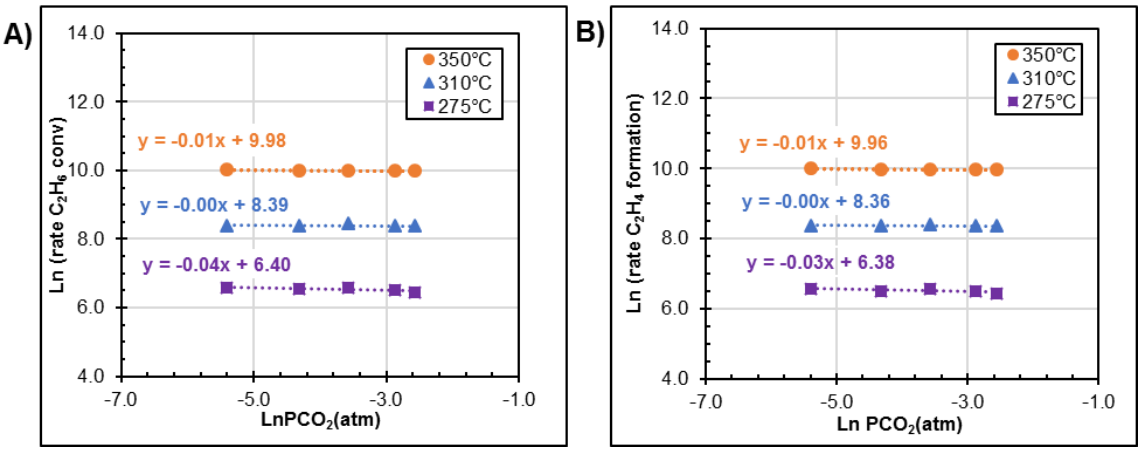

Figure 4.6: CO_2 reaction order. A) for ethane conversion. B) for ethylene formation.

For C_2H_4 reaction order study, the reaction pressure is 120psig and the feed composition is 10%O_2, 15% C_2H_6, 5%CH_4, 5%CH_4, 5-25%C_2H_4, and balance He. Figure

7 indicates the plots have negative slope showing the inhibition. Although it is not very strong inhibition, it was expected.

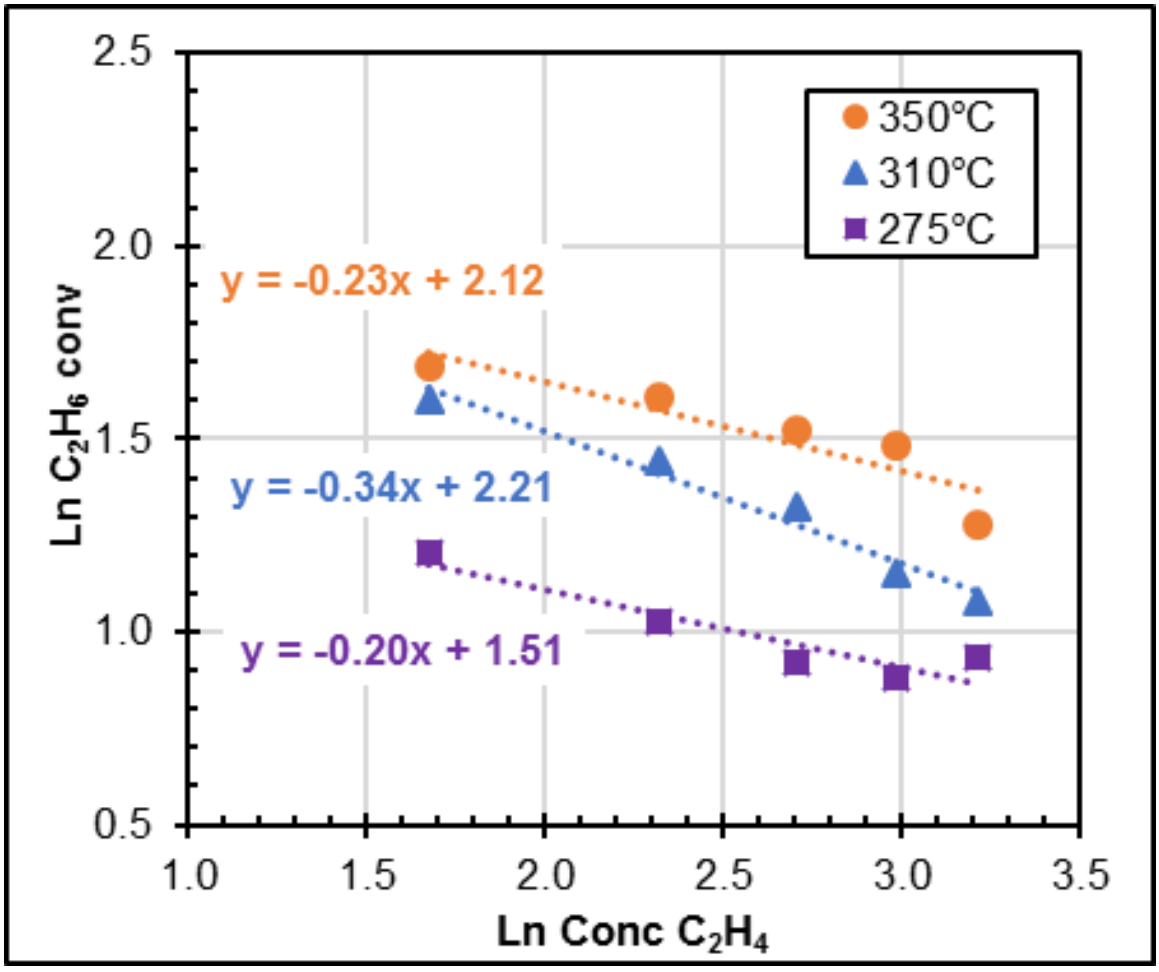

Figure 4.7: C_2H_4 reaction order.

To understand the nature of C_2H_4 oxidation, the reaction condition was 120 psig and three different temperatures of 275, 310, and 350 °C. The ethylene concentration of 5, 15, 25% and oxygen concentration of 2, 5, and 10% were used. Figure 8 shows that the oxygen reaction order is about -0.43 for all the ethylene concentrations. The similar oxygen reaction order suggests the same mechanism for different amount of ethylene exists. At the same oxygen concentration level, increasing ethylene concentration will result in ethylene conversion increasing.

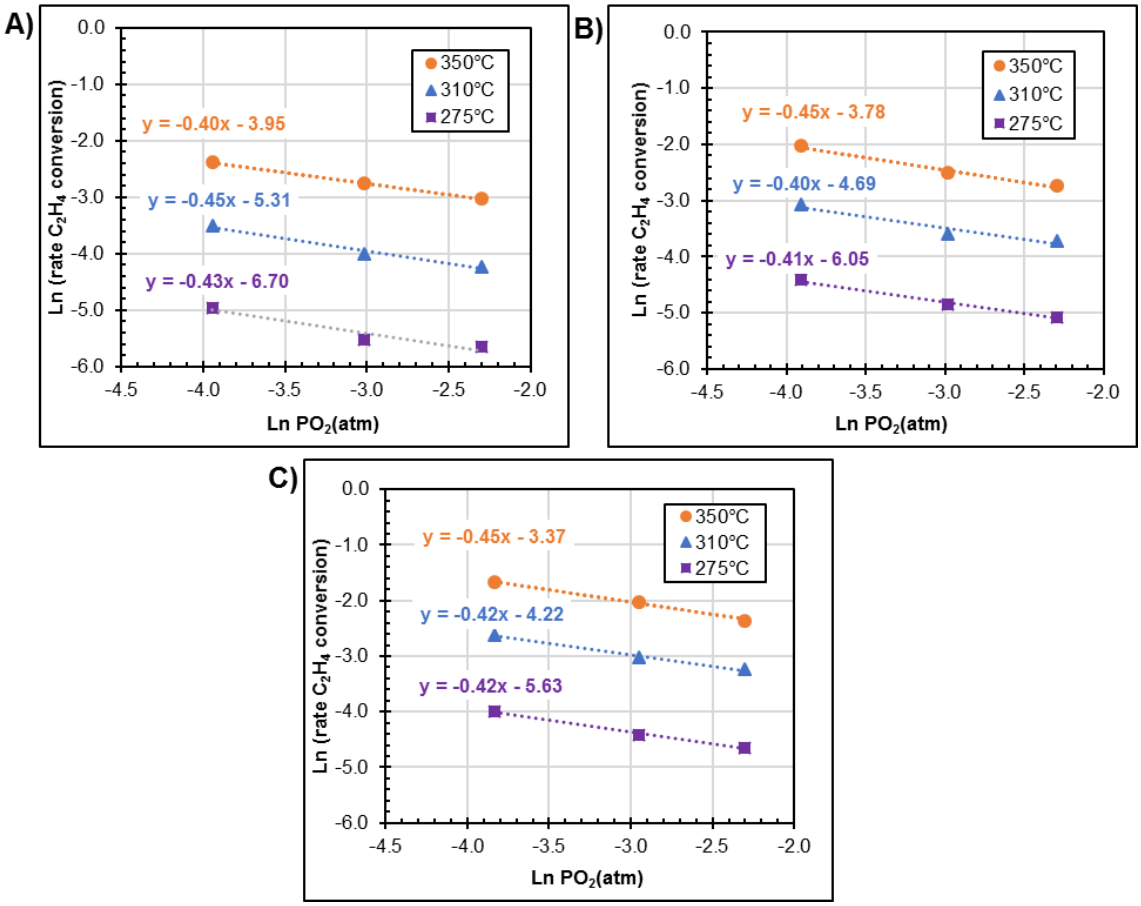

Figure 4.8: C_2H_4 oxidation A)5%C_2H_4. B)15%C_2H_4. C)25%C_2H_4.

The activation energy for ethylene oxidation were measured at 120psig and for 5, 10, 15, 20, and 25% and the activation energies are 23.7, 23.4, 21.3, 18.9, and 20.7 kcal/mol, respectively. Lower activation energy of ethylene oxidation compared to ethane oxidation suggests low temperature favors the former reaction. However, It is worth mentioning that in the operational temperature reaction range the rate of ethane conversion is more than that of the ethylene. Figure 9 shows the isokinetic point of 113K. Below this temperature the kinetics dictate higher rate of conversion for ethylene.

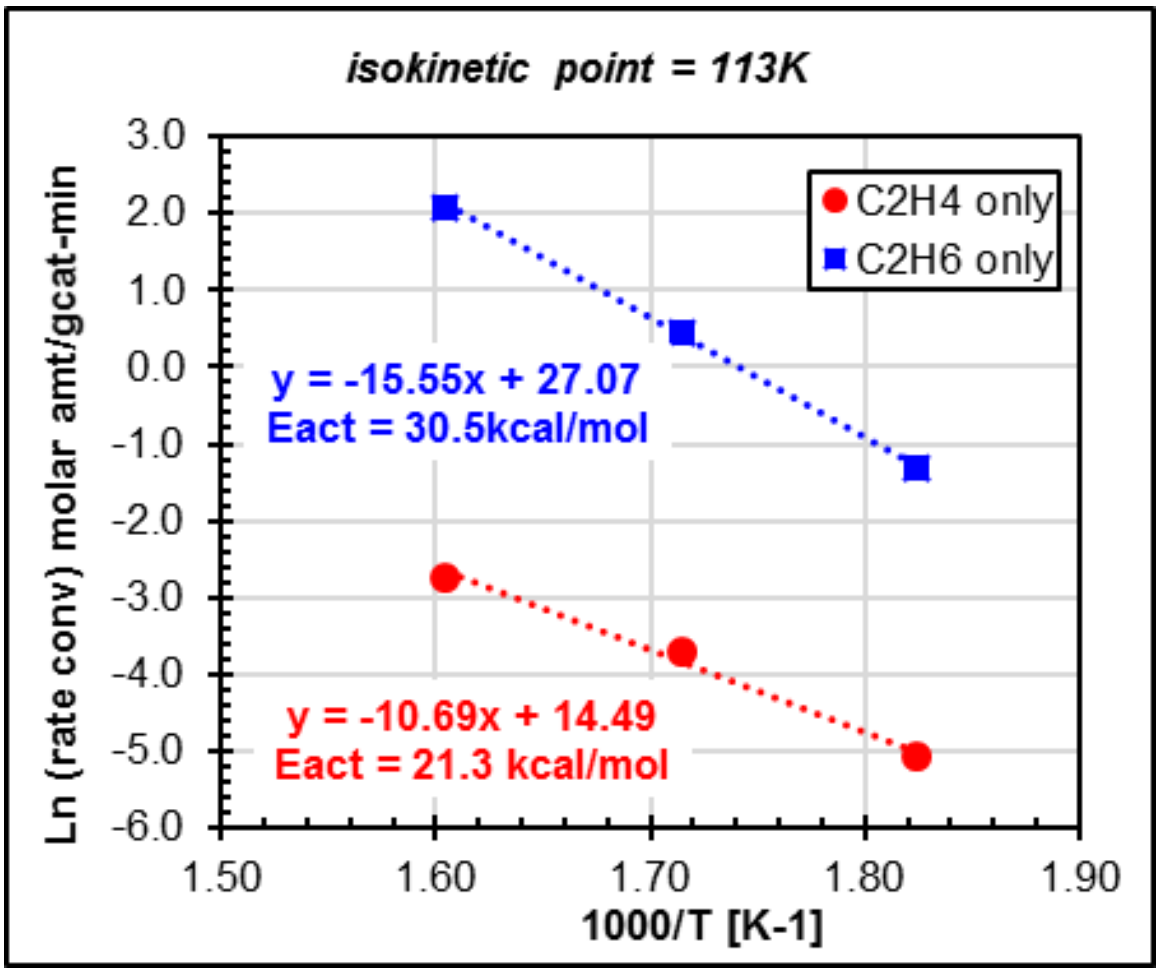

Figure 4.9: Isokinetic point.

Next, water cofeed was studied. The GC used to quantify the amount of water was another GC equipped with Pora PlotQ column for TCD in adjacent, less than 5 ft, of the reactor setup. The water was fed to the reactor in vapor phase using vapor liquid equilibrium (VLE). A split stream of feed for PFR4 after passing through VLE was sent to the GC for confirmation of water content. The GC was calibrated for water quantification. Figure 10 shows the schematic PFR4 with VLE attachment.

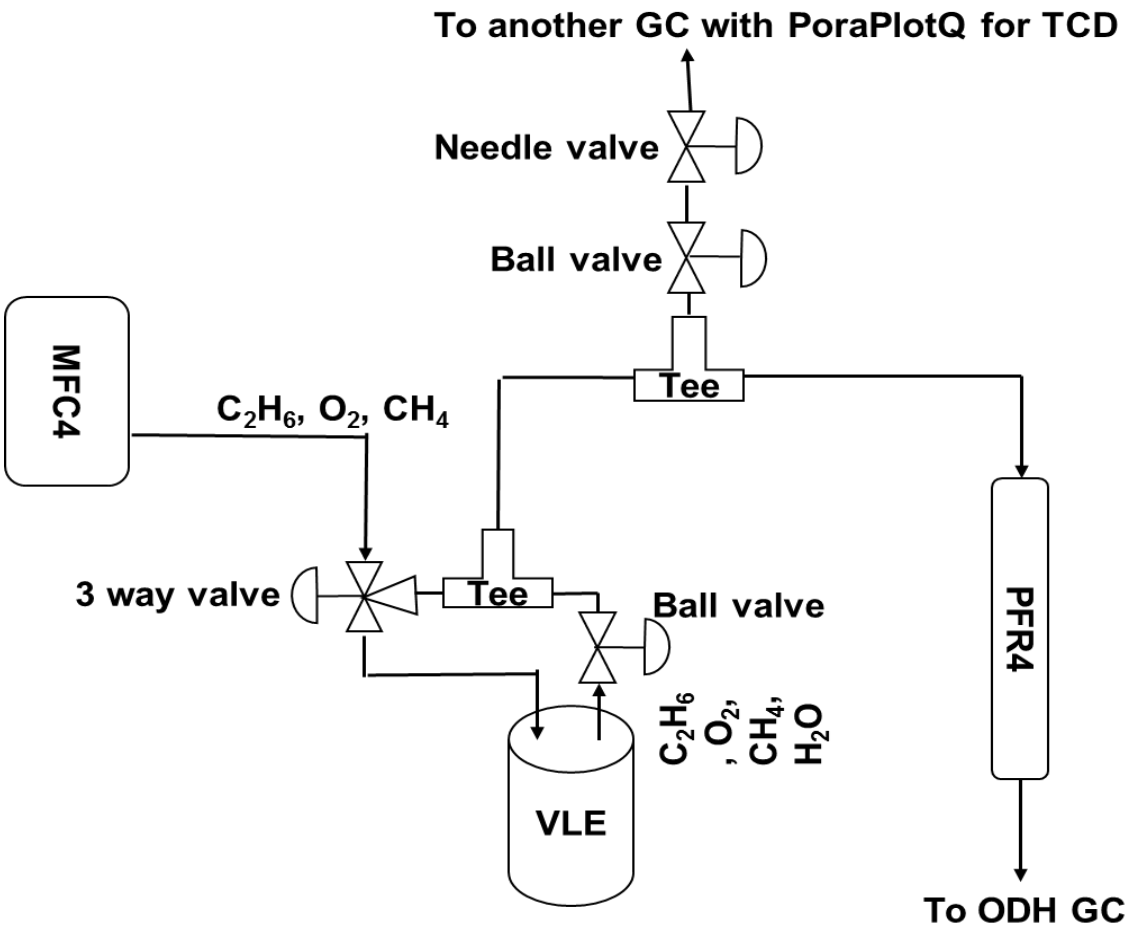

Figure 4.10: Schematic of PFR4 with VLE assembly.

The water addition was studied at pressures of 60 and 120 psig. Figure 11 shows for both pressures the selectivity's of ethylene and acetic acid did not change after addition of up to 5% water. 20% water addition was not done for 120 psig due to operational difficulties. The amount of water produced in the ODH reaction calculated based on the stoichiometry (Equation 1) for 60 and 120 psig are 4.8 and 5.2%, respectively. In Equation 1 the Loop volume is the tube volume that its content was injected to GC for analysis.

$$mole\%\ water\ = \frac{mole\ C_2H_4 + 3 * mole\ CO_x}{Loop\ volume} \quad (4.1)$$

The results show that water addition decreases the C_2H_4 selectivity while keeping the ethane conversion the same. Increasing in acetic acid formation can be explained by the existence of hydroxyl group on the surface when water is added. This observation is consistent with the work from Vasilli et al.,[85] in which they showed the water dissociates spontaneously on the reduced vanadium sites forming the surface hydroxyl groups HO-V^{4+}-O-V^{4+}-OH which do not desorb as H_2O in the gas phase due to high stability. The hydroxyl group presence on the surface favors the acetic acid production reaction.

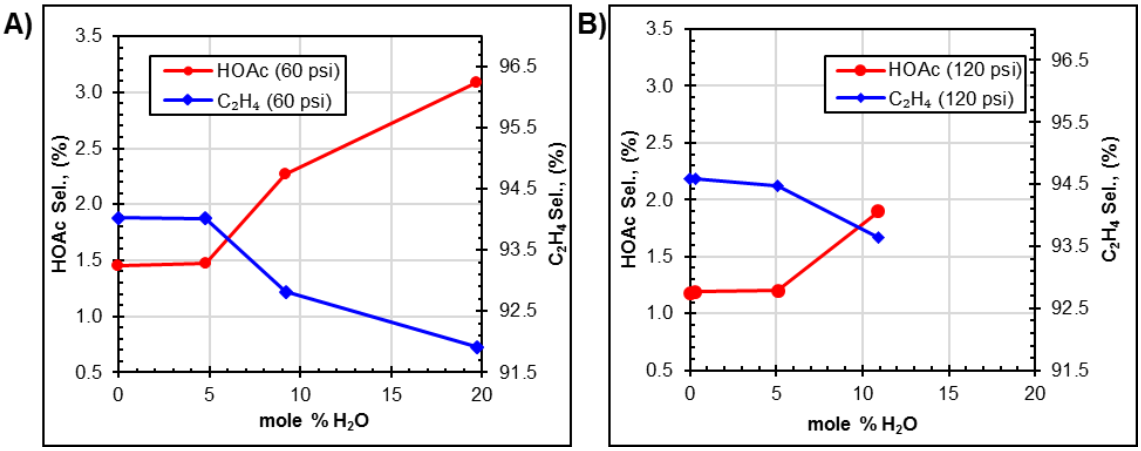

Figure 4.11: C_2H_4 and HOAc selectivity's vs amount of water added to the system.

4.4 Conclusions

The catalyst was prepared by slurry method and showed high stability and activity. The catalyst was evaluated in order to achieve reaction orders for reactants and products. A wide range of reaction conditions were used including three pressures (0, 60, and 120psig) and temperatures (310, 325, and 350°C), concentration range of 5-20% for O_2, 5-25% for C_2H_6, 0.05-7.5% for CO_2, and 5-25% for C_2H_4. The catalyst was exposed to 15%C_2H_4 as co feed prior to kinetics study. This pretreatment was performed due to the one-time deactivation in presence of C_2H_4. It was confirmed that after aforementioned pretreatment the catalyst held the activity. The stability tests were performed by

evaluation in the standard reaction condition (15% C_2H_6, 10%O_2, 5% CH_4, balance He, 0 psig, and 350°C)after each set of experiment to confirm no deactivation occurred during kinetics study.

The reaction order for oxygen in the ODH reaction was found to be pseudo zero order suggesting the Mars-Van Krevelen (MVK) mechanism. The oxygen reaction order for C_2H_4 is lower than that of combustion products recommending an oxygen lean reaction condition.

Ethane reaction order, on the other hand, appeared to be about 0.8. The reaction order of close to one for ethane indicates the rate determining step (RDS) is bond breaking in ethane, presumably the C-H bond cleavage. Higher reaction orders of ethane for ethylene formation compared to combustion products formation suggest ethane rich feed for optimal reaction condition.

CO_2 addition even at high concentration to the feed had no effect on the ethane conversion and ethylene selectivity. On the other hand, presence of ethylene in the feed caused strong inhibition as expected. However, the activation energy results suggested the lower reaction temperature favor the C_2H_4 formation.

It should be noted the suggested reaction condition for optimal operation need to be reasonable from the economic point of view. For instance, the low temperature is suggested, yet the temperature cannot be very low that no reaction occurs. The suggested oxygen lean environment demands to be chosen not to deactivate the catalyst which is metal oxide.

REFERENCES

1. Forzatti, P.; Lietti, L., Catalyst deactivation. *Catal. Today* **1999,** *52* (2), 165-181.

2. Bartholomew, C. H., Mechanisms of catalyst deactivation. *Appl. Catal., A* **2001,** *212* (1), 17-60.

3. Barbier, J., Deactivation of reforming catalysts by coking-a review. *Appl. Catal.* **1986,** *23* (2), 225-243.

4. Srokol, Z.; Bouche, A.-G.; van Estrik, A.; Strik, R. C. J.; Maschmeyer, T.; Peters, J. A., Hydrothermal upgrading of biomass to biofuel; studies on some monosaccharide model compounds. *Carbohydr. Res.* **2004,** *339* (10), 1717-1726.

5. Shelef, M.; McCabe, R. W., Twenty-five years after introduction of automotive catalysts: what next? *Catal. Today* **2000,** *62* (1), 35-50.

6. Pakhare, D.; Spivey, J., A review of dry (CO 2) reforming of methane over noble metal catalysts. *Chem. Soc. Rev.* **2014,** *43* (22), 7813-7837.

7. Horiuchi, T.; Chen, L.; Osaki, T.; Sugiyama, T.; Suzuki, K.; Mori, T., A novel alumina catalyst support with high thermal stability derived from silica-modified alumina aerogel. *Catal. Lett.* **1999,** *58* (2), 89-92.

8. Ozawa, M., Thermal stabilization of catalytic compositions for automobile exhaust treatment through rare earth modification of alumina nanoparticle support. *J. Alloys Compd.* **2006,** *408-412,* 1090-1095.

9. Tomiyama, S.; Takahashi, R.; Sato, S.; Sodesawa, T.; Yoshida, S., Preparation of Ni/SiO2 catalyst with high thermal stability for CO2-reforming of CH4. *Appl. Catal., A* **2003,** *241* (1), 349-361.

10. Lim, S.; Wang, C.; Yang, Y.; Ciuparu, D.; Pfefferle, L.; Haller, G. L., Evidence for anchoring and partial occlusion of metallic clusters on the pore walls of MCM-41 and effect on the stability of the metallic clusters. *Catal. Today* **2007,** *123* (1), 122-132.

11. Liu, X.; Wang, A.; Yang, X.; Zhang, T.; Mou, C.-Y.; Su, D.-S.; Li, J., Synthesis of Thermally Stable and Highly Active Bimetallic Au−Ag Nanoparticles on Inert Supports. *Chem. Mater.* **2009,** *21* (2), 410-418.

12. Wang, D.; Villa, A.; Porta, F.; Prati, L.; Su, D., Bimetallic Gold/Palladium Catalysts: Correlation between Nanostructure and Synergistic Effects. *J. Phys. Chem. C* **2008,** *112* (23), 8617-8622.

13. Oh, S. H.; Carpenter, J. E., Platinum-rhodium synergism in three-way automotive catalysts. *J. Catal.* **1986,** *98* (1), 178-190.

14. Vogel, D.; Spiel, C.; Suchorski, Y.; Trinchero, A.; Schlögl, R.; Grönbeck, H.; Rupprechter, G., Local Catalytic Ignition during CO Oxidation on Low-Index Pt and Pd Surfaces: A Combined PEEM, MS, and DFT Study. *Angew. Chem., Int. Ed.* **2012,** *51* (40), 10041-10044.

15. Diao, W.; Tengco, J. M. M.; Gaffney, A. M.; Regalbuto, J. R.; Monnier, J. R., Rational synthesis of bimetallic catalysts using electroless deposition methods. In *Catalysis: Volume 32*, The Royal Society of Chemistry: 2020; Vol. 32, pp 116-150.

16. Rebelli, J.; Detwiler, M.; Ma, S.; Williams, C. T.; Monnier, J. R., Synthesis and characterization of Au–Pd/SiO2 bimetallic catalysts prepared by electroless deposition. *J. Catal.* **2010,** *270* (2), 224-233.

17. Kokkinidis, G.; Papoutsis, A.; Stoychev, D.; Milchev, A., Electroless deposition of Pt on Ti—catalytic activity for the hydrogen evolution reaction. *J. Electroanal. Chem.* **2000,** *486* (1), 48-55.

18. Schaal, M. T.; Pickerell, A. C.; Williams, C. T.; Monnier, J. R., Characterization and evaluation of Ag–Pt/SiO2 catalysts prepared by electroless deposition. *J. Catal.* **2008,** *254* (1), 131-143.

19. Gallagher, J. R.; Li, T.; Zhao, H.; Liu, J.; Lei, Y.; Zhang, X.; Ren, Y.; Elam, J. W.; Meyer, R. J.; Winans, R. E.; Miller, J. T., In situ diffraction of highly dispersed supported platinum nanoparticles. *Catal. Sci. Technol.* **2014,** *4* (9), 3053-3063.

20. Song, Y.-J.; Monnier, J. R.; Fanson, P. T.; Williams, C. T., Bimetallic Ag–Ir/Al 2 O 3 catalysts prepared by electroless deposition: Characterization and kinetic evaluation. *J. Catal.* **2014,** *315*, 59-66.

21. Beard, K.; Schaal, M.; Van Zee, J.; Monnier, J., Preparation of highly dispersed PEM fuel cell catalysts using electroless deposition methods. *Appl. Catal., B* **2007,** *72* (3), 262-271.

22. Regalbuto, J., Catalyst Preparation: Science and Engineering. CRC Press: 2016; pp 297-318.

23. Regalbuto, J. R., Electrostatic Adsorption. In *Synthesis of Solid Catalysts*, Jong, K. P. d., Ed. 2009; pp 33-58.

24. Overbury, S. H.; Bertrand, P. A.; Somorjai, G. A., Surface composition of binary systems. Prediction of surface phase diagrams of solid solutions. *Chem. Rev.* **1975,** *75* (5), 547-560.

25. Vitos, L.; Ruban, A. V.; Skriver, H. L.; Kollár, J., The surface energy of metals. *Surf. Sci.* **1998,** *411* (1), 186-202.

26. Perdew, J. P.; Burke, K.; Ernzerhof, M., Generalized Gradient Approximation Made Simple. *Phys. Rev. Lett.* **1996,** *77* (18), 3865-3868.

27. Grimme, S.; Ehrlich, S.; Goerigk, L., Effect of the damping function in dispersion corrected density functional theory. *J. Comput. Chem.* **2011,** *32* (7), 1456-1465.

28. Kresse, G.; Furthmüller, J., Efficient iterative schemes for ab initio total-energy calculations using a plane-wave basis set. *Phys. Rev. B* **1996,** *54* (16), 11169-11186.

29. Kresse, G.; Joubert, D., From ultrasoft pseudopotentials to the projector augmented-wave method. *Phys. Rev. B* **1999,** *59* (3), 1758-1775.

30. Reber, A. C.; Khanna, S. N., Effect of Embedding Platinum Clusters in Alumina on Sintering, Coking, and Activity. *J. Phys. Chem. C* **2017,** *121* (39), 21527-21534.

31. Tran, R.; Xu, Z.; Radhakrishnan, B.; Winston, D.; Sun, W.; Persson, K. A.; Ong, S. P., Surface energies of elemental crystals. *Sci. Data* **2016,** *3* (1), 160080.

32. Harris, P. J. F., The sintering of platinum particles in an alumina-supported catalyst: Further transmission electron microscopy studies. *J. Catal.* **1986,** *97* (2), 527-542.

33. Voorhees, P. W., The theory of Ostwald ripening. *J. Stat. Phys.* **1985,** *38* (1), 231-252.

34. Wettergren, K.; Schweinberger, F. F.; Deiana, D.; Ridge, C. J.; Crampton, A. S.; Rötzer, M. D.; Hansen, T. W.; Zhdanov, V. P.; Heiz, U.; Langhammer, C., High Sintering Resistance of Size-Selected Platinum Cluster Catalysts by Suppressed Ostwald Ripening. *Nano Lett.* **2014,** *14* (10), 5803-5809.

35. Gamboa, G. U.; Reber, A. C.; Khanna, S. N., Electronic subshell splitting controls the atomic structure of charged and neutral silver clusters. *New J. Chem.* **2013,** *37* (12), 3928-3935.

36. Ferrando, R.; Jellinek, J.; Johnston, R. L., Nanoalloys: From Theory to Applications of Alloy Clusters and Nanoparticles. *Chem. Rev.* **2008,** *108* (3), 845-910.

37. Gérard Bergeret, P. G., Particle Size and Dispersion Measurements. In *Handbook of Heterogeneous Catalysis*, G. Ertl, H. K., F. Schüth, J. Weitkamp, Ed. 2008.

38. Hansen, M.; Elliott, R. P.; Shunk, F. A.; Research, I., *Constitution of binary alloys*. McGraw-Hill: New York, 1958.

39. Krishnamurthy, S.; Landolt, G. R.; Schoennagel, H. J., The stoichiometry of hydrogen and CO chemisorption on Irγ-Al2O3. *J. Catal.* **1982,** *78* (2), 319-326.

40. Duivenvoorden, F.; Kip, B.; Koningsberger, D.; Prins, R., DETERMINATION OF THE METAL PARTICLE SIZE OF SUPPORTED Pt, Rh, AND Ir CATALYSTS. A CALIBRATION OF HYDROGEN CHEMISORPTION BY EXAFS. *J. Phys. Colloq.* **1986,** *47* (C8), C8-227-C8-230.

41. Kaspar, T. C.; Droubay, T.; Chambers, S. A.; Bagus, P. S., Spectroscopic Evidence for Ag(III) in Highly Oxidized Silver Films by X-ray Photoelectron Spectroscopy. *J. Phys. Chem. C* **2010,** *114* (49), 21562-21571.

42. Ruban, A. V.; Skriver, H. L.; Nørskov, J. K., Surface segregation energies in transition-metal alloys. *Phys. Rev. B* **1999,** *59* (24), 15990-16000.

43. Han, C. W.; Majumdar, P.; Marinero, E. E.; Aguilar-Tapia, A.; Zanella, R.; Greeley, J.; Ortalan, V., Highly Stable Bimetallic AuIr/TiO2 Catalyst: Physical Origins of the Intrinsic High Stability against Sintering. *Nano Lett.* **2015,** *15* (12), 8141-8147.

44. Okada, M.; Nakamura, M.; Moritani, K.; Kasai, T., Dissociative adsorption of hydrogen on thin Au films grown on Ir{111}. *Surf. Sci.* **2003,** *523* (3), 218-230.

45. Okada, M.; Ogura, S.; Diño, W. A.; Wilde, M.; Fukutani, K.; Kasai, T., Reactive gold thin films grown on iridium. *Appl. Surf. Sci.* **2005,** *246* (1), 68-71.

46. Ferrin, P. A.; Kandoi, S.; Zhang, J.; Adzic, R.; Mavrikakis, M., Molecular and Atomic Hydrogen Interactions with Au−Ir Near-Surface Alloys. *J. Phys. Chem. C* **2009,** *113* (4), 1411-1417.

47. Kong, L.; Li, J.; Zhao, Z.; Liu, Q.; Sun, Q.; Liu, J.; Wei, Y., Oxidative dehydrogenation of ethane to ethylene over Mo-incorporated mesoporous SBA-16 catalysts: The effect of MoOx dispersion. *Applied Catalysis A: General* **2016,** *510*, 84-97.

48. Qiao, A.; Kalevaru, V. N.; Radnik, J.; Martin, A., Oxidative dehydrogenation of ethane to ethylene over Ni–Nb–M–O catalysts: Effect of promoter metal and CO2-admixture on the performance. *Catalysis Today* **2016,** *264*, 144-151.

49. Rahmani, F.; Haghighi, M.; Amini, M., The beneficial utilization of natural zeolite in preparation of Cr/clinoptilolite nanocatalyst used in CO2-oxidative dehydrogenation of ethane to ethylene. *Journal of Industrial and Engineering Chemistry* **2015,** *31*, 142-155.

50. Zhu, H.; Rosenfeld, D. C.; Anjum, D. H.; Sangaru, S. S.; Saih, Y.; Ould-Chikh, S.; Basset, J.-M., Ni–Ta–O mixed oxide catalysts for the low temperature oxidative dehydrogenation of ethane to ethylene. *Journal of Catalysis* **2015,** *329*, 291-306.

51. Chu, B.; Truter, L.; Nijhuis, T. A.; Cheng, Y., Oxidative dehydrogenation of ethane to ethylene over phase-pure M1 MoVNbTeOx catalysts in a micro-channel reactor. *Catalysis Science & Technology* **2015,** *5* (5), 2807-2813.

52. Armstrong, R. D.; Freakley, S. J.; Forde, M. M.; Peneau, V.; Jenkins, R. L.; Taylor, S. H.; Moulijn, J. A.; Morgan, D. J.; Hutchings, G. J., Low temperature catalytic partial oxidation of ethane to oxygenates by Fe– and Cu–ZSM-5 in a continuous flow reactor. *Journal of Catalysis* **2015,** *330*, 84-92.

53. Zhu, H.; Laveille, P.; Rosenfeld, D. C.; Hedhili, M. N.; Basset, J.-M., A high-throughput reactor system for optimization of Mo–V–Nb mixed oxide catalyst composition in ethane ODH. *Catalysis Science & Technology* **2015,** *5* (8), 4164-4173.

54. Nguyen, T. T.; Aouine, M.; Millet, J. M. M., Optimizing the efficiency of MoVTeNbO catalysts for ethane oxidative dehydrogenation to ethylene. *Catalysis Communications* **2012,** *21*, 22-26.

55. Cheng, Y.; Zhang, F.; Zhang, Y.; Miao, C.; Hua, W.; Yue, Y.; Gao, Z., Oxidative dehydrogenation of ethane with CO2 over Cr supported on submicron ZSM-5 zeolite. *Chinese Journal of Catalysis* **2015,** *36* (8), 1242-1248.

56. Corma, A.; García, H., Lewis Acids as Catalysts in Oxidation Reactions: From Homogeneous to Heterogeneous Systems. *Chemical Reviews* **2002,** *102* (10), 3837-3892.

57. Leus, K.; Liu, Y.-Y.; Van Der Voort, P., Metal-Organic Frameworks as Selective or Chiral Oxidation Catalysts. *Catalysis Reviews* **2014,** *56* (1), 1-56.

58. Védrine, J. C., Heterogeneous Partial (amm)Oxidation and Oxidative Dehydrogenation Catalysis on Mixed Metal Oxides. *Catalysts* **2016,** *6* (2), 22.

59. Rouquerol, J.; Llewellyn, P.; Rouquerol, F., Is the bet equation applicable to microporous adsorbents? In *Studies in Surface Science and Catalysis*, Llewellyn, P. L.; Rodriquez-Reinoso, F.; Rouqerol, J.; Seaton, N., Eds. Elsevier: 2007; Vol. 160, pp 49-56.

60. Melzer, D.; Xu, P.; Hartmann, D.; Zhu, Y.; Browning, N. D.; Sanchez-Sanchez, M.; Lercher, J. A., Atomic-Scale Determination of Active Facets on the MoVTeNb Oxide M1 Phase and Their Intrinsic Catalytic Activity for Ethane Oxidative Dehydrogenation. *Angewandte Chemie International Edition* **2016,** *55* (31), 8873-8877.

61. Grasselli, R. K.; Burrington, J. D.; Buttrey, D. J.; DeSanto, P.; Lugmair, C. G.; Volpe, A. F.; Weingand, T., Multifunctionality of Active Centers in (Amm)oxidation Catalysts: From Bi–Mo–Oxto Mo–V–Nb–(Te, Sb)–Ox. *Topics in Catalysis* **2003,** *23* (1), 5-22.

62. Thorsteinson, E. M.; Wilson, T. P.; Young, F. G.; Kasai, P. H., The oxidative dehydrogenation of ethane over catalysts containing mixed oxides of molybdenum and vanadium. *Journal of Catalysis* **1978,** *52* (1), 116-132.

63. Ueda, W.; Oshihara, K., Selective oxidation of light alkanes over hydrothermally synthesized Mo-V-M-O (M=Al, Ga, Bi, Sb, and Te) oxide catalysts. *Applied Catalysis A: General* **2000**, *200*, 135–143.

64. Oshihara, K.; Hisano, T.; Ueda, W., Catalytic oxidative activation of light alkanes over Mo–V-based oxides having controlled surface. *Topics in Catalysis* **2001**, *15*, 153–160.

65. Lo´pez Nieto, J. M.; Botella, P.; Concepcio´n, P.; Dejoz, A.; Va´zquez, M. I., Oxidative dehydrogenation of ethane on Te-containing MoVNbO catalysts. *Catalysis Today* **2004**, *91–92*, 241–245.

66. Xie, Q.; Chen, L.; Weng, W.; Wan, H., Preparation of MoVTe(Sb)Nb mixed oxide catalysts using a slurry method for selective oxidative dehydrogenation of ethane. *Journal of Molecular Catalysis*. A: Chemical **2005**, *240*, 191–196.

67. Botella, P.; Dejoz, A.; Abello, M. C.; Va´zquez, M.I; Arru´a, L.;Lo´pez Nieto, J. M., Selective oxidation of ethane: Developing an orthorhombic phase in Mo–V–X (X = Nb, Sb, Te) mixed oxides. *Catalysis Today* **2009**, *142*, 272–277.

68. Konya, T.; Katou, T.; Murayama, T.; Ishikawa, S.; Sadakane, M.; Buttrey, D.;

Ueda, W., An orthorhombic Mo3VOxcatalyst most active for oxidative dehydrogenation of ethane among related complex metal oxides. *Catalysis Science & Technology* **2013**, *3*, 380–387.

69. Botella, P.; Garcı´a-Gonza´lez, E.; Dejoz, A.; Lo´pez Nieto, J. M.; Va´zquez, M. I.; Gonza´lez-Calbet, J., Selective oxidative dehydrogenation of ethane on MoVTeNbO mixed metal oxide catalysts. *Journal of Catalysis* **2004**, *225*, 428–438.

70. Cheng, M.-J.; Goddard, W. A., In Silico Design of Highly Selective Mo-V-Te-Nb-O Mixed Metal Oxide Catalysts for Ammoxidation and Oxidative Dehydrogenation of Propane and Ethane. *Journal of American Chemical Society* **2015**, *137*, 13224–13227.

71. Najari, S.; Saeidi, S.; Concepcion, P.; Dionysiou, D. D.; Bhargava, S. K.; Lee, A. F.; Wilson, K., Oxidative dehydrogenation of ethane: catalytic and mechanistic aspects and future trends. *Chemical Society Review* **2021**, *50*, 4564-4605.

72. Nguyen, T. T; Deniau, B.; Delichere, P.; Millet, J.-M. M., Influence of the Content and Distribution of Vanadium in the M1 Phase of the MoVTe(Sb)NbO Catalysts on their Catalytic Properties in Light Alkanes Oxidation. *Topics in Catalysis* **2014**, *57*, 1152–1162.

73. Chu, B.; Truter, L.; Nijhuis, T. A.; Cheng, Y., Performance of phase-pure M1 MoVNbTeOx catalysts by hydrothermal synthesis with different post-treatments for the oxidative dehydrogenation of ethane. *Applied Catalysis A: General* **2015**, *498*, 99–106.

74. Chen, X.; Yang, Q.; Chu, B.; An, H.; Cheng, Y., Valence variation of phase-pure M1 MoVNbTe oxide by plasma treatment for improved catalytic performance in oxidative dehydrogenation of ethane. *RSC Advances* **2015**, *5*, 91295–91301.

75. Che-Galicia, G.; Quintana-Solo´rzano, R.; Ruiz-Martı´nez, R. S.; Valente, J. S.; Castillo-Araiza, C. O., Kinetic modeling of the oxidative dehydrogenation of ethane to ethylene over a MoVTeNbO catalytic system. *Chemical Engineering Journal* **2014**, *252*, 75–88.

76. Che-Galicia, G.; Ruiz-Martı´nez, R. S.; Lo´pez-Isunza, F.; Castillo-Araiza, C. O.; Modeling of oxidative dehydrogenation of ethane to ethylene on a MoVTeNbO/TiO2 catalyst in an industrial-scale packed bed catalytic reactor. *Chemical Engineering Journal* **2015**, *280*, 682–694.

77. Elbadawi, A. H.; Ba-Shammakh, M. S.; Al-Ghamdi, S.; Razzak, S. A.; Hossain, M. M.; de Lasa, H. I., Phenomenologically based kinetics of ODH of ethane to

ethylene using lattice oxygen of VOx/Al2O3–ZrO2 catalyst. *Chemical Engineering Research and Design* **2017**, *117*, 733–745.

78. Al-Ghamdi, S.; Volpe, M.; Hossain, M. M.; De Lasa, H., VOx/c-Al2O3 catalyst for oxidative dehydrogenation of ethane to ethylene: Desorption kinetics and catalytic activity. *Applied Catalysis A: General* **2013**, *450*, 120–130.

79. Elbadawi, A. H.; Ba-Shammakh, M. S.; Al-Ghamdi, S.; Razzak, S. A.; Hossain, M. M., Reduction kinetics and catalytic activity of VOx/γ-Al2O3-ZrO2 for gas phase oxygen free ODH of ethane. *Chemical Engineering Journal* **2016**, *284*, 448–457.

80. Khan, M. Y.; Al-Ghamdi, S.; Razzak, S. A.; Hossain, M. M.; de Lasa, H., Fluidized bed oxidative dehydrogenation of ethane to ethylene over VOx/Ce-γAl2O3 catalysts: Reduction kinetics and catalyst activity. *Molar Catalysis* **2017**, *443*, 78–91.

81. Valente, J. S.; Quintana-Solo´rzano, R.; Armenda´riz- Herrera, H.; Barraga´n-Rodrı´guez, G.; Lo´pez-Nieto, J. M., Kinetic Study of Oxidative Dehydrogenation of Ethane over MoVTeNb Mixed-Oxide Catalyst. *Industrial Engineering Chemical Research* **2014**, *53*, 1775–1786.

82. Che-Galicia, G.; Lo´pez-Isunza, F.; Corona-Jime´nez, E.; Castillo-Araiza, C. O., The role of kinetics and heat transfer on the performance of an industrial wall-cooled packed-bed reactor: Oxidative dehydrogenation of ethane. *AIChE Jounral* **2020**, e16900.

83. Rahman, F.; Loughlin, K. F.; Al-Saleh, M. A.; Saeed, M. R.; Tukur, N. M.; Hossain, M. M.; Karim, K.; Mamedov, A., Kinetics and mechanism of partial oxidation of ethane to ethylene and acetic acid over MoV type catalysts. *Applied Catalysis A: General* **2010**, 375, 17–25.

84. Donaubauer, P. J.; Melzer, D. M.; Wanninger, K.; Mestl, G.; Sanchez-Sanchez, M.; Lercher, J. A.; Hinrichsen, O., Intrinsic kinetic model for oxidative dehydrogenation of ethane over MoVTeNb mixed metal oxides: A mechanistic approach. *Chemical Engineering Journal* **2020**, *383*, 123195.

85. Avdeev, V. I; Tapilin, V. M., Water Effect on the Electronic Structure of Active Sites of Supported Vanadium Oxide Catalyst VOx/TiO2(001). *Journal of Physical Chemistry C* **2010**, *114*, 3609–3613.

APPENDIX A

SUPPORTING INFORMATION FOR STABILIZATION OF CATALYTIC SURFACE THROUGH CORE-SHELL STRUCTURES: AG-IR/AL2O3 CASE STUD

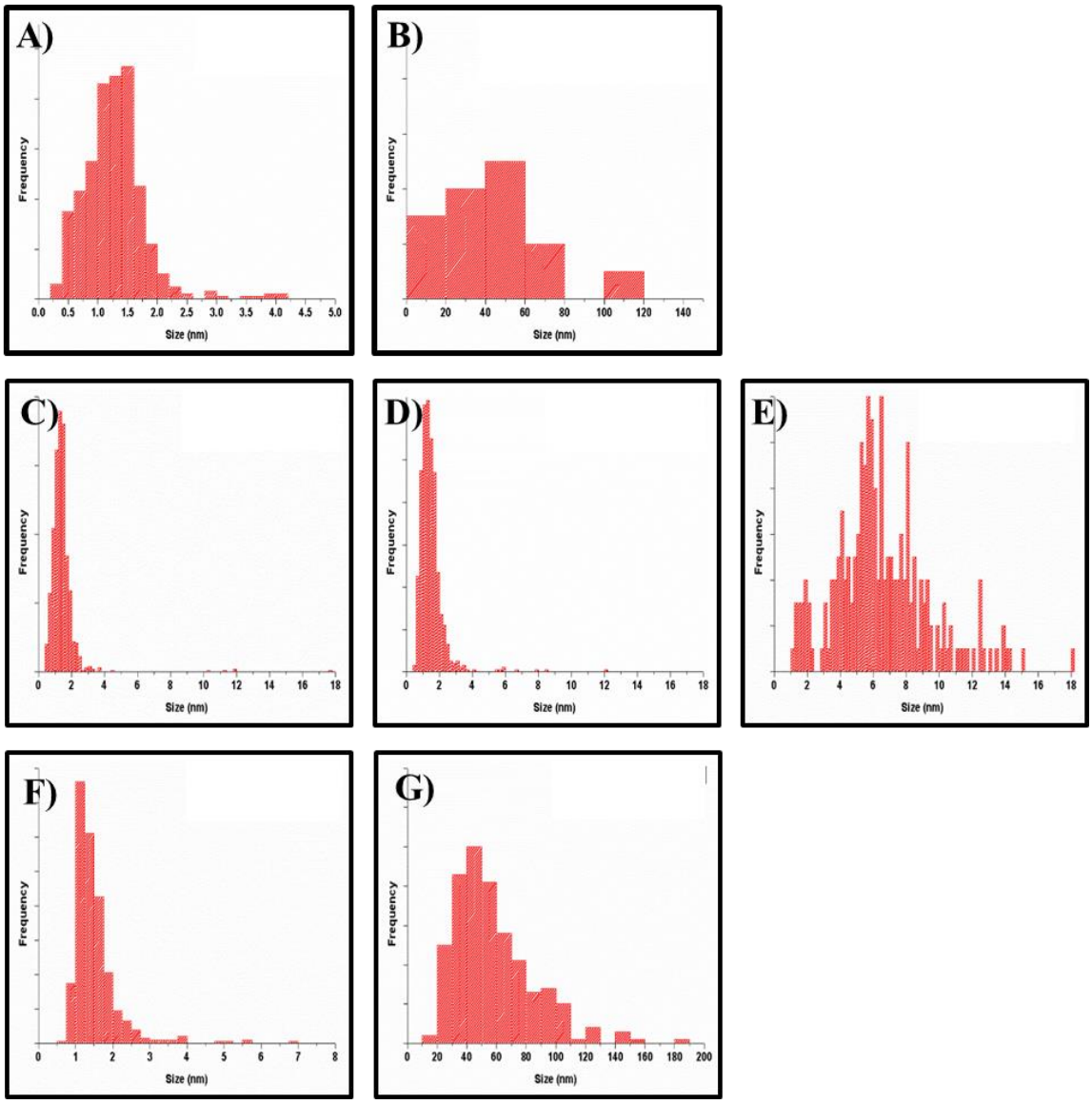

Figure A.1: Size distribution of (A) 1% Ir/δ,θ-Al_2O_3 fresh. (B) 1% Ir/δ,θ-Al_2O_3 at 800°C. (C-E) 0.35% Ag-Ir/δ,θ-Al_2O_3 at fresh, 400°C and 800°C, respectively. (F) 2.8% Ag-Ir/γ-Al_2O_3 at 800°C. (G) 3.2% Ir/γ-Al_2O_3 at 800° C.

APPENDIX B

COPYRIGHT PERMISSIONS